# STUDY OF HIGH ENERGY PHOTONS FROM HOT NUCLEAR SYSTEMS

*By*


**DEEPAK PANDIT**
**Experimental Nuclear Physics Division**
**VARIABLE ENERGY CYCLOTRON CENTRE**
**Kolkata-700064, India**


*A thesis submitted to the*
*Board of Studies in* **Physical Sciences**
*In partial fulfillment of requirements*
*For the Degree of*

**DOCTOR OF PHILOSOPHY**

*of*

**HOMI BHABHA NATIONAL INSTITUTE**
**Bhabha Atomic Research Centre**
**Mumbai-400085, India**

June, 2012

# Homi Bhabha National Institute

## Recommendations of the Viva Voce Board

As members of the Viva Voce Board, we certify that we have read the dissertation prepared by Deepak Pandit entitled 'Study of high energy photons from hot nuclear systems' and recommend that it may be accepted as fulfilling the dissertation requirement for the Degree of Doctor of Philosophy.

S. Bhattacharya — Date: 19/02/2013

Chairman: Dr. Sailajananda Bhattacharya

Date: 19/02/2013

Guide/Convener: Dr. S. R. Banerjee

Alok Chakrabarti — Date: 19/02/2013

Member: Dr. Dr Alok Chakrabarti

Satyajit Saha — Date: 19/02/2013.

Member: Prof. Satyajit Saha

Date: 19/02/2013

External Examiner: Dr. A. K. Sinha

Final approval and acceptance of this dissertation is contingent upon the candidates submission of the final copies of the dissertation to HBNI.

I hereby certify that I have read this dissertation prepared under my direction and recommend that it may be accepted as fulfilling the dissertation requirement.

**Date:** 19/02/2013

**Time:** 17:00 hrs.

**Guide:**

Dr. S. R. Banerjee

# STATEMENT BY AUTHOR

This dissertation has been submitted in partial fulfillment of requirements for an advanced degree at Homi Bhabha National Institute (HBNI) and is deposited in the Library to be made available to borrowers under rules of the HBNI.

Brief quotations from this dissertation are allowable without special permission, provided that accurate acknowledgement of source is made. Requests for permission for extended quotation from or reproduction of this manuscript in whole or in part may be granted by the Competent Authority of HBNI when in his or her judgment the proposed use of the material is in the interests of scholarship. In all other instances, however, permission must be obtained from the author.

Deepak Pandit 19/02/13

DEEPAK PANDIT

# DECLARATION

I, hereby declare that the investigation presented in the thesis has been carried out by me. The work is original and has not been submitted earlier as a whole or in part for a degree / diploma at this or any other Institution / University.

Deepak Pandit 19/02/13
DEEPAK PANDIT

## DEDICATIONS

**In the loving memories
of my best friend
SANGHITA DAS**

## ACKNOWLEDGEMENTS

First and foremost I would like to express my sincere thanks to Dr. S. R. Banerjee for his valuable guidance, supervision and constant encouragement throughout my thesis work. It has been an enjoyable experience working with you.

My sincere thanks also go to Dr. R. K. Bhandari (Director, VECC, Kolkata) and Dr. Dinesh Kumar Srivastava (Head, Physics group, VECC, Kolkata) for their valuable guidance.

I express my thanks to Dr. Sailajananda Bhattacharya, Dr. V. S. Pandit and Dr. Chandana Bhattacharya. I have had very valuable and fruitful physics discussions with them throughout these days.

I tender my heartful thanks to my collaborators cum friends Dr. Surajit Pal, Shri Supriya Mukhopadhyay, Dr Srijit Bhattacharya and Dr. Alokkumar De. I could not have completed my thesis without the support and encouragement from them. I have learnt academically and personally many things from Supriya Da and ever-enthusiastic Surajit Pal, 'Pal Babu'. I also thank my other collaborators Dr. G. Mukherjee, Dr. T. K. Ghosh, Shri K. Banerjee, Shri S. Kundu, Shri T. K. Rana, Shri R. Pandey, Mrs(Dr.) A. Dey, Shri A. Roy, Shri P. Dhara and Shri J. K. Meena for their help and full co-operation towards me.

I take this opportunity to thank the VECC cyclotron staff for the excellent operation of the machine during the experimental runs.

On a personal note, it would have been impossible for me to complete the thesis without the patience and moral support of my parents and my brother. Finally I would like to thank my wife Manjari for her continuous love, support and encouragement.

# Contents


**SYNOPSIS** . . . . . . . . . . . . . . . . . . . . . . . . . . . . . x

**List of Figures** . . . . . . . . . . . . . . . . . . . . . . . . . . xvii

**List of Tables** . . . . . . . . . . . . . . . . . . . . . . . . . . . xxii

**1 Introduction** **1**

1.1 High energy gamma rays . . . . . . . . . . . . . . . . . . . . . . 1

1.2 Giant resonances . . . . . . . . . . . . . . . . . . . . . . . . . . 3

1.3 Isovector giant dipole resonance . . . . . . . . . . . . . . . . . . 5

1.3.1 GDR centroid energy . . . . . . . . . . . . . . . . . . . 7

1.3.2 GDR width . . . . . . . . . . . . . . . . . . . . . . . . . 9

1.4 GDR built on excited state . . . . . . . . . . . . . . . . . . . . . 10

1.4.1 J-dependence of the GDR width . . . . . . . . . . . . . . 14

1.4.2 T-dependence of the GDR width . . . . . . . . . . . . . . 15

1.5 Effect of deformation on the GDR . . . . . . . . . . . . . . . . . 17

1.6 Motivation . . . . . . . . . . . . . . . . . . . . . . . . . . . . . 20

**2 High-energy $\gamma$-rays from spontaneous fission of $^{252}$Cf** **25**

2.1 Introduction . . . . . . . . . . . . . . . . . . . . . . . . . . . . 25

2.2 LAMBDA spectrometer . . . . . . . . . . . . . . . . . . . . . . . 26

2.3 Energy and time resolution . . . . . . . . . . . . . . . . . . . . . 28

2.4 Experiment and data analysis . . . . . . . . . . . . . . . . . . . 29

2.4.1 Front-end electronics and data acquisition . . . . . . . . 30

2.4.2 Rejection of neutrons, pile-up and cosmic events . . . . . 32

2.4.3 Event reconstruction . . . . . . . . . . . . . . . . . . . 35

2.5 Result and discussion . . . . . . . . . . 36

**3 Theoretical models** **42**

3.1 Introduction . . . . . . . . . . 42

3.2 The free energy . . . . . . . . . . 44

3.2.1 Deformed liquid drop energy . . . . . . . . . . 45

3.2.2 Moment of inertia . . . . . . . . . . 49

3.2.3 Entropy . . . . . . . . . . 50

3.3 Free energy surface & shape transition . . . . . . . . . . 50

3.3.1 Shape transition of $^{47}$V nucleus . . . . . . . . . . 51

3.3.2 Shape transition of $^{32}$S nucleus . . . . . . . . . . 53

3.4 Giant dipole resonance cross sections . . . . . . . . . . 54

3.5 Thermal shape fluctuation . . . . . . . . . . 56

3.6 Statistical model . . . . . . . . . . 58

3.6.1 CASCADE . . . . . . . . . . 59

**4 Giant dipole resonance $\gamma$-rays from hot $^{47}$V nucleus** **62**

4.1 Introduction . . . . . . . . . . 62

4.2 The multiplicity filter . . . . . . . . . . 63

4.2.1 Multiplicity detector fabrication . . . . . . . . . . 63

4.2.2 Energy and time resolution . . . . . . . . . . 64

4.2.3 Crosstalk probability . . . . . . . . . . 66

4.3 Experimental details . . . . . . . . . . 68

4.3.1 Trigger generation . . . . . . . . . . 69

4.3.2 Calibration of the detectors . . . . . . . . . . 72

4.4 Extraction of angular momentum . . . . . . . . . . 74

4.5 Experimental data analysis . . . . . . . . . . 76

4.6 Result . . . . . . . . . . 80

**5 Giant dipole resonance $\gamma$-rays from hot $^{32}$S nucleus** **83**

5.1 Introduction . . . . . . . . . . 83

5.2 Experimental details . . . . . . . . . . . . . . . . . . . . . . . . 85
5.3 Experimental data analysis . . . . . . . . . . . . . . . . . . . . . . 87
5.4 Result . . . . . . . . . . . . . . . . . . . . . . . . . . . . . . . . 94

**6 Summary and conclusion 97**

**Bibliography** . . . . . . . . . . . . . . . . . . . . . . . . . . . . 100

**List of Publications** . . . . . . . . . . . . . . . . . . . . . . . . 112

# SYNOPSIS

A natural approach to study the properties of the atomic nucleus is to heat it up and measure the frequencies of the emitted electromagnetic radiations. In other words, by measuring the $\gamma$-decay of the excited compound nuclei, one can probe the structure of nuclei at finite temperature ($T$) and angular momentum ($J$). Since the photon interacts with the nuclear medium through the relatively weak Coulomb interaction, it is one of the cleanest probes to study the diverse properties of the nuclei. The photons are emitted from excited compound nucleus through several mechanisms. Low energy discrete $\gamma$-rays are emitted during the de-excitation of equilibrated nuclei, which is a statistical process. The high-energy $\gamma$-rays (8-20 MeV) are produced from the decay of Giant Dipole Resonance (GDR) built on excited states in heavy ion fusion reaction while the most energetic photons ($>$ 20 MeV) originate from the bremsstrahlung phenomenon during the early stages of the reaction. The present thesis deals with the study of high-energy $\gamma$-rays from the decay of GDR built on the excited states for the investigation of the deformation in light $\alpha$ and non-$\alpha$ like systems and the emission of nucleus-nucleus coherent bremsstrahlung $\gamma$-rays from the spontaneous fission of $^{252}$Cf.

The GDR, a particularly interesting mode of collective vibration, can be understood as out of phase oscillations of the protons and the neutrons in the hot nucleus. Since, the decay of GDR occurs on a time scale that is sufficiently short ($\sim 10^{-22}$ s), it can provide information on the shape evolution of the nuclei at finite temperature and fast rotation which occurs in a much larger time scale. The resonance energy being inversely proportional to the nuclear radius, one gets a single lorentzian strength function for spherical nuclei since the vibrations along the three principal axes are same. However, the GDR strength function splits in the case of deformed nuclei and the investigation of this strength distribution gives a direct access to look into nuclear deformations. The decay of GDR $\gamma$-rays from hot $^{47}$V and $^{32}$S nuclei have been studied to explore the deformed shapes of light $\alpha$ and non-$\alpha$ systems using GDR lineshape and compare them with the corresponding predictions for equilibrium Jacobi shapes.

Rapidly rotating light nuclei in general are likely to undergo Jacobi shape transition, an abrupt change of shape from an oblate ellipsoid rotating around the symmetry axis to an elongated prolate or triaxial shape rotating perpendicularly around the symmetry axis, at an angular momentum value near the fission limit. Signatures of such shape transitions in $^{45}$Sc and $^{46}$Ti have been reported from the study of lineshapes of GDR built on excited states. Recently, in an experiment at VECC, the deformation of the excited $^{47}$V and $^{32}$S nucleus has been estimated from the inclusive $\alpha$-particle spectrum. The large deformations observed in light $\alpha$-like systems are believed to be due to the occurrence of either quasimolecular resonances or nuclear orbiting, which has the origin in the $\alpha$-cluster structure of these nuclei. The enhancement of fragment yield near the entrance channel as well as $\alpha$-spectroscopic studies for $^{32}$S have strongly indicated a highly deformed orbiting dinuclear shape from the previous studies. The $\alpha$-spectroscopic studies, however, can only indicate effective deformation in an indirect way. Hence, it is worthwhile to complement the above study by exploring the relationship between the shapes of the light $\alpha$-like systems and the corresponding Jacobi shapes directly via the GDR $\gamma$ decays in more direct manner.

The $\gamma$-ray yield from the decay of the GDR in self-conjugate nuclei ($^{32}$S) populated by T $=0$ entrance channel depends strongly on the isospin mixing due to the isovector nature of the electric dipole radiation. The E1 emission associated with the GDR ($\Delta$T=1) decay is hindered because the density of T=0 levels is always much higher than the density of T=1 levels. However, the yield of high energy $\gamma$-rays from N=Z compound nuclei increases in the presence of isospin mixing. In heavy ion collisions at projectile energies above 6 MeV/nucleon, incomplete fusion and pre-equilibrium nucleon emission processes also occur. Hence, the statistical emission of $\gamma$-rays may also arise following incomplete fusion or pre-equilibrium nucleon emission. Thus, a decaying compound nucleus may not be a N=Z nucleus. The mass and charge of the compound nucleus as well as the excitation energy are expected to be lower than in case of complete fusion.

The $^{47}$V and $^{32}$S nuclei were formed by bombarding pure 1 mg/cm$^2$ thick $^{27}$Al and $^{12}$C targets, respectively, with accelerated $^{20}$Ne beams from the K-130 cyclotron at the Variable Energy Cyclotron Centre, Kolkata, India. The $^{47}$V nucleus was populated at an excited energy of 108 MeV corresponding to a projectile energy of 160 MeV. Similarly, the initial excitation energies of $^{32}$S nucleus were 73 & 78 MeV corresponding to projectile energies of 145 & 160 MeV, respectively. The critical angular momenta for the two systems $^{47}$V and $^{32}$S were 38$\hbar$ and 24$\hbar$, respectively, and extend well beyond the critical angular momenta values of 29.6$\hbar$ and 21.5$\hbar$ at which the Jacobi transitions are predicted to occur for these nuclei (according to systematic $J_c = 1.2A^{5/6}$). The angular momentum values are also well below their fission limits for the two systems making it possible to probe these nuclei at these conditions. The high-energy photons were detected using the Large Area Modular $BaF_2$ Detector Array (LAMBDA) in coincidence with low energy $\gamma$-ray multiplicities measured with the multiplicity filter detector. The LAMBDA spectrometer arranged in a 7$\times$7 matrix was centered at 55° to the beam direction and at a distance of 50 cm from the target. Apart from the LAMBDA spectrometer, another $BaF_2$ based

50-element gamma multiplicity filter has been designed & developed in-house to measure the angular momentum in an event-by-event mode. The 50-element filter was split into two blocks of 25 detectors each and was placed on the top and the bottom of the scattering chamber at a distance of 10 cm from the target center (covering $\sim$30% of $4\pi$) in castle geometry to measure the $\gamma$-multiplicities in coincidence with the high-energy photon events.

The high-energy gamma spectra were extracted from the off-line analysis of the data recorded in the event-by-event mode by applying proper cuts on the Time-Of-Fight (TOF) and Pulse Shape Discrimination (PSD). After application of different conditions, in a valid event, the energy deposited in the detectors was summed using a nearest neighbor event reconstruction technique. Finally, the energies were Doppler corrected. The measured fold distributions from the multiplicity filter were mapped onto the angular momentum distributions using a realistic approach based on Monte Carlo GEANT simulation. Next, the experimental high-energy $\gamma$-ray spectra were analyzed using a modified version of the statistical model code CASCADE along with a bremsstrahlung component folded with the detector response function.

The linearized GDR lineshapes for the systems $^{47}$V and $^{32}$S are remarkably different from which one usually gets in the case of a spherical or a near spherical system and indicate large deformations. The most striking feature for $^{47}$V is the strong enhancement in the $\gamma$-ray yield at $\sim$10 MeV similar to the one observed in $^{46}$Ti earlier. It is the characteristics of Jacobi shape transition and Coriolis effect due to high angular momentum in the system undergoing giant dipole vibration. Since the statistical model code CASCADE used in the thesis does not include the effect of isospin, the data for $^{20}$Ne + $^{12}$C have been analyzed twice i.e. considering pre-equilibrium emission and without pre-equilibrium emission. For both the cases, the GDR parameters are very similar except for the overall GDR strength function indicating that, with the inclusion of isospin effect, the spectral shape of the GDR will not alter rather the magnitude of the overall strength function will be modified. Interestingly, no enhancement at $\sim$10 MeV is seen for the $^{32}$S nucleus although it is populated well above the Jacobi transition point. The shape looks more like a highly extended prolate (one component at $\sim$ 14 MeV and another at $\sim$ 26 MeV ) and is seen for the first time for this nucleus.

In order to understand the equilibrium deformation in these hot and rotating nuclear systems, a calculation is performed for estimating the equilibrium shape of a nucleus by minimizing the total free energy under the framework of rotating liquid drop model (RLDM) and thermal shape fluctuation model (TSFM) for a given temperature and angular momentum. It has been observed that our prediction of GDR strength function for an equilibrated shape from a minimized free energy (with thermal fluctuation included) describes the data for $^{47}$V remarkably well for both the experimentally measured spin windows. The enhancement of the strength at $\sim$10 MeV and the goodness of description are characteristic signatures of Jacobi transition in the case of $^{47}$V nucleus at these spin values. However, the same free energy calculation fails miserably to explain the GDR strength function for $^{32}$S performed at both low and high angular momentum. The shapes suggest a strongly prolate deformed nucleus ($\beta \sim 0.76$ for $E_{proj} = 160$ MeV, corresponding to an axis ratio of 1.94:1). The occurrence of such a large deformation without showing the characteristics of Jacobi transition is possible only if some other reaction mechanism is responsible. This unusual deformation, seen directly for the first time, has been speculated due to the formation of either the orbiting dinuclear configuration or molecular structure of $^{16}$O + $^{16}$O in $^{32}$S super deformed band.

Apart from the heavy ion fusion reaction, the high-energy coherent bremsstrahlung $\gamma$-rays ($>$ 20 MeV) are also believed to be produced from the spontaneous fission of $^{252}$Cf due to the acceleration of fission fragments in their Coulomb field. However, the high-energy $\gamma$-ray spectra, above 20 MeV, emitted in the spontaneous fission of $^{252}$Cf have been one of the fundamental problems of nuclear fission physics. From earlier studies, it has been seen that for energies above 20 MeV, the experimental data and theoretical calculations are contradictory. In few experiments, such high-energy $\gamma$-rays were not detected while in some experiment the high-energy $\gamma$-ray spectrum was measured. The yield of $\gamma$-rays with energies 20 - 120 MeV has been calculated using various models, but the calculations in different models differ by several orders of magnitude. Thus, the conflicting theoretical work as well as the experimental results motivates one to carry out further investigation of the high energy $\gamma$-rays ($>$ 20 MeV) emitted in the spontaneous fission of $^{252}$Cf.

An extensive experimental study was carried out using $^{252}$Cf source to investigate the photon emission accompanying the spontaneous fission at Variable Energy Cyclotron Centre (VECC), Kolkata. High energy $\gamma$-rays from the spontaneous fission of $^{252}$Cf were detected in coincidence with the low energy discrete $\gamma$-rays emitted from the decay of excited fission fragments in order to establish a correlation (photons/fission) between the high energy $\gamma$-rays and the fission process. The high-energy $\gamma$-rays were measured using the LAMBDA array and the prompt $\gamma$-rays with multiplicity detector. Four small $BaF_2$ detectors were placed as close as possible to the source to determine the start signal for each event. The LAMBDA array arranged in a 7$\times$7 matrix was kept at a distance of 35 cm from the source. Time of flight measurement distinguished the $\gamma$-rays from neutrons while long/short gate technique was applied to reject the pile up events. Data were collected in this $\gamma$-$\gamma$ coincidence mode for 450 hours. At the photon energies $E_\gamma$ $>$ 25 MeV, cosmic ray showers are major source of background, therefore, extreme precautions were taken to obtain the experimental data free from any cosmic impurity. Finally, the background events were subtracted by collecting the data for another 450 hours without the source.

Interestingly, high-energy $\gamma$-rays above 20 MeV were detected in the experiment pointing towards the evidence of nucleus-nucleus coherent bremsstrahlung. The photon spectrum was measured up to 80 MeV using the $^{252}$Cf source. The low energy (8 - 20 MeV) part of the photon spectrum is mainly associated with direct excitation of the giant dipole resonance (GDR) from the daughter nuclei arising in the fission process. However, the photons above 20 MeV can only be emitted by nuclear bremsstrahlung phenomenon since at start the nucleus has zero energy. It is also evident from the high-energy $\gamma$-ray spectrum since the slope changes sharply after 20 MeV clearly indicating that the mechanisms of the emission of photons below and above 20 MeV are completely different in origin.

A theoretical calculation was performed based on the classical Coulomb acceleration model to predict the yield of these photons above 20 MeV. The photon yield was estimated for a distribution of the most probable masses and charges arising from the fission of $^{252}$Cf including a pre-scission kinetic energy for the fragments. An attempt was also made to include the conservation of energy by multiplying the bremsstrahlung yield with a factor of $(1 - \hbar\omega/E)$, where $\hbar\omega$ is the energy carried away by the bremsstrahlung photons. This approximate calculation represents the experimental result quite well when the pre-scission kinetic energy is taken into account. However, a complete quantum mechanical calculation is desirable to predict the yield of bremsstrahlung $\gamma$-rays in nucleus-nucleus collision and is beyond the scope of this thesis.

# List of Figures


1.1 *The lowest multipoles of electric giant resonances.* . . . . . . . . . . . 4

1.2 *Photo-absorption cross-sections for the Sn isotopes (symbols). The full line is a fit with Lorentzian curve.* . . . . . . . . . . . . . . . . . 6

1.3 *Schematic drawings of the Goldhaber-Teller and Steinwedel-Jensen dipole modes. For each case, one-half cycle of the vibration is shown as a function of time.* . . . . . . . . . . . . . . . . . . . . . . . . 7

1.4 *Schematic diagram showing the decay of the compound nuclei.* . . . . 11

1.5 *High-energy gamma ray spectrum showing different regions.* . . . . . . 12

1.6 *The calculated $\gamma$-spectrum obtained as a best fit to the data for $^{110}$Sn at $E_x$=92 MeV, which corresponds to an effective temperature of $\sim$ 2 MeV. The first-step contribution is indicated by T=2 (dashed curve) while later contributions at the lower temperatures T=1 and T=0.5 are indicated by the dot-dashed and thin curves, respectively. As expected the highest-energy $\gamma$-rays are predominantly due to first-step emission while the lower-energy ones originate mainly from later steps.* . . . . . . . . . . . . . . . . . . . . . . . . . . . . . . . . . 13

1.7 *(a) Evolution of the equilibrium deformation for $^{106}$Sn as a function of the angular momentum (continuous line). The dashed line shows the value of the variance of the deformation ($\Delta\beta$). (b) The reduced GDR widths are plotted against the reduced parameter J/A$^{5/6}$ for different nuclei. The symbols represent the experimental data while the continuous line refers to the theoretical prediction. (c) The GDR widths as a function of T for $^{63}$Cu, $^{120}$Sn and $^{208}$Pb. The different symbols represent the experimental data. The dashed, continuous and dot-dashed lines correspond to the prediction of TSFM, CTFM and PDM, respectively. The dotted line in $^{208}$Pb panel is the shell effect included TSFM calculation [Orm96].* . . . . . . . . . . . . . . . . . . 15

1.8 *The Jacobi shape transition is shown schematically. Due to high rotation the spherical shape changes to an oblate shape rotating parallel to the symmetric axis and finally to a collective prolate shape rotating perpendicular to the symmetry axis. The corresponding GDR lineshape (idealized) is shown below for all the shapes (continuous line).* 19

2.1 *The LAMBDA spectrometer arranged in three 7×7 matrix.* . . . . . . 27

2.2 *(a) The schematic view (top) of the experimental setup and (b) Front view of the LAMBDA spectrometer.* . . . . . . . . . . . . . . . . . . 29

2.3 *(a) The long gate and short gate for pulse shape discrimination (PSD) along with an unattenuated $BaF_2$ signal.* . . . . . . . . . . . . . . . . 31

2.4 *The time of flight (TOF) spectrum during online experiment.* . . . . . 32

2.5 *The pulse shape discrimination (PSD) spectrum during online experiment. The selection of $\gamma$-band is shown with continuous line.* . . . . . 33

2.6 *The typical cosmic muon tracks in LAMBDA spectrometer arranged in 7×7 matrix. The direction of the muon tracks are shown by the arrows along with the actual energy deposits in the detector elements.* 34

2.7 *The cluster summing technique of the LAMBDA spectrometer arranged in a 7×7 matrix. The cluster is shown as a shaded rectangle while the central detector of cluster is marked with box.* . . . . . . . . 35

2.8 *The experimentally measured $\gamma$-spectrum (filled circles). The dotted line represents the CASCADE calculation. The dashed line represents the pure Coulomb calculation. The solid lines correspond to the calculation including conservation of energy while the dot-dashed line represents the calculation including both conservation of energy and pre-scission kinetic energy. [Inset] The experimental data compared with a previous result [Ple95] (open circle).* . . . . . . . . . . . . . . 37

2.9 *The experimentally measured $\gamma$-spectrum compared with the data observed in other experiments.* . . . . . . . . . . . . . . . . . . . . . . 40

3.1 *Nuclear shapes in the $(\beta, \gamma)$ plane. The figure shows the orientation of the shape relative to the rotation axis (the z-axis in this case).* . . . 43

3.2 *Liquid drop free energy surfaces at different spins of $^{47}V$. The line represents the prolate shape ($\gamma = 0°$) while the dotted line corresponds to minimum of the free energy at $J = 0\hbar$.* . . . . . . . . . . . . . . . 51

3.3 *The equilibrium shapes are plotted as a function of quadrupole deformation parameters $\beta$ and $\gamma$ for different spins for $^{47}V$ nucleus. The discrete spin values are represented alongside the data points.* . . . . . 51

3.4 *The moment of inertia plotted as a function of angular momentum for the total shape change for $^{47}V$ nucleus.* . . . . . . . . . . . . . . . 52

3.5 *The equilibrium shapes are plotted as a function of quadrupole deformation parameters $\beta$ and $\gamma$ for different spins for $^{32}S$ nucleus. The discrete spin values are represented alongside the data points.* . . . . . 53

3.6 *The moment of inertia plotted as a function of angular momentum for the total shape evolution for $^{32}S$ nucleus.* . . . . . . . . . . . . . . 53

3.7 *The deformation probability distributions in the $(\beta, \gamma)$ plane for the $^{47}V$ nucleus at different temperature (clockwise from the top left side). The distribution is normalized in such a way that the peak probability in each case is 1.* . . . . . . 57

4.1 *The step by step process for detector fabrication from a bare crystal. Clockwise from the top left side. I. Cleaning of the bare $BaF_2$ crystal with pure dehydrated ethyl alcohol. II. The wrapping of the crystal with white teflon tape. III. The wrapped aluminium foil over the teflon wrapped crystal. IV. The black electric tape wrapped over the aluminium tape for light tightness.* . . . . . . 65

4.2 *The step by step process for detector fabrication from a bare crystal. Clockwise from the top left side. I. Highly viscous optical grease over the crystal surface before connecting to PMT. II. Coupling of the PMT with the crystal. III. The specially designed aluminium collar being put around the coupling area to provide additional support. IV. The total assembly covered with black electric tape and finally with heat shrinkable tube to provide mechanical stability to the detector.* 65

4.3 *The full multiplicity filter arranged in two blocks of 5×5 arrays.* . . . . 66

4.4 *Energy spectra from a single multiplicity detector for different laboratory standard gamma ray sources.* . . . . . . 67

4.5 *Time resolution of an individual detector using $^{60}Co$ $\gamma$-source.* . . . 67

4.6 *The crosstalk probabilities for three energies ($^{22}Na$, $^{137}Cs$ and $^{60}Co$) at different thresholds of the multiplicity filter. The symbols represent the experimental points while the lines correspond to GEANT simulation.* . . . . . . 68

4.7 *The experimental setup of the LAMBDA spectrometer along with the multiplicity filter.* . . . . . . 70

4.8 *The electronic scheme of the experimental setup.* . . . . . . 71

4.9 *Top panel: The Am-Be spectrum in one of the large $BaF_2$ detectors during calibration. The left panel shows the comparison between raw spectrum (red circles) and no-leak spectrum (blue circles) while the no-leak spectrum is shown independently in the right panel. Bottom panel: Cosmic muon spectrum in the same detector during calibration. In the left panel, the raw spectrum (red line) is shown along with the vertically fired condition (blue line). The spectrum for vertically fired condition is shown in the right panel. The spectrum is fitted with Landau function to extract the most probable energy (continuous line).* 72

4.10 *The $^{22}Na$ spectrum during calibration is shown in the top panel while the calibration curve is shown in the bottom panel.* . . . . . . 73

4.11 *The experimental fold spectrum (symbols) fitted with GEANT simulation (solid line).* . . . . . . . . . . . . . . . . . . . . . . . . . 75

4.12 *The incident multiplicity distribution used in GEANT simulation (symbols along with dotted line). The multiplicity distributions obtained for different folds are also shown in the figure. The solid line represents fold 2 while the dashed line represents fold ≥3.* . . . . . . 75

4.13 *The experimental high-energy $\gamma$-ray spectra.* . . . . . . . . . . . . . 77

4.14 *The high-energy $\gamma$-ray spectra (filled circles) along with CASCADE prediction (continuous line) consisting of five GDR component for $^{47}V$ nucleus.* . . . . . . . . . . . . . . . . . . . . . . . . . . . 79

4.15 *The linearized experimental GDR strength function (filled circles) together with best fitting 5-Lorentzian function (continuous line) and its individual components.* . . . . . . . . . . . . . . . . . . . . . . 80

4.16 *The predicted line shapes from the free energy minimization technique (continuous lines) are compared with the linearized GDR strength functions for $^{47}V$ for the two angular momentum windows. The filled circles are the experimental data.* . . . . . . . . . . . . . . . . . . 81

5.1 *The experimental setup of the LAMBDA spectrometer arranged in 7×7 matrix along with the multiplicity filter placed on top and bottom of the scattering chamber.* . . . . . . . . . . . . . . . . . . . . . . 86

5.2 *The experimental high-energy $\gamma$-ray spectra (filled circles) for two incident beam energies for $^{32}S$ nucleus. The dashed line corresponds to CASCADE calculation (without GDR strength function) while the dot-dashed line represents the bremsstrahlung component. The sum of the two (continuous line) is compared with the experimental data. The bottom panel shows the divided plot.* . . . . . . . . . . . . . . 88

5.3 *The high-energy $\gamma$-ray spectra (filled circles) along with CASCADE prediction including GDR strength function (dashed line) for two incident beam energies for $^{32}S$ nucleus. The dot-dashed line represents the bremsstrahlung component while the continuous line corresponds to CASCADE + bremsstrahlung.* . . . . . . . . . . . . . . . . . . 89

5.4 *The GDR lineshape for the two-incident energy. The symbols represent the experimental data; continuous lines correspond to the GDR strength functions used in CASCADE while the dashed lines represent the TSFM calculation for $^{32}S$ nucleus at $J$=22$\hbar$ and $T$ = 2.8 MeV.* . 89

5.5 *Same as Fig.5.2 but with pre-equilibrium correction.* . . . . . . . . . 90

5.6 *Same as Fig.5.3 but with pre-equilibrium correction.* . . . . . . . . . 91

5.7 *The GDR lineshape for the two-incident energy (with pre-equilibrium correction). The symbols represent the experimental data; continuous lines correspond to the GDR strength functions used in CASCADE while the dashed lines represent the TSFM calculation for $^{31}P$ nucleus at $J = 16\hbar$ and $T = 1.9$ MeV.* . . . . . . . . . . . . . . . . . . . . . . 93

5.8 *The evolution of GDR lineshape with angular momentum for $^{32}S$ nucleus at $T = 2.8$ MeV.* . . . . . . . . . . . . . . . . . . . . . . . . . . 93

# List of Tables

4.1 Average angular momentum values corresponding to different folds. 76

4.2 The extracted GDR components for two angular momentum windows for $^{47}$V. . . . . . . . . . . . . . . . . . . . . . . . . . . . 79

5.1 The extracted GDR components for two incident energies for $^{32}$S. 94

5.2 The extracted GDR components including pre-equilibrium correction. . . . . . . . . . . . . . . . . . . . . . . . . . . . . . . . 94

# Chapter 1

# Introduction

## 1.1 High energy gamma rays

Electromagnetic radiation produced in nuclear reactions has been an important subject of study since the beginning of nuclear science. The reason for the continuing interest in photons from nuclear reaction is the fact that it allows one to probe the nucleon-nucleon interaction, the structure of nuclei and the dynamics of nuclear reactions. Since the photon interacts with the nuclear medium through the relatively weak Coulomb interaction, it often provides one of the cleanest probes available for the study of nuclear systems.

The photons from the excited compound nucleus are emitted through several mechanisms. Low-energy photons are mostly produced during the de-excitation of equilibrated nuclei, which is a statistical process. The high energy gamma rays (8 - 20 MeV) are emitted from the decay of giant dipole resonance (GDR) built on excited states in heavy ion fusion reactions (discussed in section 1.4). These high-energy photons are mainly used to study various aspects of the structure of excited nuclei. The most energetic photons ($>$ 20 MeV), however, are produced during the first stages of the nuclear reaction in which the nucleus is not equilibrated. These high-energy photons originate mainly from bremsstrahlung, which is by definition a dynamical process and can therefore be used as a probe for reaction studies.

The present thesis deals with the study of high-energy gamma rays from the decay of GDR built on the excited states for the investigation of the deformation in light $\alpha$ and non-$\alpha$ like systems and the emission of nucleus-nucleus coherent bremsstrahlung originating from $^{252}$Cf spontaneous fission.

Fission is a nuclear reaction in which a massive nucleus splits into two fragments of nearly equal mass (binary fission) with the simultaneous release of energy ($\sim$200 MeV). Around 80% of the total energy released in fission process is converted into the kinetic energy of the fission fragments in a time of $10^{-21} \sim 10^{-19}$ seconds. Since very small time scales are involved, the fission fragments are imparted with a huge impulsive force originating from the Coulomb repulsion of the fragments leading to massive accelerations. This sudden increase of velocity leads to the production of coherent nucleus-nucleus bremsstrahlung. The $^{252}$Cf undergoes $\alpha$-decay 96.9% of the time while the remaining 3.1% of decays are spontaneous fission with a half-life of 2.645 years. Thus, it provides us with an unique source to study the bremsstrahlung phenomenon in nuclear fission since the photons above 20 MeV can only be emitted by nuclear bremsstrahlung phenomenon as the nucleus has zero energy before fission.

The GDR can be understood as out-of-phase vibration of neutrons against protons with a dipole spatial pattern. This vibration couples directly to the nuclear shape degrees of freedom and the investigation of its strength distribution gives a direct access to the nuclear deformations. Moreover, it also occurs on a time scale that is sufficiently small and thus competes with the other modes of nuclear decay. Therefore, measurement of energetic photon from the excited nuclei allows one to study the nuclear properties at finite temperature and spin.

## 1.2 Giant resonances

The study of giant resonances, an important collective phenomena, provide a great field of research which concerns the structure of quantal many body systems. They have greatly contributed to our understanding of bulk behaviour of such systems and their non-equilibrium properties. For a variety of many body systems, it is possible to describe the excitation spectra in terms of elementary modes of excitation representing different fluctuations about the equilibrium. These correspond partly to shape oscillations of different multipole order and partly to fluctuations in which the neutrons move collectively with respect to the protons. In other words, they can be viewed as a high frequency, damped, (nearly) harmonic density/shape vibration around the equilibrium density/shape of the nuclear system. The vibration amplitude is small, only a few percent of the nuclear radius, resulting in a frequency of $\sim 3$ x $10^{21}$ Hz [Bor01] and lie in the typical excitation energy range of 5 to 30 MeV, depending on the nuclear mass and the type of resonance. The giant resonances are classified according to their multipolarity $L$, spin $S$ and isospin $T$ quantum numbers [Har01].

The electromagnetic multipole moments for the excitation of electric giant resonances can in the long wavelength approximation ($kr \ll 1$) be written as [Har01, Sri09],

$$Q_E(LM) = \int r^L Y_{LM} \rho(\vec{r})\, d\tau \tag{1.1}$$

where $k$ is the wave vector and $\mathrm{r}^L\mathrm{Y}_{LM}$ is the operator. $Y_{LM}$ are the associated spherical harmonics of the multipole $L$, $r$ is the radius of the nucleus and $\rho(\vec{r})$ is the charge density. $E$ in the subscript of $Q$ implies electric mode i.e. vibration induced by electric field only. In this case, no spin is involved ($\Delta S = 0$). It is possible to have multipole excitation with the involvement of spin excitation.

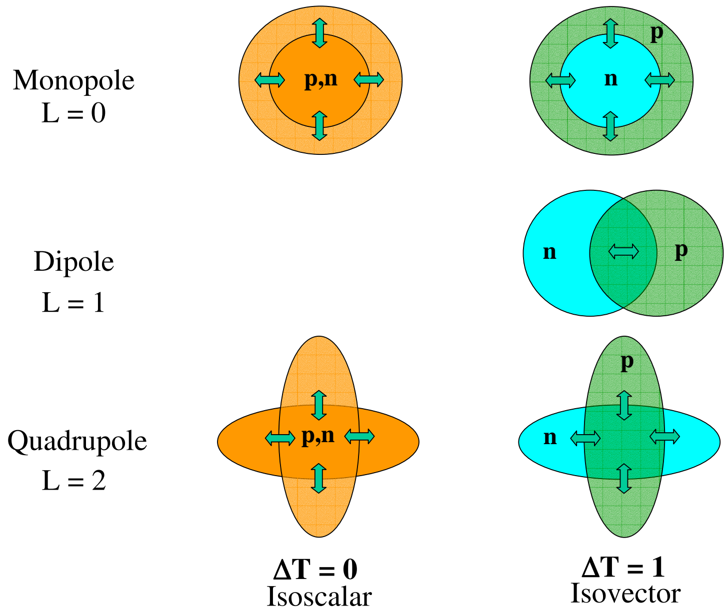


Figure 1.1: *The lowest multipoles of electric giant resonances.*

These are called the magnetic multipoles where the spin orientation of the nucleons are involved ($\Delta S = 1$). The electric and magnetic giant resonances can be further classified as isoscalar mode (IS) ($\Delta T = 0$) in which the nucleons oscillate in phase inside the nucleus and isovector (IV) ($\Delta T = 1$) modes where the protons and the neutrons move out of phase inside the nucleus. The $L = 0$ mode is called the giant monopole resonance (GMR). For this mode, the first-order operator in eq.(1.1) becomes a constant and it is the second-order operator r$^2$ Y$_{00}$ which is responsible for its excitation. The corresponding collective picture is the radial vibration of the nucleus. $L = 0$, $\Delta T = 0$ mode, the breathing mode, is the isoscalar GMR. Its excitation energy is directly related to the incompressibility of the nucleus, which is a fundamental quantity of nuclear matter and an important input parameter in nuclear equation of state. From the selection rule principle, for $L = 0$ mode $\gamma$ emission is not possible. $L = 1$ multipoles represent the collective dipole vibration. The isoscalar dipole operator corresponds in first order to the centre of mass coordinate which induces a translational motion of the nucleus and thus does not lead to an intrinsic nuclear excitation. However, the second-order isoscalar dipole operator can lead to intrinsic nuclear excitation. It is viewed as the squeezing compressional mode. In the IVGDR, the protons and neutrons oscillate against each other creating a changing dipole moment. $L = 2$ and higher multipoles represent the shape vibration of the nucleus. $L = 2$ represents the quadrupole vibration which means a changing electric quadrupole moment of the nucleus. A pictorial representation of the collective macroscopic picture of the various electric GRs is shown in Fig.1.1. The resonance energy for the GR can be well described by an $A^{-1/3}$ dependence, where $A$ is the nuclear mass number, the constant of proportionality being equal to about 79 MeV for GDR, 80 MeV for GMR, 65 MeV for ISGQR and 140 MeV for IVGQR, respectively [Sri09].

## 1.3 Isovector giant dipole resonance

The first evidence of the giant resonance type phenomenon was observed by Bothe and Gentner [Bot37] in 1937 during their measurement of induced radioactivity by bombarding various samples with $\gamma$-radiations from Li(p, $\gamma$) reactions. The isovector giant dipole resonance (IVGDR) is the best known GR due to the high selectivity for GDR excitation by $\gamma$-absorption. Over the years, a considerable amount of photon-absorption cross-sections have been acquired for a variety of masses using the bremsstrahlung photons produced from the electron accelerators and with mono-energetic photons obtained from the positron-annihilation in-flight technique [Bal47, Ber69, Ber75, Die88]. The GDR has been observed in nuclei as light as $^{4}$He to the heaviest one. The $\gamma$-absorption cross-section for most non-deformed, medium-heavy and heavy, nuclei in the energy range from about 10-20 MeV can be very well described by a Lorentzian

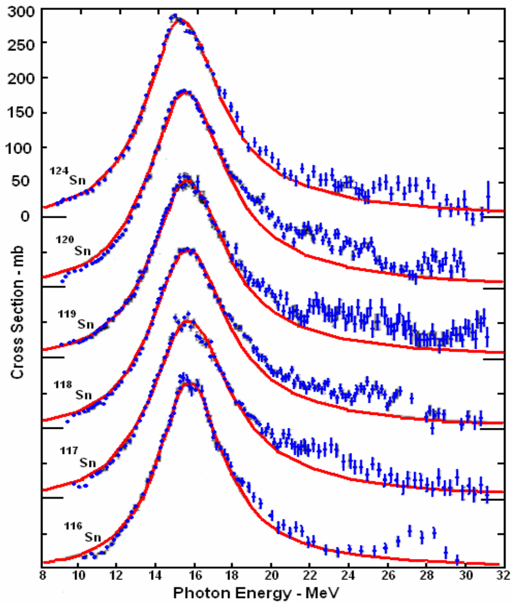


Figure 1.2: *Photo-absorption cross-sections for the Sn isotopes (symbols). The full line is a fit with Lorentzian curve.*

curve

$$\sigma_{abs}(E_\gamma) = \frac{\sigma_m \Gamma^2_{GDR} E^2_\gamma}{(E^2_\gamma - E^2_{GDR})^2 + \Gamma^2_{GDR} E^2_\gamma} \tag{1.2}$$

where $\sigma_m$ is the peak cross-section with $E_{GDR}$ & $\Gamma_{GDR}$ defining the energy and the width of the resonance, respectively.

An example of such a fit for the Sn isotopes is depicted in Fig.1.2. The spectra clearly show all the beautiful features of resonance absorption. The figure has been adopted from [Ber75]. However, for light nuclei, the GDR does not show up as a very nice well-located resonance and the excitation mode seems to spread out over a range of excitation. The resonance exhausts a large part of the energy weighted sum rule (EWSR) for dipole radiation. The sum rule strength of GDR integrated up to $E_\gamma$= 30 MeV is given approximately by Thomas-Reiche-Kuhn (TRK) dipole sum rule and can be calculated from the

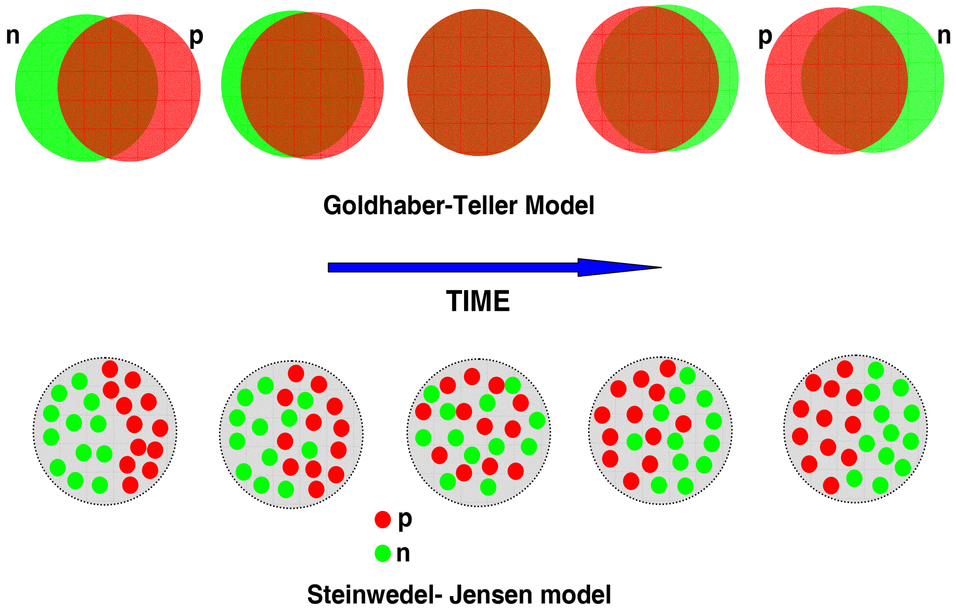


Figure 1.3: *Schematic drawings of the Goldhaber-Teller and Steinwedel-Jensen dipole modes. For each case, one-half cycle of the vibration is shown as a function of time.*

classical electrodynamics [Jac75]:

$$\int_0^{30MeV} \sigma_{abs}(E_\gamma)dE_\gamma = \left(\frac{2\pi^2\hbar r^2}{Mc}\right)\left(\frac{NZ}{A}\right) = 60\frac{NZ}{A}MeV.mb \tag{1.3}$$

In heavy nuclei, the experimental GDR cross section exceed the TRK sum rule by $\sim$ 30%, while in the light nuclei the strength falls a little short of it. Thus, the result well indicates that all the nucleons within the nucleus participate in giant resonance vibrations.

### 1.3.1 GDR centroid energy

Macroscopically, the isovector giant dipole vibration is interpreted as the superposition of the Goldhaber-Teller (GT) [Gol48] and the Steinwedel-Jensen (SJ) modes [Ste50]. The GT mode, dominant for nuclei with low mass, also amounts more than the SJ mode for all nuclei. However, the contribution of SJ mode increases with A and becomes almost equal for heaviest nucleus [Mye77].

The Steinwedel-Jensen (SJ) model [Ste50] assumes that the protons and the neutrons on the surface of the nuclei have fixed positions with respect to each other. Motion of protons and neutrons inside the nucleus causes density changes in the proton-fluid and neutron fluid. This kind of motion corresponds to the lowest acoustic mode in a spherical cavity. Thus, the frequency of oscillation would be inversely proportional to the radius of the nucleus and inversely proportional to $A^{1/3}$.

On the other hand, the Goldhaber-Teller (GT) Model [Gol48, Mye77] assumes that the protons and the neutrons behave as two inter-penetrating incompressible fluids. During the dipole vibration, the two fluids suffer a relative displacement so that near the nuclear surface the two fluids no longer overlap. The total restoring force will be proportional to the surface, that is, to $R^2$. For small displacement, the frequency ($\omega$) of the resulting harmonic motion is proportional to the square root of force over mass. Thus, we have $\omega \sim (R^2/R^3)^{1/2} \sim R^{-1/2}$ and the frequency of oscillation varies as $A^{-1/6}$. The above two models have been pictorially represented in Fig.1.3. The excitation energy of the IVGDR can be reproduced quite well by the expression [Har01]

$$E_{GDR} = 31.2A^{-1/3} + 20.6A^{-1/6} \tag{1.4}$$

Microscopically, the GDR is described as a coherent superposition of one particle-one hole (1p-1h) configurations, often called the collective particle-hole doorway resonance. The term doorway implies that the excited nucleus passes from the entrance channel through the doorway state before the full complexity of the compound nuclear states are populated. In order to describe the resonance in this way the p-h interaction has to be taken into account. Strong E1 matrix elements occur for single-particle excitations from one major shell to the next adjacent shell; hence in the independent-particle shell model the energy of this state is $1\hbar\omega = 41 \cdot A^{-1/3}$ MeV. Inclusion of the repulsive interaction between particles and holes shifts the energy of the GDR up to its observed value of $\sim 2\hbar\omega$ in heavy nuclei, and somewhat less in light nuclei. The microscopic picture has severe limitations. As the energy increases, it becomes more and more difficult to perform such microscopic calculations [Vre99].

### 1.3.2 GDR width

All giant resonances have a width i.e. the oscillatory motion is damped. In heavy nuclei, the damping is mostly due to dissipative processes in which the collective energy is converted into internal energy. The damping mechanism of the dipole collective vibration is of particular interest since it gives an idea about the nuclear shear viscosity. The typical value of the width for heavy nuclei is about 5 MeV implying that after a few vibrations the resonance is completely damped owing to energy dissipation [Har01]. The general trend of the width ($\Gamma_{GDR}$) as deduced from the Lorentzian fit shows that it is smallest for closed shell nuclei, about 4 MeV for nuclei around $^{90}$Zr and $^{208}$Pb, and increases to 5-6 MeV for nuclei between shells. However, it needs to be mentioned that for deformed nuclei the width was obtained by fitting one single Lorentzian. Hence, the deformation induced widening of the width was considered as a part of damping. In general, the width for viscous systems should increase as A decreases since the damping increases with decreasing volume.

Microscopically, the total width of the GDR built on ground state ($T = 0$ MeV) consists of the landau width, the spreading width and the escape width [Har01]. The landau width arises from the coupling of the correlated 1p-1h excitation with the uncorrelated 1p-1h configuration in the same excitation energy range causing a fragmentation of the initial collective 1p-1h strength function. The spreading width is associated with the mixing of the correlated 1p-1h state with more complex and numerous 2p-2h configurations, whereas, the escape width arises because of coupling to the continuum causing the direct particle decay into hole states of the residual nucleus. In medium and heavy nuclei, it turns out that the landau and escape widths only account for a small fraction and the major contribution of the large resonance width comes from the spreading width [Bor98]. Recently, an empirical formula has been derived for the spreading width [Jur08] with only one free fit parameter by separating the deformation induced widening from the spreading effect, and is expressed as $\Gamma_{sp} = 0.05 \cdot E_{GDR}^{1.6}$. The relation has been found to hold good for the widths of the different GDR components corresponding to the three axes of a deformed nucleus in general [Jur08, Erh10]. The inclusion of the deformation in describing the apparent GDR width is also supported by the recent experimental [Sre06] and theoretical [Del10] development in the description of nuclear ground state deformation.

## 1.4 GDR built on excited state

The excited state GDR, as the name suggests, implies that the GDR is actually built on the excited states of the nucleus. The first evidence for the excited state GDR was found in 1974, during the study of high energy $\gamma$-rays from the fission fragments in spontaneous fission of $^{252}$Cf [Die74]. The possibility of such an excited state GDR is in agreement with the Brink-Axel hypothesis [Bri62] which states that a GDR can be built on any nuclear state. Later, in 1981 it was experimentally established that the same phenomenon of increased $\gamma$-decay in the IVGDR energy range also occurs in the decay of hot nuclei produced in fusion reactions [New81]. In heavy-ion fusion reaction, both energy and angular momentum are transferred to the compound system. In general, neither the initial energy nor the initial angular momentum of the compound nucleus is sharply defined. The uncertainty in excitation energy is due to pre-equilibrium

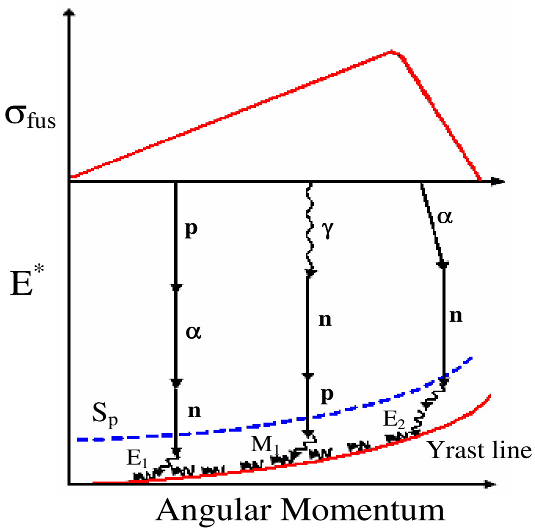


Figure 1.4: *Schematic diagram showing the decay of the compound nuclei.*

emission and incomplete-fusion process [Bor91, Kel97, Kel99]. The spread in angular momentum originates from the spread in the impact parameter of the collision.

Once the hot equilibrated nuclear system is formed, it decays sequentially by emission of neutrons, charged particles and with a much lower probability by emission of $\gamma$-rays. Neutron emission is possible as long as the excitation energy $E_x > E_{yrast} + B_n$ , where $E_{yarst}$ is the J-dependent energy of the yrast line and $B_n \sim 8$ MeV the neutron binding energy. The GDR $\gamma$-decay can occur after $xn$-emission, where $x$ = 0,1,2,.., as long as $E_x > E_{yrast} + E_{GDR}$, where $E_{GDR} \sim 10$ MeV or higher is the energy of the emitted IVGDR decay photon. Thus, the measured IVGDR $\gamma$-ray spectrum originates not only from the initial nucleus but also from all the nuclei populated in the de-excitation chain. However, $\gamma$-ray with an energy $E_\gamma > B_n + 2T$, with $T$ the temperature of the emitting system, will be preferentially emitted in the first few steps of the de-excitation chain [Har01]. If the cooling process has advanced to the energy region $E_{yrast} < E_x < E_{yrast} + B_n$, further cooling to the yrast level

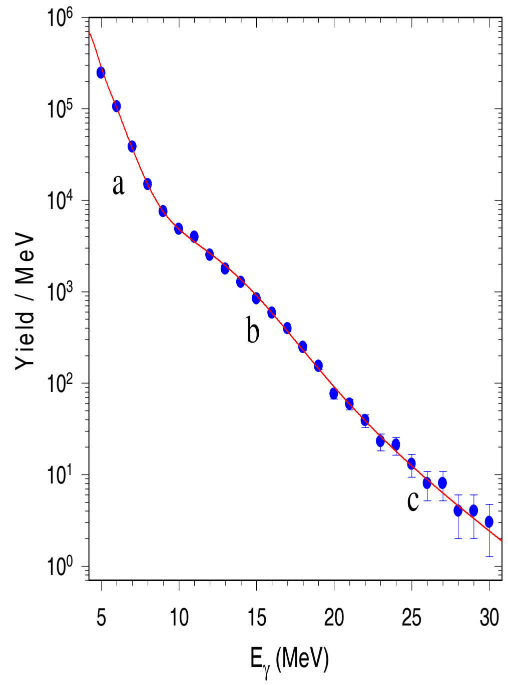


Figure 1.5: *High-energy gamma ray spectrum showing different regions.*

will occur through emission of lower energy, mainly statistical E1 $\gamma$-emission. Subsequently, decay along the yarst line occurs by low-energy discrete E2 $\gamma$-radiation, the multiplicity of which is related to the initial angular momentum. The decay of the compound nuclei is schematically indicated in Fig.1.4.

For an understanding of the experimental high-energy $\gamma$-spectrum from excited compound nuclei, it may be divided into different regions in terms of $\gamma$-ray energies. A typical high energy $\gamma$-spectrum is shown in Fig.1.5. (a) The spectrum is dominated by statistical $\gamma$-decay for $E_\gamma \leq 8$ MeV, which originates from the last steps in the decay chain when the nucleus is already cooled down to an energy $E_{yrast} < E_x < E_{yrast} + B_n$. (b) In the energy region $10 \leq E_\gamma \leq 25$ MeV, the spectrum is mainly due to statistical decay of GDR. (c) The slope of the spectrum changes after $E_\gamma \geq 25$ MeV and is dominated mainly by the nucleon-nucleon bremsstrahlung emitted during the initial stage of the equi-

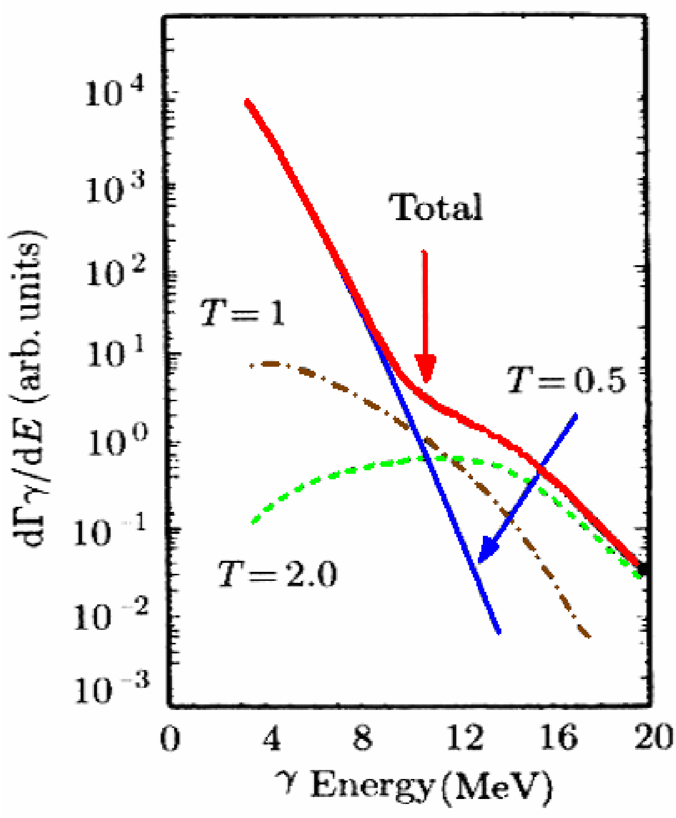


Figure 1.6: *The calculated $\gamma$-spectrum obtained as a best fit to the data for $^{110}$Sn at $E_x$=92 MeV, which corresponds to an effective temperature of $\sim$ 2 MeV. The first-step contribution is indicated by T=2 (dashed curve) while later contributions at the lower temperatures T=1 and T=0.5 are indicated by the dot-dashed and thin curves, respectively. As expected the highest-energy $\gamma$-rays are predominantly due to first-step emission while the lower-energy ones originate mainly from later steps.*

libration process of the fusion reaction. Fig.1.6 shows for the nucleus $^{110}$Sn at $E_x$ = 92 MeV how the spectra at various T-values contribute to the total $\gamma$-spectrum. The figure has been adopted from [Har01]. The highest energy $\gamma$-rays are predominantly due to first-step emission while the lower energy ones originate mainly from later steps [Bor98].

In the last few years, many experiments have been performed using heavy ion fusion and inelastic scattering of light projectiles on heavy targets to study the temperature (T) and angular momentum (J) dependence of the GDR centroid energy and width. It has been observed that the GDR centroid energy is nearly independent of the excitation energy and spin of the compound nucleus [Gaa92, Har01]. This is also expected from the theoretical estimates since both the nuclear size and the symmetry coefficient depend weakly on the temperature T. However, the apparent GDR width has been found to increase with both J and T of the compound nucleus [Gaa92, Sno86, Sri09, Har01].

### 1.4.1 J-dependence of the GDR width

Several studies of the GDR $\gamma$-decay in hot, rotating nuclei have showed that the GDR width remains roughly constant upto a critical angular momentum ($J_c$=0.6A$^{5/6}$) and increases rapidly at higher values of J [Har01, Kus98, Mat97]. This J-dependence of the GDR width is described reasonably well within the thermal shape fluctuation model (TSFM) [Alh99, Kus98]. As the rotational frequency becomes larger, the nucleus undergoes an oblate flattening due to centrifugal effects. The equilibrium deformation ($\beta_{eq}$) increases rapidly with J and, as a consequence, the total GDR strength function undergoes splitting which increases the overall width of the resonance. Also the thermal fluctuation of shape about this equilibrium deformation plays an important part in the increase of GDR width. However, even though the equilibrium deformation of a nucleus increases with J, an increase of GDR width is not evident experimentally until the equilibrium deformation increases sufficiently to affect the thermal average [Mat97]. In particular, as long as $\beta_{eq}$ is less than the variance $\Delta\beta = \left[\langle\beta^2\rangle - \langle\beta\rangle^2\right]^{1/2}$ the increase of GDR width is not significant. Thus, the competition between $\beta_{eq}$ and $\Delta\beta$ give rise to the critical angular momentum observed in the experiments. The variation of $\beta_{eq}$ and $\Delta\beta$ as a function of J for $^{106}$Sn at T = 1.8 MeV is shown in Fig.1.7(a) [Mat97]. A systematic study of the thermal shape fluctuation model has revealed the existence of a universal scaling law for angular momentum in terms of reduced width and reduced

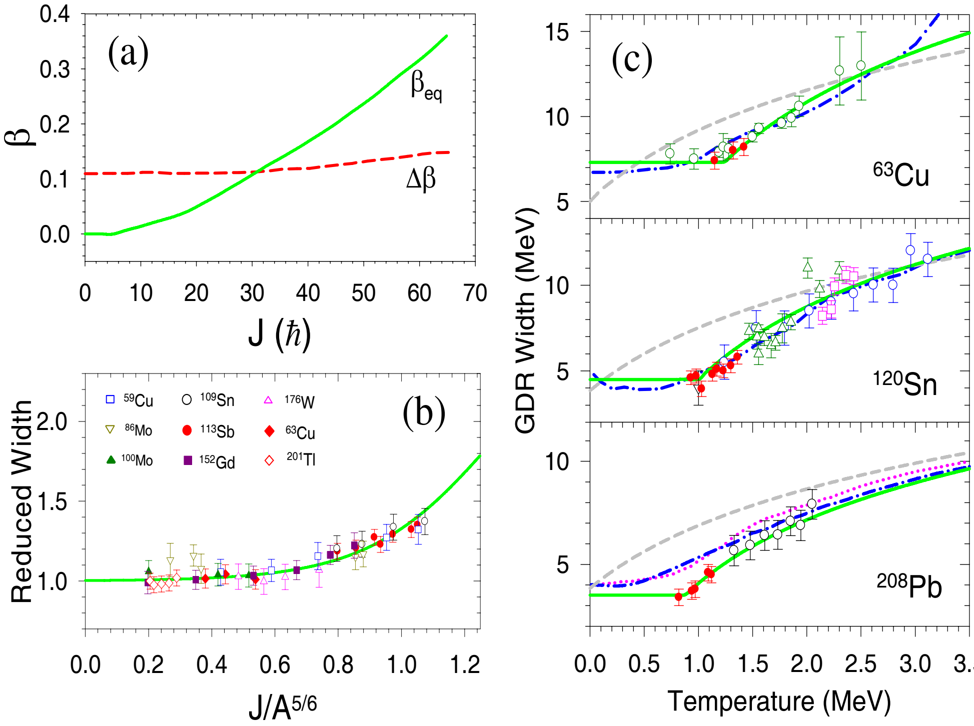


Figure 1.7: *(a) Evolution of the equilibrium deformation for $^{106}$Sn as a function of the angular momentum (continuous line). The dashed line shows the value of the variance of the deformation ($\Delta\beta$). (b) The reduced GDR widths are plotted against the reduced parameter $J/A^{5/6}$ for different nuclei. The symbols represent the experimental data while the continuous line refers to the theoretical prediction. (c) The GDR widths as a function of T for $^{63}$Cu, $^{120}$Sn and $^{208}$Pb. The different symbols represent the experimental data. The dashed, continuous and dot-dashed lines correspond to the prediction of TSFM, CTFM and PDM, respectively. The dotted line in $^{208}$Pb panel is the shell effect included TSFM calculation [Orm96].*

parameter J/A$^{5/6}$ shown in Fig.1.7(b) [Kus98, Dee12].

### 1.4.2 T-dependence of the GDR width

A wealth of GDR data, built on excited states, show that the GDR width remains more or less constant till T∼1 MeV and increases thereafter with T [Muk12, Dee12, Dan11, Kel99, Kus98, Orm96]. The increase of the GDR width above T≥1.5 MeV can be explained reasonably well within the TSFM [Alh99, Kus98, Har01]. The model proposes that the nucleus does not posses a single well-defined shape but rather explores a broad ensemble of mostly quadrupole shapes because of thermal fluctuation around an equilibrium shape given by (T, J). Thus, in adiabatic assumption, the observed GDR width then results from a weighted average over all frequencies associated with the possible shapes. This gives rise to T-driven broadening of the width. However, the model fails to explain the experimental data below T$\leq$1.5 MeV in different mass regions [Muk12, Dee12, Dee10b, Hec03, Cam03, Kus98]. Recently, it has been shown that the GDR vibration itself produces a quadrupole moment causing the nuclear shape to fluctuate even at T=0 MeV [Dee12]. Therefore, when the giant dipole vibration, having its own intrinsic fluctuation is used as a probe to view the thermal shape fluctuations, it is unlikely to feel the thermal fluctuations that are smaller than its own intrinsic fluctuation. The discrepancy between the experimental data and the TSFM predictions at low T is attributed to the competition between the GDR induced fluctuation ($\beta_{GDR}$) and the variance of the deformation ($\Delta\beta$) due to thermal fluctuations, which in turn gives rise to a critical temperature ($T_c$) in the increase of the GDR width. It is also shown that $T_c$ follows a 1/A dependence which is consistent with the experimental results. A new model has been proposed by modifying the phenomenological parameterization (pTSFM) based on TSFM by including the GDR induced qradrupole moment and is termed as critical temperature included fluctuation model (CTFM) [Dee12]. This model gives a good description of the GDR width systematics for the entire range of mass, spin and temperature.

The microscopic phonon damping model (PDM), on the other hand, attributes this increase of the GDR width to the coupling of GDR phonon to particle-particle and hole-hole configurations [Dan98]. The model calculates the GDR width and the strength function directly in the laboratory frame without any need for an explicit inclusion of thermal fluctuation of shapes. This model also gives a very good description of the GDR width as function of T. However, the PDM does not have a built-in angular momentum dependence of the GDR width at finite temperatures and may, therefore, be used only to describe the temperature dependence at zero spin. The GDR widths predicted within the PDM[Dan11], CTFM[Dee12] and pTSFM[Kus98] for $^{63}$Cu, $^{120}$Sn and $^{208}$Pb as function of T are shown in Fig.1.7(c).

## 1.5 Effect of deformation on the GDR

The nucleus in the ground state can be spherical or deformed. The GDR can probe the shape of the nucleus because the GDR resonance energy is inversely proportional to the nuclear radius along which the vibration occurs. The nuclear radius for a deformed nucleus is given by

$$R(\theta,\phi) = R_0\left[1+\sum_{\lambda,\mu}\alpha_{\lambda,\mu}Y_{\lambda,\mu}(\theta,\phi)\right] \tag{1.5}$$

where $R_0$ is the equilibrium radius and $R(\theta,\phi)$ the distance of the nuclear surface from the origin. The coordinates $\alpha_{\lambda,\mu}$ are the spherical tensor components ( which transform as spherical harmonics under rotation of the coordinate system) and give the extent of the deformation. $\lambda$ is the multipolarity of the deformation. Here only quadrupole deformations will be considered. The deformation parameters $\alpha_{\lambda,\mu}$ can be expressed in terms of the intrinsic deformation parameters $a_{20}$, $a_{21} = a_{2-1}$ and $a_{22} = a_{2-2}$ via a rotation from the body-fixed frame to the laboratory frame. The orientation of these two frames with respect to each other is uniquely defined by the Euler angles $\omega = (\phi,\theta,\psi)$. The transformation relations are given by

$$\alpha_{2\mu} = \sum_{\lambda} D_{\lambda\mu}(\omega)a_{2\lambda} \tag{1.6}$$

The two non-vanishing intrinsic variables $a_{20}$ and $a_{22}(= a_{2-2})$ are expressed in terms of the deformation parameters [Boh75] $\beta$ and $\gamma$ and are defined as

$$a_{20} = \beta\cos\gamma \tag{1.7}$$

$$a_{22} = \frac{1}{\sqrt{2}}\beta \sin\gamma \tag{1.8}$$

The parameter $\beta$ gives the magnitude of deformation. The value of the parameter $\gamma$ is defined as 0° for an axially prolate shape, 60° for an axially symmetric oblate shape and in between for triaxial nuclei. In the body fixed frame, the ellipsoidal shapes are described as

$$R_k = R_0\, exp\left[\sqrt{\frac{5}{4\pi}}\beta\cos\left(\gamma - \frac{2\pi k}{3}\right)\right] \tag{1.9}$$

with $k = 1, 2, 3$ denoting the three principal axes. The frequencies of vibration are inversely proportional to the lengths of the axes and are given by

$$\omega_k = \omega_0\, exp\left[-\sqrt{\frac{5}{4\pi}}\beta\cos\left(\gamma - \frac{2\pi k}{3}\right)\right] \tag{1.10}$$

Danos [Dan58] investigated the coupling of the GDR to the shape degrees of freedom in the framework of hydrodynamical model. It has been shown that in an axially symmetric deformed nucleus the ratio of the two resonance energies is related to the ratio of the corresponding lengths of the two axes by the following relation:

$$\frac{E_\perp}{E_\parallel} = 0.911\frac{R_\parallel}{R_\perp} + 0.089 \tag{1.11}$$

$E_\perp(E_\parallel)$ in this equation denotes the vibration perpendicular (parallel) to the symmetry axis. Using the equation (1.9) and (1.11), the following expression for $\beta$ in terms of the resonance energies can be obtained:

$$\beta = \sqrt{\frac{4\pi}{5}}\left(\frac{\delta - 1.0}{0.5\delta + 0.87}\right) \tag{1.12}$$

where $\delta = E_\perp/E_\parallel$

At $T \geq 1.5$ MeV, where shell effects have melted [Boh75], a rotating nucleus will behave like a rotating liquid drop [Coh74]. Owing to the centrifugal force at high spin, the nucleus undergoes a Jacobi shape transition (Fig.1.8), an

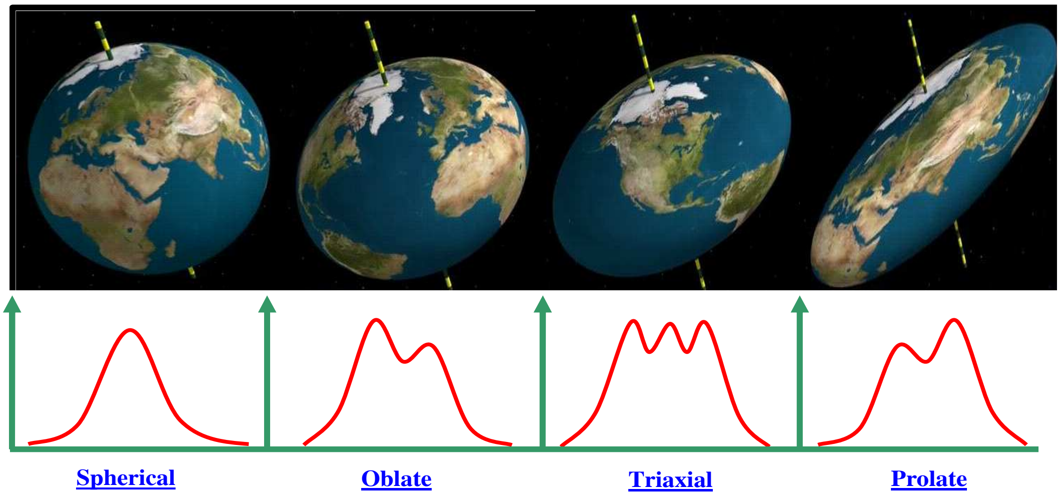


Figure 1.8: *The Jacobi shape transition is shown schematically. Due to high rotation the spherical shape changes to an oblate shape rotating parallel to the symmetric axis and finally to a collective prolate shape rotating perpendicular to the symmetry axis. The corresponding GDR lineshape (idealized) is shown below for all the shapes (continuous line).*

abrupt change of shape from an oblate ellipsoid rotating around the symmetry axis to an elongated prolate or triaxial shape rotating perpendicularly around the symmetry axis, similar to one, which occurs in gravitating rotating stars [Cha69].

In practice, the required fast rotations for the oblate to triaxial transition can only be achieved in light and medium nuclei as fission barrier vanishes for such high rotational frequencies for heavier nuclei. Since, the GDR strength distribution reflects the nuclear shape such a transition might show up in the GDR $\gamma$-spectra. The idealized GDR lineshapes for the different shapes of the nucleus are depicted in Fig.1.8. The main problem, however, arises due to the thermal shape fluctuation, which smears out the associated splitting of the strength function resulting in an overall broadening of the distribution and making direct identification of the shape transition very difficult. The confirmation then has to come from a comparison of the experimental data and theoretical calculation based on the expected shape transition. The giant dipole resonance strength function in hot rotating nuclei at finite temperature has been discussed in the framework of the thermal shape fluctuation model [TSFM] which accounts for adiabatic, large-amplitude thermal fluctuations of the nuclear shapes [Gal85, Alh86, Alh87, Alh93, Orm99]. Different models have been developed under its framework following an exact treatment of the fluctuations [Aru04] and using the LSD model for liquid drop energy [Pom03, Maj04, Dub05]. TSFM has been successfully utilized to explain the deformation and the Jacobi shape transition in light mass system [Maj04, Dee10a].

## 1.6 Motivation

The goal of the experimental research presented in this thesis is the investigation of the nuclear deformation in light $\alpha$ and non-$\alpha$ like systems by measuring the high-energy $\gamma$-rays from the decay of GDR in heavy ion induced reactions and the emission of high-energy $\gamma$-rays from the coherent nucleus-nucleus bremsstrahlung in $^{252}$Cf spontaneous fission.

### High energy $\gamma$-rays from spontaneous fission of $^{252}$Cf

Fission is a nuclear reaction or a radioactive decay process in which the nucleus of an atom splits up into two approximately equal parts (addressing different aspects of nuclear physics). After more than fifty years of continuous investigations, a number of interesting questions are still unanswered. For many years, measurements addressing the fission process have concentrated on particle emission from fissioning nuclei. Only a few experiments have been performed on the high-energy part of the $\gamma$-spectrum coming from spontaneously fissioning nuclei, although it has been suggested to contain specific information on the dynamical features of fission. The high-energy $\gamma$-ray photons, above 20 MeV, emitted in the spontaneous fission of $^{252}$Cf have been one of the fundamental problems of nuclear fission physics.

For $\gamma$-ray energies above 20 MeV, both experimental data and theoretical calculations are contradictory. In several experiments, the yield of $\gamma$-rays with such a high energy was not detected, and only an upper bound was determined [Luk91, Die74]. In three other experiments, the energy spectrum was measured [Kas89, Ple92, Var05]. The yield of $\gamma$-rays with energies 20 - 120 MeV is theoretically attributed to the coherent bremsstrahlung of the fission fragments accelerating in their mutual Coulomb field. A detailed macroscopic calculation of the bremsstrahlung yield from the spontaneous fission source has been performed considering different acceleration mechanisms (instantaneous, pure Coulomb) [Kas89, Luk91]) and also including the quantum-mechanical corrections for the effect of tunneling of the fragments through the potential barrier [Luk91]. However, the calculations in different models differ by several orders of magnitude. Thus, the conflicting theoretical predictions as well as the experimental results motivate one to carry out further investigation of the high energy $\gamma$-rays ($>$ 20 MeV) emitted in the spontaneous fission of $^{252}$Cf.

## Giant Dipole Resonance $\gamma$-rays from hot $^{47}$V nucleus

Hot nuclei are formed in heavy ion fusion reactions where the relative kinetic energy of the colliding nuclei is converted into internal excitation energy and angular momentum of the compound nuclei. Rapidly rotating light nuclei in general are likely to undergo Jacobi shape transition at an angular momentum value lower than that of the fission limit, where the shape changes abruptly from non-collective oblate to collective triaxial and/or prolate shape (Fig.1.8). Since it is possible for the light mass nuclei to attain very high angular velocities beyond the critical point for Jacobi transition without undergoing fission, existence of exotic shapes in nuclei with a large deformation becomes a possobility. Signatures of such shape transitions in $^{45}$Sc [Kin93] and $^{46}$Ti [Maj04, Kmi07] have been reported from the study of lineshapes of giant dipole resonance (GDR) built on excited states. Apart from the GDR $\gamma$-rays, the occurrence Jacobi shape transition has also been confirmed for $^{48}$Cr [Sal08] from high-spin spectroscopy and corresponding theoretical calculation using the LSD liquid drop model [Pom03].

The deformation of the excited $^{47}$V nucleus has been estimated earlier from the inclusive $\alpha$-particle spectrum [Apa06] in the reaction $^{20}$Ne + $^{27}$Al $\rightarrow$ $^{47}$V. This nucleus is also expected to undergo Jacobi shape transition similar to $^{46}$Ti [Maj04]. For non-$\alpha$ like $^{47}$V system, it is well established that there is no significant entrance channel effect and the fusion fission compound nuclear yield is dominant in accordance with the qualitative expectation from the number of open channel model [Ray91, Bec93]. The $\alpha$-spectroscopic studies, however, can only indicate overall deformation in an indirect way. Hence, it is worthwhile to complement the above study with the investigation of the nuclear structure of excited rotating systems via the GDR $\gamma$ decays in a more direct manner.

### Giant Dipole Resonance $\gamma$-rays from hot $^{32}$S nucleus

The phenomena of clustering and large deformations in light $N = Z$ nuclei has recently evoked a lot of interest and a few attempts have been made to study the characteristics of such light, highly deformed systems [Hor04, Bec09]. Such large deformations observed in light $\alpha$-like systems are believed to be due to the occurrence of either quasimolecular resonances or nuclear orbiting [San99], which has the origin in $\alpha$-cluster structure of these nuclei. In fact, the orbiting yield has been found to be dominant in $\alpha$-like systems due to small number of open channels available to carry away the grazing angular momentum [Ray91].

The $^{20}$Ne + $^{12}$C populating $^{32}$S is a well-established orbiting system [Sha79]. Our previous studies on enhancement of fragment yield near the entrance channel [Cha05] as well as $\alpha$-spectroscopic studies on this system [Apa06] have strongly indicated a highly deformed orbiting dinuclear shape for this system. Interestingly, in self-conjugate nuclei, the $\gamma$-ray yield from the decay of the GDR populated by T=0 entrance channel is found to be strongly inhibited due to the isovector nature of the electric dipole radiation [Har86]. In particular, the E1 GDR decays from T=0 to T=0 states are isospin forbidden. However, it has been found that the yield of the high energy $\gamma$-rays from N=Z compound nuclei increases in the presence of isospin mixing [Har86, Beh93, Kin04]. In heavy ion collisions at projectile energies above 6 MeV/nucleon, it is known that incomplete fusion and pre-equilibrium emission processes also occur. Hence, the high energy $\gamma$-rays will not only arise from N=Z compound nuclei but may also follow from incomplete fusion and pre-equilibrium emission [Kin04]. In this case, the mass and charge of the compound nucleus as well as the excitation energy are expected to be lower than in case of complete fusion. Moreover, bremsstrahlung $\gamma$-ray emission should also be included in the analysis [Kin04]. It is, therefore, relevant to explore the relationship between the shapes of the light $\alpha$-like systems and the corresponding Jacobi shapes directly through the GDR $\gamma$ decays at projectile energies above 7 MeV/nucleon, which would help in understanding the reaction dynamics of light $\alpha$-like systems and the role played by $\alpha$-clustering in determining the shape of these nuclei.

The aim of the present study is to make quantitative experimental estimation of the deformed shapes of light $\alpha$ and non-$\alpha$ systems using GDR lineshape studies and compare them with the corresponding predictions for equilibrium Jacobi shapes.

The description of the high-energy photon spectrometer LAMBDA and the high-energy $\gamma$-ray measurement from $^{252}$Cf spontaneous fission source are discussed in chapter two. The statistical model to interpret the high-energy $\gamma$-ray spectra and the thermal shape fluctuation model to study the shape transition in nuclei are discussed in chapter three. The development of 50-element multiplicity filter for the measurement of angular momentum and the decay of GDR $\gamma$-rays from hot $^{47}$V nucleus are discussed in chapter four while the measurement of the GDR $\gamma$-decay from hot $^{32}$S nucleus is discussed in chapter five. Finally in chapter six, summary and conclusion of the present work is discussed.

# Chapter 2

# High-energy $\gamma$-rays from spontaneous fission of $^{252}$Cf

## 2.1 Introduction

Fission is a mode of nuclear reaction in which a massive nucleus splits into smaller nuclei with the simultaneous release of energy ($\sim$ 200 MeV). This nuclear phenomenon can occur spontaneously as a natural decay process or can be induced by the excitation of the nucleus by photons, neutrons or charged particles. $^{252}$Cf undergoes $\alpha$-decay 96.9% of the time while the remaining 3.1% of decays are spontaneous fission with a half life of 2.645 years. In spontaneous fission, the high-energy gamma rays ($<$ 20 MeV) are emitted by the excited fission fragments. The excitation energy in the fragments originate from two sources: a) the excitation energy of the system at scission is shared by the fragments and b) the deformation energy of each fragment at a near scission point is converted to excitation energy shortly after separation [Hof93] (when the equilibrium shape is attained).

The photons from spontaneous fission in the energy range 20-120 MeV are associated with the coherent nucleus-nucleus bremsstrahlung of the fission fragments in the Coulomb field. In the recent past, a detailed macroscopic calculation of the bremsstrahlung yield from the spontaneous fission source has been performed considering different acceleration mechanisms (instantaneous, pure Coulomb) [Kas89, Luk91], including fragment-fragment barrier penetration (tunneling). However, the high-energy photon spectra predicted by these different models differ by several orders of magnitude. Moreover, in few experiments [Luk91, Die74], the yield of $\gamma$-rays with such high-energy were not detected while in other three experiments, the energy spectrum was measured [Kas89, Ple92, Var05]. Thus, both the experimental data and theoretical calculations are conflicting and require further investigation.

An extensive experiment was performed using the LAMBDA spectrometer to investigate the high-energy $\gamma$-ray yield from the coherent nucleus-nucleus bremsstrahlung from the $^{252}$Cf spontaneous fission [Dee10b].

## 2.2 LAMBDA spectrometer

A suitable detector system is an important part of the high-energy $\gamma$-measurement. The high-energy $\gamma$-rays interact with the detector material mainly via $e^+ - e^-$ pair productions and produce an electromagnetic shower. In order to get proper energy information, the detector material should confine this shower effectively. Therefore, a good high-energy $\gamma$-ray detector should have a large interaction volume and high $\gamma$-detection efficiency.

Generally, NaI(Tl) and $BaF_2$ scintillators are used for high energy $\gamma$-detection in this energy range [Kno99]. The energy resolution of $BaF_2$ is ideally a factor of two or three worse than that of its best NaI(Tl) counterpart, but they are comparable in terms of detection efficiency. The gain variation of $BaF_2$ is also significant with temperature. Still, $BaF_2$ is superior to NaI(Tl), especially in those applications where fast timing is essential, and the poorer energy resolution gets compensated by the much better timing characteristics of $BaF_2$. Other


Figure 2.1: *The LAMBDA spectrometer arranged in three 7×7 matrix.*

major advantages of using $BaF_2$ scintillator are that it is non-hygroscopic and has a very low neutron capture probability. The important properties of $BaF_2$ are listed below:

- Radiation length = 2.05 cm.
- Moliere radius = 3.39 cm.
- Mass density = 4.88 gm/cm$^3$.
- Scintillation light consists of two components. The fast component (20%) peaking at $\lambda$ = 220 nm (time constant 0.6 ns) and the slow component (80%) peaking at $\lambda$ = 320 nm (time constant 630 ns). Thus, the fast component provides the timing signal and the slow component provides a measure of the deposited energy.

Recently, a promising scintillator detector $LaBr_3$:Ce (Lathanum Bromide Cerium doped) has been developed which has high light output, fast response and therefore shows very good energy and time resolution [Van02]. The typical energy resolution at 662 keV is 3% as compared to NaI detectors at 7%. The scintillation light output peaks at 380 nm and has a decay time $\leq$ 25 ns. The density of the crystal is 5.29 gm/cc. However, the crystals are very expensive and large size $LaBr_3$:Ce crystals are not yet available compared to NaI and $BaF_2$.

At the Variable Energy Cyclotron Centre, Kolkata, India, a large array of $BaF_2$ detectors has been designed, developed and fabricated. LAMBDA [Muk07] is the acronym of **L**arge **A**rea **M**odular **B**a$F_2$ **D**etector **A**rray. The entire detector system has been fabricated from bare $BaF_2$ crystals with indigenous in-house expertise. The gamma spectrometer consists of 162-individual detector elements in a planar and modular geometry, each detector having a cross-section of 3.5cm x 3.5cm and a length of 35 cm. A fast photo multiplier tube (PMT) (Phillips XP2978) of 29 mm diameter with a quartz window is coupled with the scintillators. The detector system is highly granular which greatly reduces the possibility of any $\gamma\gamma$ and $\gamma$-neutron pile up events in in-beam experiments. Being modular in nature, the array can be arranged in different geometries, e.g., two 9 x 9, three 7 x 7, or six 5 x 5 matrix formations and placed at different angles with respect to the beam axis. The details of the development and fabrication of the spectrometer can be found in Ref[Muk07]. The LAMBDA spectrometer arranged in three 7 x 7 matrix is shown in Fig.2.1.

## 2.3 Energy and time resolution

The detectors were tested for energy resolution using the $^{137}$Cs (0.662 MeV), $^{22}$Na(0.511 MeV, 1.274 MeV), $^{60}$Co(1.17 MeV, 1.33 MeV) and $^{241}$Am-$^{9}$Be (4.43 MeV). The energy resolution was plotted as function of $1/\sqrt{E}$. A straight line passing through the origin was fitted which gave energy resolution (%) $= 16/\sqrt{E}$ Ref[Muk07]. For energy of 4.43 MeV, the energy resolution lies between 8% - 9%.

The time resolution of an individual detector was measured with respect to

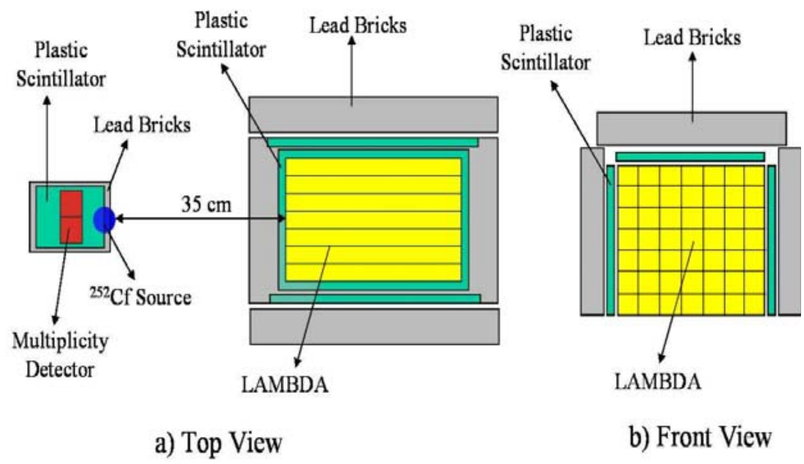


Figure 2.2: *(a) The schematic view (top) of the experimental setup and (b) Front view of the LAMBDA spectrometer.*

another similar detector with a $^{60}$Co source. The source was placed in between two identical detectors, kept at 180° apart. The energies and their relative times of arrival were measured simultaneously in event by event mode. The value of time resolution obtained was 960 ps. The details of the performance of the detectors are presented in Ref[Muk07, Sri09].

## 2.4 Experiment and data analysis

High-energy $\gamma$-rays from the spontaneous fission of $^{252}$Cf (3$\mu$Ci) were detected in coincidence with the low energy discrete $\gamma$-rays emitted from the decay of excited fission fragments in order to establish a correlation (photons/fission) between the high energy $\gamma$-rays and the fission process. The source was placed as close as possible to the four $BaF_2$ multiplicity detectors (3.5cm x 3.5cm x 5cm ) [Dee10c], arranged in a 2×2 matrix, to get a start trigger in order to separate/reject the neutrons and the cosmic pile-ups in the high energy spectrometer. The high-energy $\gamma$-rays were measured using the array LAMBDA [Muk07]. The array was assembled in a 7×7 matrix and kept at a distance of 35 cm from the $^{252}$Cf source covering a solid angle of 3.5% of $4\pi$. A master trigger was generated by taking a coincidence between the start trigger and any one of the 49 detectors in the pack above a high threshold of 4 MeV ensuring the selection of fission events and rejection of background. At the photon energies $E_\gamma > 25$ MeV, cosmic ray showers are the major source of background. Therefore, extreme precaution was taken to suppress the background and obtain the experimental data free from cosmic impurity. A 10 cm thick lead shielding was placed on the top and the two sides of the detector array to cut down the $\gamma$-rays from the cosmic background. Large area plastic scintillators pads (paddle) were used as active shielding that surrounded the LAMBDA array as well as the multiplicity filter to reject the cosmic muons. The schematic view of the setup is shown in Fig.2.2. The data were collected in this $\gamma$-$\gamma$ mode for 450 hrs.

### 2.4.1 Front-end electronics and data acquisition

A dedicated front-end electronic set-up developed for the LAMBDA spectrometer was used for generating a clean, valid trigger to register the energy and time information from each detector element in an event-by-event mode. Commercially available high-density programmable CAMAC modules were used in the experiment. All the electronics and Data Acquisition (DAQ) systems kept inside the experimental hall were controlled from outside over Ethernet. A dedicated VME data acquisition (DAQ) system running under LINUX environment, developed at VECC was used to acquire the data. Fast 12 bit, 32 channel VME charge to digital converter (QDC) (Model: CAEN V792) and time to digital converters (TDC) (Model: CAEN V775) were used for energy and time measurements, respectively. These modules have a conversion time of 5.6 $\mu$s for all its 32 channels. The QDCs can handle a maximum input charge of 400 pC while the TDCs have a dynamic range of 140 ns to 1200 ns. The DAQ can handle about 4k events/sec with a negligible dead time loss.

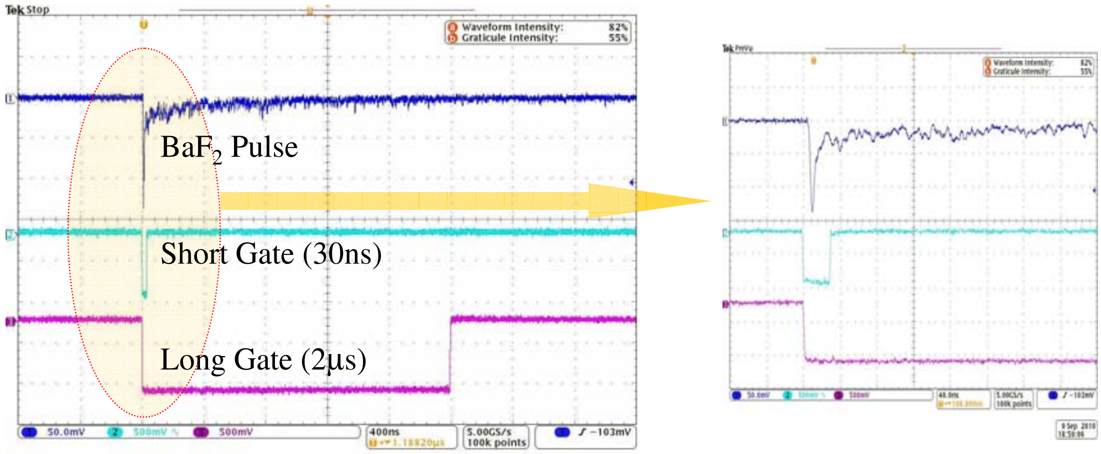


Figure 2.3: *(a) The long gate and short gate for pulse shape discrimination (PSD) along with an unattenuated $BaF_2$ signal.*

In this electronics scheme, the neutrons were rejected by time of flight (TOF) and pile-up events were rejected using pulse shape discrimination (PSD) in each detector element. Each of the signals in the analog path was split into two parts, with an amplitude ratio of 1:10 before sending them to a pair of QDCs for long and short integration. The amplitude ratio was chosen in such a way, so that approximately equal amounts of charge was integrated under the long and short gates forming a $\gamma$-band making approximately a 45° slope in the 2-dimensional short vs. long energy spectrum. A typical unattenuated signal from $BaF_2$ detector along with short gate (30ns) and long gate (2$\mu$s) is shown in Fig.2.3. The detailed electronic scheme is described later in chapter 4.

The energy calibration of the $BaF_2$ detector assembly was done using laboratory standard $\gamma$-rays sources $^{22}$Na (0.511 MeV, 1.274MeV), $^{137}$Cs(0.662 MeV), $^{241}$Am - $^{9}$Be (4.44 MeV) and minimum ionizing cosmic muons (23.1 MeV). These muons deposit 6.6 MeV/cm in $BaF_2$ material, thus while traversing the width of the detector (3.5 cm) vertically they deposit 23.1 MeV of energy in the detector volume and provide a high-energy calibration point [Muk07].

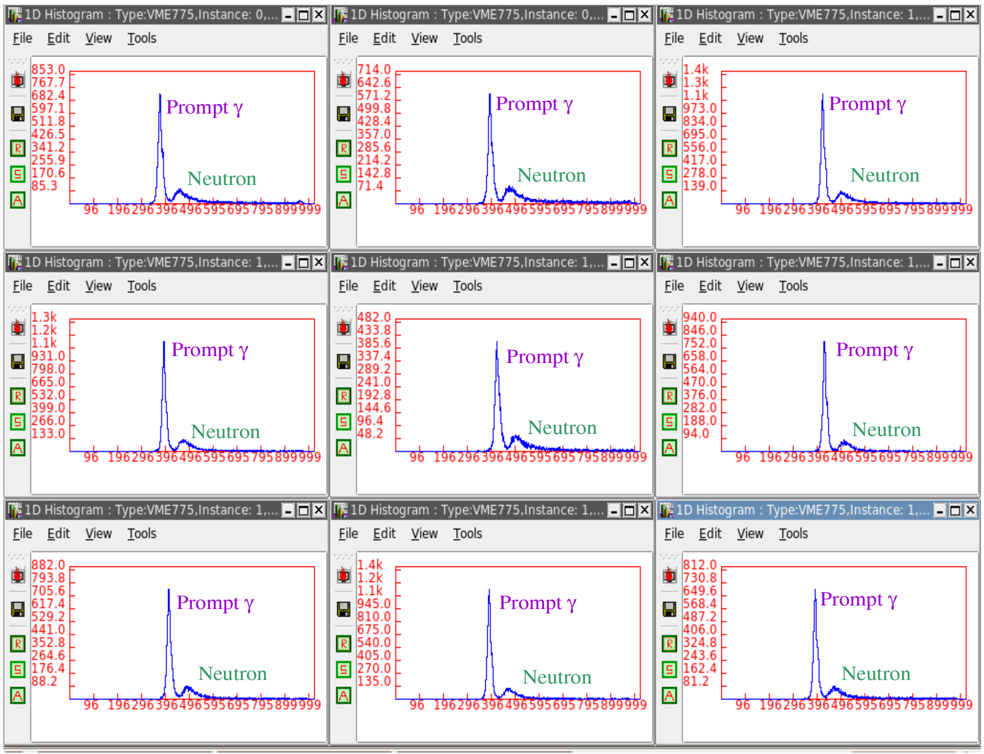


Figure 2.4: *The time of flight (TOF) spectrum during online experiment.*

### 2.4.2 Rejection of neutrons, pile-up and cosmic events

Slower neutrons, interact in the $BaF_2$ material primarily by (n,$\gamma$) or (n,n$'$,$\gamma$) reactions and deposit their energy in the detector as photons. On the other hand, the fast neutrons interact via (n,p) or (n,n$'$,p) reactions and the knocked out protons in turn deposit their energies in the detector. Thus, it is not possible to identify and separate the slow neutrons by pulse shape discrimination (PSD) alone. These neutrons are discriminated mainly by their time of flight (TOF). Utilizing the fast timing properties of $BaF_2$, these neutrons can be effectively rejected by the selection of prompt $\gamma$-rays from the TOF spectrum (Fig.2.4) for the individual detector elements. The master trigger was used for generating the common-start trigger of the TDCs and each TDC was stopped by the individual delayed outputs from the CFDs (with a uniformly low threshold of 300 keV) for

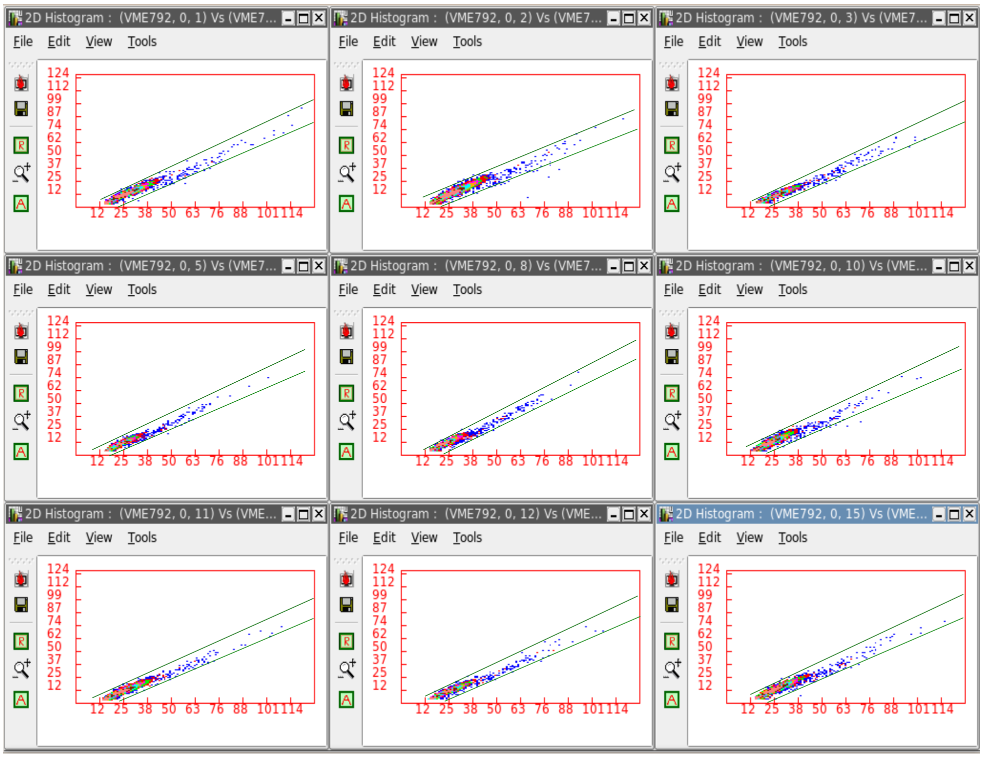


Figure 2.5: *The pulse shape discrimination (PSD) spectrum during online experiment. The selection of $\gamma$-band is shown with continuous line.*

the generation of the individual time spectrum for each element of LAMBDA. The time of flight spectrum from individual detector elements during an online experiment is shown in Fig.2.4. The prompt $\gamma$-ray and neutron peaks are shown in the figure. A clear separation of $\gamma$-rays and neutrons are obtained.

The pile-up events occur mainly when, along with a valid high-energy photon event in a single detector element, another photon or neutron enters the same element while the integration gates are open. The pile-up events are rejected by the PSD method as discussed in section 4.2.1. In the experiment, the master trigger was used for generating the integration gates (2$\mu$s, 30ns). The PSD spectrum from individual detector elements during online experiment is shown in Fig.2.5. The ($\gamma$, $\gamma$) or ($\gamma$, n) hits in the same element in the same event during the integration will result in a different ratio of short to long gate

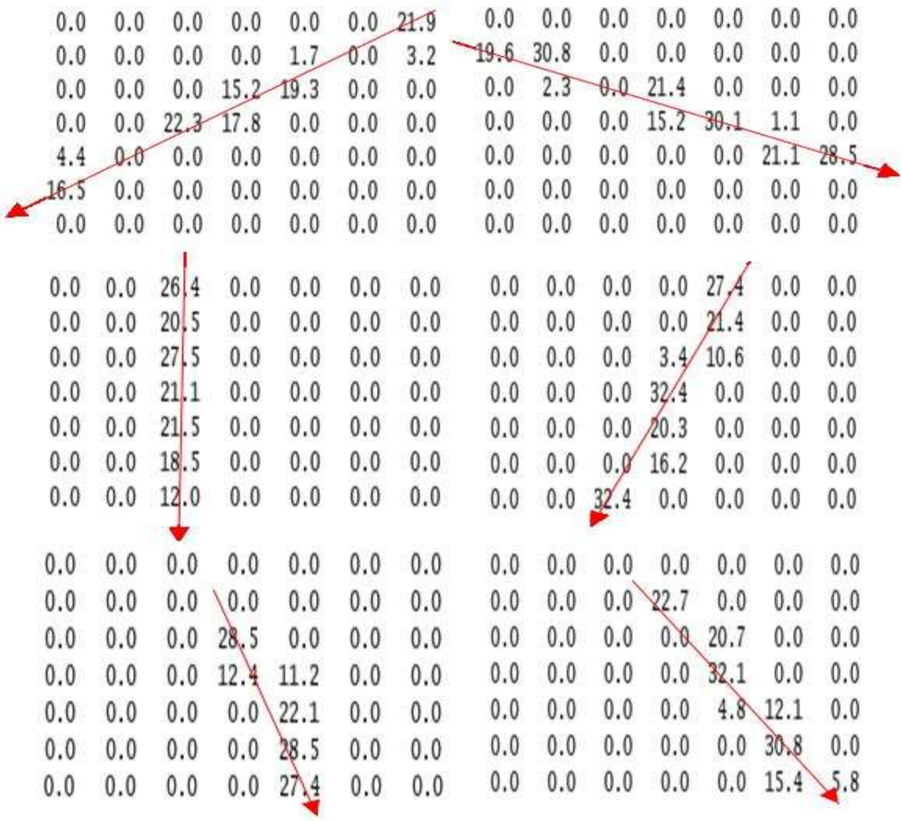


Figure 2.6: *The typical cosmic muon tracks in LAMBDA spectrometer arranged in 7×7 matrix. The direction of the muon tracks are shown by the arrows along with the actual energy deposits in the detector elements.*

integrated charge and will appear away from the true $\gamma$-band in short vs. long 2 dimensional spectrum for the individual detectors. A suitable selection of the true $\gamma$-band effectively rejects these pile-up events Fig.2.5. However, the pile-up events are negligible due to large granularity of the LAMBDA spectrometer.

The high-energy cosmic muons coming from the top and the sides of the spectrometer produce a hit pattern which is completely different from the high-energy photons. These minimum ionizing cosmic muons deposit an energy of 6.6 MeV/cm in the detector material ($BaF_2$) while traversing in straight paths through the array. When passing vertically through the array, they deposit 23.1 MeV in each detector in its path (for a detector thickness of 3.5 cm). This

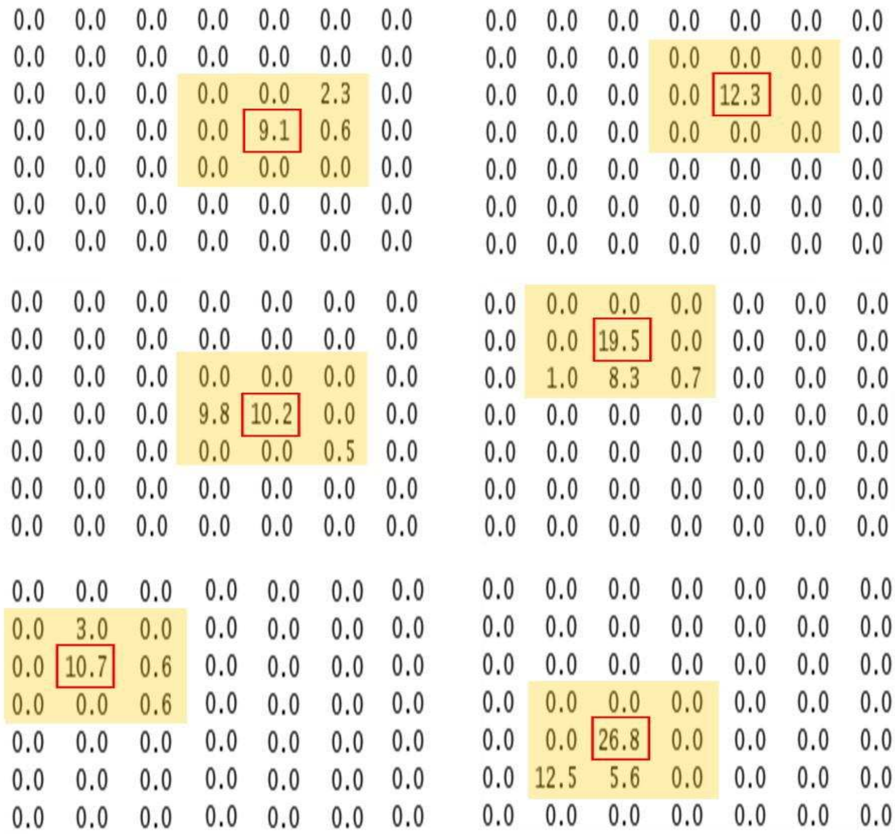


Figure 2.7: *The cluster summing technique of the LAMBDA spectrometer arranged in a 7×7 matrix. The cluster is shown as a shaded rectangle while the central detector of cluster is marked with box.*

property is used for calibrating the detectors at higher energy. For diagonal and oblique entry, these energy deposits will be higher. The typical cosmic muon tracks in the spectrometer are shown in Fig.2.6. During offline analysis, these muons are effectively rejected due to their unique hit patterns in the array.

### 2.4.3 Event reconstruction

The high-energy $\gamma$-ray spectrum is generated in the offline analysis by using a nearest neighbor (cluster) summing technique [Muk07]. In this technique, first, the detector with highest energy deposit above a high threshold ($\geq$ 4 MeV) within the array is identified as the primary detector. In order to gather the full energy information of the incident photons, it is important to confine the secondary electromagnetic shower within the array volume as far as possible. Therefore, a check is done to find whether the primary detector is surrounded by all its neighbors. The event is treated as valid, if this condition is satisfied. Otherwise, due to the possibility of losing a part of the electromagnetic shower (for events near the edges), the event is rejected. In the case of a valid event, for the final adding back, only those detectors are considered among the 8 nearest neighbors, having an energy deposit $>$ 300 keV. Next, it is checked if the energy deposited in the primary detector satisfies the time of flight and pulse shape discrimination gating conditions. If satisfied, the energy deposited in the primary detector is added with those of its nearest neighbors after applying the TOF and the PSD gate conditions in all of them. If any of them does not obey these conditions, the energy deposited in that detector is rejected. The cluster summing technique for the array arranged in 7x7 matrix is shown in Fig.2.7.

## 2.5 Result and discussion

The high-energy gamma spectrum was extracted from the binary list mode data recorded in the event-by-event mode. The list file contained the information of the energy deposited in each of the detectors of the large array and the relative time information. A data analysis computer program was developed for the analysis under the framework of CERN ROOT. In each event, all the detectors were checked, applying pulse shape discrimination and time of flight conditions for the rejection of neutrons and pile up events. After application of different conditions, in a valid event, the energy deposited in the detectors was summed-up using nearest neighbor event reconstruction technique. Finally, the random coincidence events were rejected by subtracting the background spectrum, which was also collected for 450 hours in an identical configuration without the fission

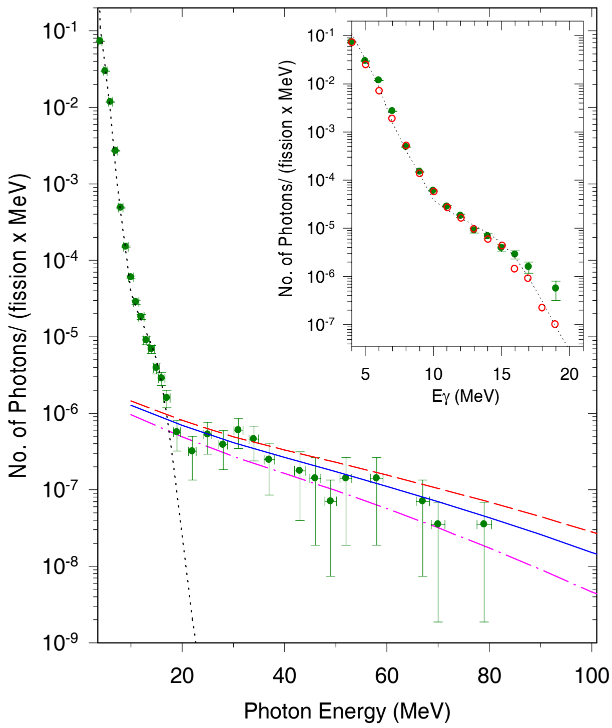


Figure 2.8: *The experimentally measured $\gamma$-spectrum (filled circles). The dotted line represents the CASCADE calculation. The dashed line represents the pure Coulomb calculation. The solid lines correspond to the calculation including conservation of energy while the dot-dashed line represents the calculation including both conservation of energy and pre-scission kinetic energy. [Inset] The experimental data compared with a previous result [Ple95] (open circle).*

source.

Interestingly, high-energy $\gamma$-rays greater than 20 MeV are observed in the experiment. The $\gamma$-ray spectrum measured upto 80 MeV is shown in Fig.2.8 (filled circles) [Dee10b]. The data below 20 MeV are also compared with the neutron corrected data (open circle, inset of Fig.2.8) obtained earlier in fission-$\gamma$ coincidence experiment [Ple95]. The gamma spectrum matches exceptionally well with the earlier measurement. As can be seen from Fig.2.8 that the slope of the $\gamma$ spectrum changes sharply after 20 MeV, clearly indicating that the mechanisms of the emission of photons below and above 20 MeV are completely different in origin. These high-energy $\gamma$-rays can only be emitted from the coherent nucleus-nucleus bremsstrahlung as the $^{252}$Cf nucleus has zero energy at the start.

In order to substantiate the experimental result, a theoretical calculation based on Coulomb acceleration model, in accordance with the work done by Luke et al. [Luk91], was performed to predict the estimated yield of these photons above 20 MeV. Equation 2.1 gives the exact energy spectrum of the bremsstrahlung produced from the acceleration of the two charged fission fragments in the classical non-relativistic limit [Luk91].

$$\begin{aligned}\frac{d^2N}{dE_\gamma d\Omega} =& \frac{\mu^2}{4\pi^2(\hbar c)c^2}\frac{e^2}{E_\gamma}\Bigg|\int dt[\hat{n}\times\ddot{x}] \\ &\cdot e^{-i\omega t}\left(\frac{z_1}{m_1}e^{i(\omega/c)(\mu/m_1)\hat{n}\cdot x} - \frac{z_2}{m_2}e^{i(\omega/c)(\mu/m_2)\hat{n}\cdot x}\right)\Bigg|^2\end{aligned} \tag{2.1}$$

In order to solve the above equation, time (t) was expressed as a function of the distance (x) between the two fragments. The motion of the fragments was determined by solving the differential equation for the two particles under the influence of a repulsive Coulomb potential

$$\frac{1}{2}\mu\dot{x}^2 + \frac{k}{x} = E \tag{2.2}$$

where k = $Z_1Z_2e^2$ and $E$ is the total energy of the system. The expression for $t(x)$ was calculated by solving Eq(2.2) and is given by

$$\begin{aligned}t(x) = \Bigg\{\sqrt{\frac{\mu}{2E}}\Bigg[&\sqrt{x^2 - \frac{kx}{E}} \\ &+ \frac{k}{2E}\ln\left(\left(x - \frac{k}{2E}\right) + \sqrt{x^2 - \frac{kx}{E}}\right)\Bigg]\Bigg\}_{x_{scission}}^{x}\end{aligned} \tag{2.3}$$

The expression of $t(x)$ in Eq(2.3) was substituted in Eq(2.1) to calculate the integral numerically in co-ordinate space. The minimum distance between the two fission fragments ($x_{scission} = Z_1Z_2e^2/E$) is critical and determines strongly the yield of the bremsstrahlung. For the most probable fission pair (A = 109, Z

= 43 and A = 143, Z = 55), the experimentally measured total kinetic energy is 187 MeV [Sch66] which yields a value of 18.2 fm for $x_{scission}$ assuming no pre-scission kinetic energy. Due to the tunneling process, the actual acceleration starts before scission and at the scission point the kinetic energy is about 25-30 MeV [Ple95a]. The corresponding values of $x_{scission}$ is 21.0 and 21.7 fm, respectively [Dee10b]. The classical bremsstrahlung takes over from that point. The calculation was performed for a distribution of the most probable masses and charges arising from the fission of $^{252}$Cf [Wah88] both including and excluding the pre-scission kinetic energy. The photon spectrum was averaged over the total solid angle considering an isotropic emission since the angular correlation between the fission fragments and the high-energy $\gamma$-rays could not be ascertained in this case. Finally, the estimated yields were folded with the detector response function [Muk07] to compare with the experimental data.

An attempt was made to include the conservation of energy by multiplying the bremsstrahlung yield with a factor of (1 - $\hbar\omega$/E), where $\hbar\omega$ is the energy carried away by the bremsstrahlung photons [Dee10b]. The theoretical predictions of the bremsstrahlung yield are shown in Fig.2.8. The dashed line represents the pure Coulomb calculation i.e. without taking into account the conservation of energy and pre-scission kinetic energy. The solid line corresponds to the calculation performed considering only conservation of energy while the dot-dashed line corresponds to the calculation taking into account both the conservation of energy and pre-scission kinetic energy ($x_{scission}$ = 21.7 fm corresponding to pre-scission kinetic energy of 30 MeV). As expected, the emission probability is suppressed for higher energies when the kinetic energy achieved before reaching scission point is taken into account. It is evident that when both conservation of energy and pre-scission kinetic energy is considered the approximate theoretical approach gives an excellent description of the experimental data. However, a de-

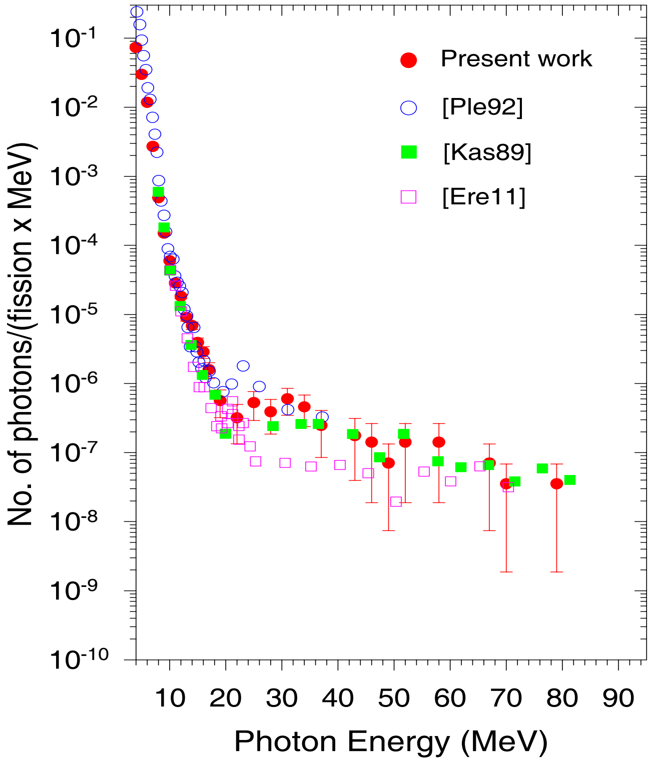


Figure 2.9: *The experimentally measured $\gamma$-spectrum compared with the data observed in other experiments.*

tailed quantum mechanical calculation is needed for a more realistic description and is beyond the scope of the present thesis.

The measured high-energy $\gamma$-ray spectrum is also compared with that of the earlier measurements employing $\gamma$-$\gamma$ coincidence method [Kas89] and fission fragment-$\gamma$ coincidence [Ple92] (Fig.2.9). As could be seen, our measurement agrees quite well with that of by Kasagi and his group earlier (green filled squares) in the range 8 - 80 MeV. Our result is also in agreement with the fission-$\gamma$ coincidence experiment where the high-energy $\gamma$-rays were observed only upto 38 MeV (blue open circle), except at energy around 25 MeV. The spectral discontinuity at 25 MeV was attributed to the prompt pile-up of the neutrons [Ple95a]. Recently, the high-energy $\gamma$-rays accompanying spontaneous fission of $^{252}$Cf was investigated in double and triple neutron-$\gamma$ coincidences

[Ere11] (pink open squares). The data differs about an order between 20 and 40 MeV but shows exactly a similar behaviour above 40 MeV. In the work of Luke [Luk91], the high-energy $\gamma$-ray above 20 MeV was not observed. They used complicated active and passive shielding in order to reduce cosmic ray background. It seems that they may have also reduced the true coincidence events because such $\gamma$-rays do not lose all its energy in the $\gamma$-detector and may have lost some part in the anticoincidence shielding. The high-energy $\gamma$-ray spectra measured in the different experiments show a very similar result at high-energy confirming the fact that nucleus-nucleus coherent bremsstrahlung photons are emitted in fission process. The results are also in agreement with the classical calculation based on the Coulomb acceleration model including conservation of energy and pre-scission kinetic energy.

A detailed statistical model calculation (CASCADE) was performed to explain the $\gamma$-ray yield below 20 MeV (dotted line in Fig.2.8). The GDR width from the decay of excited fission fragments was extracted for an average nuclear mass ($\sim$117) and compared with the prediction for the increase of GDR width with temperature in the framework of thermal shape fluctuation model in the low temperature region. It was found that the model overestimates the variation of GDR width at low temperature. The details can be found in Ref[Dee10b].

# Chapter 3

# Theoretical models

The theoretical formalism for shape transition in hot rotating nucleus and the statistical model for the interpretation of the high-energy $\gamma$-ray spectrum are discussed in this chapter.

## 3.1 Introduction

The equilibrium shape of a hot rotating nucleus can be obtained in a mean-field theory by minimizing its free energy $\mathrm{F}(\mathrm{T}, \omega; \rho)$ in the rotating frame at a given temperature T and angular velocity $\omega$ (of the rotating frame). Here $\rho$ represents a set of suitable variational parameters with respect to which F is minimized [Alh92]. In the case of nuclear shape transition, the quadrupole deformation parameters $\alpha_{2\mu}(\mu = -2, ., 2)$ are believed to play the dominant role. The parameters $\alpha_{2\mu}$ describe ellipsoidal shapes for the nuclear mean field. One can transform $\alpha_{2\mu}$ from the laboratory frame into $\mathrm{a}_{2\mu}$ in the intrinsic principal frame (see eq. 1.6), which is defined as $a_{2-1} = a_{21} = 0$, $a_{22} = a_{2-2}$ and $a_{20}$ real. The quantities $a_{20}$ and $a_{22}$ are then parameterized by the deformation parameters [Hil53] $\beta, \gamma$ as

$$a_{20} = \beta \cos(\gamma) \tag{3.1}$$

$$a_{22} = \frac{1}{\sqrt{2}} \beta \sin(\gamma) \tag{3.2}$$

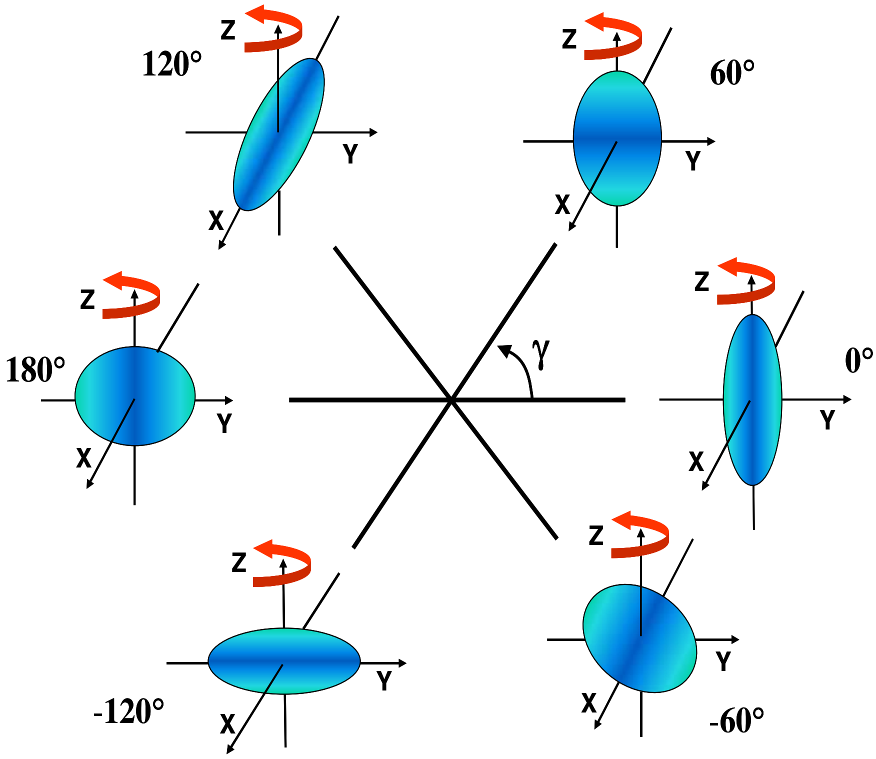


Figure 3.1: *Nuclear shapes in the $(\beta, \gamma)$ plane. The figure shows the orientation of the shape relative to the rotation axis (the z-axis in this case).*

These parameters $\beta, \gamma$ determine the intrinsic shape of the nucleus to be an ellipsoid with semi-axis lengths (k=1, 2, 3 for the three principal axes)

$$R_k = R_0 exp\left[\sqrt{\frac{5}{4\pi}}\beta cos\left(\gamma - \frac{2\pi k}{3}\right)\right] \tag{3.3}$$

Using the above conventions, when $\omega$ is parallel to z-direction, $\gamma = 0°$ and $\gamma = 180°$ describe a prolate and oblate shapes, respectively, rotating around their symmetry axis (non-collective motion), while $\gamma = \pm 120°$ and $\gamma = \pm 60°$ are these shapes, respectively, rotating around an axis perpendicular to the symmetry axis [Alh87]. When the angular rotation $\omega$ is not along z, the component of $\omega$ in the intrinsic principal frame is given as

$$\omega_x = -\omega \cos\phi \sin\theta \qquad \omega_y = \omega \sin\phi \sin\theta \qquad \omega_z = \omega \cos\theta \tag{3.4}$$

The free energy F(T,$\omega$; $\beta, \gamma, \Omega$) is independent of $\psi$ (which is the rotation angle around z). Configurations in which the nucleus rotates around a principal axis (say z) can all be described by taking -180° $\leq \gamma \leq$180°. These shapes are shown in Fig.3.1. The deformations are symmetric under the $\gamma \rightarrow -\gamma$ transformation, which corresponds to interchanging the x and y principal axes. Due to this symmetry the equilibrium shapes with $\gamma \neq 0°, \pm 180°$ always appear in symmetric pairs. The rotation along z differs from the common convention of $\omega$ as parallel to x, and it leads to a considerable simplification in many of the subsequent expressions and calculations [Alh92]. The change of convention does not affect the physical results and a shape $(\beta, \gamma)$ in the present thesis is $\beta$, $(\gamma + 120)$ in the standard one (i.e. $\omega$ parallel to x-direction).

## 3.2 The free energy

In calculations which are intended to determine the equilibrium shape of a highly excited and rotating nucleus one should in principle begin with the excitation energy E* and the angular momentum J as input parameters and maximize the entropy of the nucleus for the fixed values of these parameters. It is, however, much more convenient to work instead with fixed temperature T and angular velocity $\omega$ and minimize an appropriately chosen free energy [Alh87]. The free energy of a hot rotating nucleus is given by

$$F(\beta, \gamma, \omega, T) = E_{DLD} + (E - E_{av})_{shell} - TS - \frac{1}{2}(\vec{\omega} \cdot I \cdot \vec{\omega})\omega^2 \tag{3.5}$$

where,

$$\begin{aligned}
E &= \sum_i f_i \cdot e_i \\
f_i &= [1 + exp\{(e_i - \mu)/T\}]^{-1} \\
S &= -\sum_i f_i \cdot \ln(f_i) - \sum_i (1 - f_i) \cdot \ln(1 - f_i) \\
\vec{\omega} \cdot I \cdot \vec{\omega} &= I_{xx} \sin^2\theta \cos^2\phi + I_{yy} \sin^2\theta \sin^2\phi + I_{zz} \cos^2\theta
\end{aligned} \tag{3.6}$$

$e_i$ are the single particle energies and $E_{av}$ is the Strutinsky averaged energy. While S represents the entropy of the system, $f_i$ are the Fermi occupation numbers with $\mu$ as the chemical potential. $E_{DLD}$ is the deformed liquid drop energy and $(\vec{\omega} \cdot I \cdot \vec{\omega})$ is the moment of inertia about the rotation axis $\omega$. $I_{xx}$, $I_{yy}$, $I_{zz}$ are rigid body moments of inertia along the principal axes. The microscopic effects are neglected in our calculation as it is well known that at temperatures T $\geq$ 1.5 MeV shell effects melt and the nucleus behaves like a liquid drop [Coh74]. In physical application, spin is conserved rather than $\omega$ [Alh93]. Thus, for a hot rotating liquid drop, free energy surfaces at constant spin and neglecting the shell effects is given as [Alh93]

$$F(Z, N, \beta, \gamma, J, T) = E_{DLD}(Z, N, \beta, \gamma) - TS + \frac{J(J+1)\hbar^2}{2 \cdot (\vec{\omega} \cdot I \cdot \vec{\omega})} \tag{3.7}$$

### 3.2.1 Deformed liquid drop energy

The liquid drop energy can be calculated by summing the nuclear and Coulomb energies corresponding to a triaxially deformed shape in general defined by the deformation parameters $\beta$ and $\gamma$. However, as only the relative deformation energies are important, the liquid drop energy ($E_{LDM}$) is estimated by considering the surface and Coulomb energies. In order to calculate the surface energy, the Yukawa-plus-exponential model is considered which is discussed extensively in Ref[Kra79]. The generalized nuclear surface energy is given by

$$E_n = E_Y(a_{surf}, c_s) + \frac{2}{3} \frac{r_0}{a_{surf}} c_s A \tag{3.8}$$

where,

$$E_Y(a_{surf}, c_s) = -\frac{c_s}{8\pi^2 r_0^2 a_{surf}^3} \iint \frac{e^{-\sigma/a_{surf}}}{\sigma} d^3r d^3r' \tag{3.9}$$

with $\sigma$ = r - r$'$ and $a_{surf}$ being the range of the Yukawa folding function. The double integration is over the volume of the nuclear configuration, whose magnitude is kept fixed at $\frac{4}{3}\pi R_0^3$ as the nucleus deforms. The radius $R_0$ of the spherical shape is given by

$$R_0 = r_0 A^{1/3} \tag{3.10}$$

where $r_0$ is the nuclear radius constant. The dependence of the effective surface energy constant $c_s$ upon the relative neutron-proton excess I = (N - Z)/A is taken to be

$$c_s = a_s(1 - k_s I^2) \tag{3.11}$$

where $a_s$ is the surface energy constant and $k_s$ is the surface asymmetry constant.

The known deficiencies of the single-Yukawa model can be corrected by using a folding function that is the difference between two Yukawa function [Sch69, Sat76], which introduces another strength and another range. By varying the two ranges requiring that the interaction energy between two semi-infinite slabs of nuclear matter be a minimum for zero separation, one finds that heavy-ion interaction potentials are best reproduced if the two ranges are approximately equal. As the ranges become equal the strengths of the two Yukawa functions go to infinity but their difference remains finite [Kra79]. In the limit in which the two ranges become equal the resulting folding function is the difference between an exponential function and a Yukawa function, containing a single strength and a single range

$$E_n = -\frac{c_s}{8\pi^2 r_0^2 a_{surf}^3} \iint \left(\frac{\sigma}{a_{surf}} - 2\right) \frac{e^{-\sigma/a_{surf}}}{\sigma} d^3r d^3r' \tag{3.12}$$

For a single spherical nucleus, it is shown in Ref[Kra79] that eq.(3.12) gives

$$\begin{aligned} E_n^0 = B_s = &\left\{ 1 - 3\left(\frac{a_{surf}}{R_0}\right)^2 + \left(\frac{R_0}{a_{surf}} + 1\right) \right. \\ &\left. \cdot \left[ 2 + 3\left(\frac{a_{surf}}{R_0}\right) + 3\left(\frac{a_{surf}}{R_0}\right)^3 \right] e^{-2R_0/a_{surf}} \right\} E_s \end{aligned} \tag{3.13}$$

where $E_s = c_s A^{2/3}$ is the surface energy of a spherical nucleus. The leading term in eq.(3.13) is the surface energy, which is proportional to $A^{2/3}$. The mean curvature energy, which should be represented by a term proportional to $A^{1/3}$, is identically zero. The finite range of the nuclear force and the diffused nuclear surface give rise to the $A^{\circ}$ term and to the exponentially smaller terms [Mol81].

The Coulomb energy for a diffused nuclear density is given as

$$B_c = \frac{1}{2}\iint d^3r_1 d^3r_2 \frac{1}{|\bar{r}_1 - \bar{r}_2|}\rho(\bar{r}_1)\rho(\bar{r}_2) \tag{3.14}$$

where,

$$\rho(\bar{r}_1) = \rho_0 \int_v d^3r_2 G(|\bar{r}_1 - \bar{r}_2|) \tag{3.15}$$

is the diffused density of general form and the integration is over a given sharp-surface whose volume is $V$ such that $\rho_0 V = Ze$ for charge density [Dav76]. The folding function $G$ depends only on the magnitude of the vector $\overline{r_{12}} = \bar{r}_1 - \bar{r}_2$ and is normalized so that

$$\int d^3r_{12} G(r_{12}) = 1 \tag{3.16}$$

where the integration is over all space. Considering a folding function of Yukawa shape

$$G(|\bar{r}_1 - \bar{r}_2|) = \frac{1}{4\pi a_{den}^3}\left[\frac{e^{-|\bar{r}_1-\bar{r}_2|/a_{den}}}{|\bar{r}_1 - \bar{r}_2|/a_{den}}\right] \tag{3.17}$$

and putting the Yukawa folding function in eq.(3.14) and applying Faltung theorem, it was shown in Ref[Dav76] that the Coulomb energy reduces to

$$B_c = B_c(shape) + \Delta B_c \tag{3.18}$$

where,

$$B_c(shape) = \frac{\rho_0^2}{2}\int_v\int_v d^3r_1 d^3r_2 \frac{1}{|\bar{r}_1 - \bar{r}_2|} \tag{3.19}$$

$$\Delta B_c = -\frac{\rho_0^2}{2}\int_v\int_v d^3r_1 d^3r_2 \frac{1}{|\bar{r}_1 - \bar{r}_2|} \cdot e^{-|\bar{r}_1-\bar{r}_2|/a_{den}} \cdot (1 + \frac{1}{2}\frac{\bar{r}_1 - \bar{r}_2}{a_{den}}) \tag{3.20}$$

$B_c$ (shape) is the sharp-surface Coulomb energy and $\Delta B_c$ is the diffuse surface correction. $a_{den}$ is the range of the Yukawa function. The above equations can be solved by converting the volume integrals into surface integrals by use of single and double divergence relations. The equations (3.19) & (3.20) have been solved explicitly for a spherical shape in Ref[Dav76] which gives the Coulomb energy as

$$B_c(shape) = \frac{3}{5}\frac{Z^2e^2}{R_0} \tag{3.21}$$

$$\begin{aligned}\Delta B_c = -\frac{3Z^2e^2a_{den}^2}{R_0^3}\Bigg\{1 - \frac{15}{8}\left(\frac{a_{den}}{R_0}\right) + \frac{21}{8}\left(\frac{a_{den}}{R_0}\right)^3 - \frac{3}{4}e^{-2R_0/a_{den}} \\ \cdot\left[1 + \frac{9}{2}\left(\frac{a_{den}}{R_0}\right) + 7\left(\frac{a_{den}}{R_0}\right)^2 + \frac{7}{2}\left(\frac{a_{den}}{R_0}\right)^3\right]\Bigg\}\end{aligned} \tag{3.22}$$

The shape dependence of the mass in the liquid drop energy comes in through the liquid drop functions $f$ and $g$. The function $f$ gives the dependence of the surface energy on shape and is equal to the dimensionless ratio of the surface area of the shape in question to the area of the original sphere. The function $g$ is the dimensionless ratio of the electrostatic energy of a distorted sharp distribution to that of the sphere. In the case of an ellipsoidal shape described with the deformation parameters $\beta$ and $\gamma$, the functions $f$ and $g$ are given as [Mye66]

$$f = 1 + \frac{c_{surf}}{5}\alpha^2 - \frac{4}{105}\alpha^3\cos 3\gamma \tag{3.23}$$

$$g = 1 - \frac{1}{5}\alpha^2 - \frac{4}{105}\alpha^3\cos 3\gamma \tag{3.24}$$

where $\alpha^2 = \frac{5}{4\pi}\beta^2$ and according to Ref[Kra79], $c_{surf}$ is given as

$$\begin{aligned}c_{surf} = 2 - 27\left(\frac{a_{surf}}{R_0}\right)^2 + \Bigg[4\left(\frac{R_0}{a_{surf}}\right)^3 + 14\left(\frac{R_0}{a_{surf}}\right)^2 \\ + 32\left(\frac{R_0}{a_{surf}}\right) + 52 + 54\left(\frac{a_{surf}}{R_0}\right) + 27\left(\frac{a_{surf}}{R_0}\right)^2\Bigg]e^{-2R_0/a_{surf}}\end{aligned} \tag{3.25}$$

The higher order terms have been neglected and only $2^{nd}$ order terms have been considered. Thus, the deformed liquid drop energy is given as

$$E_{DLD} = B_s \cdot f + B_c \cdot g \tag{3.26}$$

Recently, the nuclear liquid drop model has been revisited by an explicit introduction of the surface-curvature terms and is known as the LSD model [Pom03] (Lublin-Strasbourg Droplet model). The model has been successfully used to explain the Jacobi shape transition in $^{46}$Ti [Maj04]. It also gives a good description of the fission barriers and is stiffer against high-multipolar deformations. However, the Yukawa-folding model also gives reasonable estimates of the fission barriers and should be adequate in explaining the shape transition in nuclei as only quadrupole deformations are concerned.

### 3.2.2 Moment of inertia

The rigid body moment of inertia $I_{zz}$ is calculated for an ellipsoid. From the Hill-Wheeler parameterization [Hil53] we have

$$a = \frac{R_1}{R_0} = exp\left(\sqrt{\frac{5}{4\pi}} \cdot \beta \cdot \cos\left(\gamma - \frac{2\pi}{3}\right)\right) \tag{3.27}$$

$$b = \frac{R_2}{R_0} = exp\left(\sqrt{\frac{5}{4\pi}} \cdot \beta \cdot \cos\left(\gamma + \frac{2\pi}{3}\right)\right) \tag{3.28}$$

$$c = \frac{R_3}{R_0} = exp\left(\sqrt{\frac{5}{4\pi}} \cdot \beta \cdot \cos(\gamma)\right) \tag{3.29}$$

Here $a, b, c$ are the semi-axis lengths in the units of the spherical radius $R_0$ such that $abc = 1$.

The moment of inertia $I_{zz}$ is given by

$$I_{zz} = B_1 \cdot \frac{2}{5} \cdot m \cdot r_0^2 \cdot A^{5/3} \tag{3.30}$$

where,

$$B_1 = \frac{E_R}{E_R^0} = \frac{1}{2}\frac{R_1^2 + R_2^2}{R_0^2} = \frac{1}{2} \cdot (a^2 + b^2) \tag{3.31}$$

$E_R$ is the rotational energy of a deformed nucleus and $E_R^0$ is the corresponding quantity for a spherical nucleus [Alh92]. Finally, the other moment of inertia can be calculated using the following relations

$$\begin{aligned} I_{xx} &= I_{zz}\left(\gamma - \frac{2\pi}{3}\right) \\ I_{yy} &= I_{zz}\left(\gamma + \frac{2\pi}{3}\right) \end{aligned} \tag{3.32}$$

### 3.2.3 Entropy

The entropy (S) can be calculated from the single particle energies ($e_i$) using the triaxially deformed Nilsson model. It is given as S = - $\sum_i f_i \cdot \ln(f_i) - \sum_i (1 - f_i) \cdot \ln(1 - f_i)$, where $f_i = [1 + \exp\{(e_i - \mu)/T\}]^{-1}$ are the Fermi occupation numbers. The chemical potentials $\mu_N$ and $\mu_P$ are determined separately for neutrons and protons from the condition $\sum_i f_i =$ N and $\sum_j f_j =$ P, respectively. However, it is known that the dependence of level densities on deformation is weak [Alh92]. Moreover, as the calculations in this work will be performed for different J values at fixed temperature, the entropy term is approximated by $\widetilde{a}T^2$, where $\widetilde{a}$ is the level density parameter.

## 3.3 Free energy surface & shape transition

The free energy surfaces for $^{47}$V and $^{32}$S nuclei are calculated using eq.3.7. The values of the different constants used in the calculation were taken from the Refs[Dav76, Kra79, Mol81] and are listed below.

$$\begin{aligned} &a_s = 21.7\,MeV && k_s = 3.0 \\ &e^2 = 1.439\,MeV\,fm && r_0 = 1.235\,MeV \\ &a_{den} = 0.7\,fm && a_{surf} = 0.65\,fm \end{aligned}$$

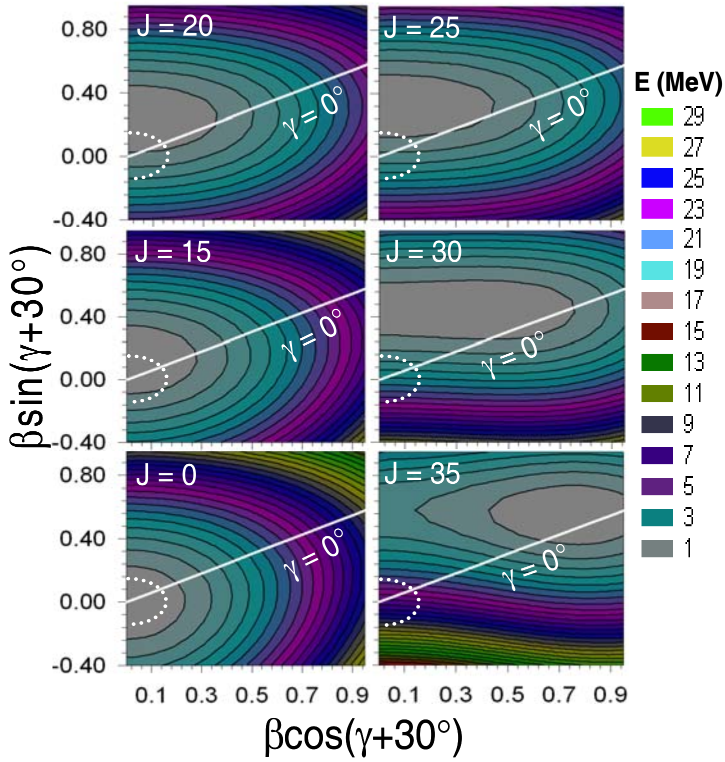


Figure 3.2: *Liquid drop free energy surfaces at different spins of $^{47}$V. The line represents the prolate shape ($\gamma = 0°$) while the dotted line corresponds to minimum of the free energy at $J = 0\hbar$.*

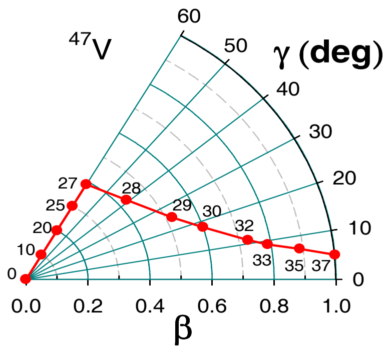


Figure 3.3: *The equilibrium shapes are plotted as a function of quadrupole deformation parameters $\beta$ and $\gamma$ for different spins for $^{47}$V nucleus. The discrete spin values are represented alongside the data points.*

### 3.3.1 Shape transition of $^{47}$V nucleus

The free energy distributions of $^{47}$V are plotted in the $(\beta, \gamma)$ - plane for six selected values of spin (Fig.3.2) and temperature T = 2.7 MeV. Here we have

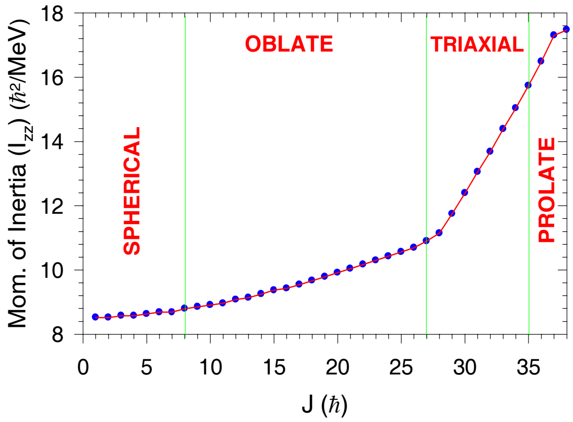


Figure 3.4: *The moment of inertia plotted as a function of angular momentum for the total shape change for* $^{47}V$ *nucleus.*

plotted $\gamma$ as ($\gamma$ - 120°) in order to represent the equilibrium deformation in conventional way i.e. $\gamma = 0°$ represents collective prolate and $\gamma = 60°$ represents non-collective oblate. It can be clearly seen that as the spin increases, the minima of the free energy surfaces move toward increasing oblate deformation (along the y-axis) and suddenly make a transition toward the prolate ($\gamma = 0°$) deformation (represented by the diagonal line in Fig.3.2 ) at high spins. The gradual evolution in shape and the transition point are evident in a polar $\beta$ vs $\gamma$ plot where the equilibrium deformations $\beta_{eq}$ and $\gamma_{eq}$ corresponding to minimum free energy is plotted for discrete spins (Fig.3.3). It is clear from the figure that for $^{47}$V, with the increase in angular velocity, the nucleus becomes more and more oblate deformed ($\gamma = 60°$). After a critical spin of $27\hbar$ it suddenly becomes triaxial ($60° < \gamma < 0°$) and approaches a prolate shape at still higher spins. This abrupt change of nuclear shape from an oblate ellipsoid non-collectively rotating around its symmetry axis, to an elongated prolate or triaxial shape, rotating collectively around the shortest axis is called Jacobi shape transition. The moment of inertia during the total shape evolution as function of angular momentum is shown in Fig.3.4.

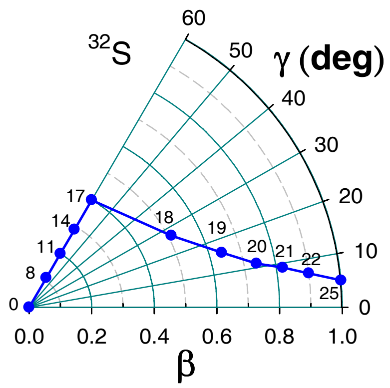


Figure 3.5: *The equilibrium shapes are plotted as a function of quadrupole deformation parameters $\beta$ and $\gamma$ for different spins for $^{32}S$ nucleus. The discrete spin values are represented alongside the data points.*

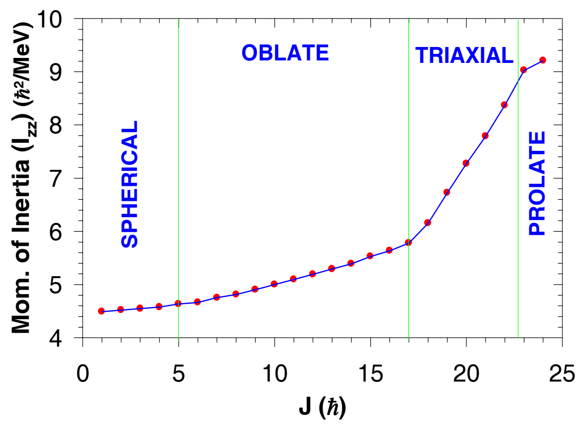


Figure 3.6: *The moment of inertia plotted as a function of angular momentum for the total shape evolution for $^{32}S$ nucleus.*

The Jacobi shape transition is also evident in the moment of inertia plot where $I_{zz}$ increases rapidly after $27\hbar$.

### 3.3.2 Shape transition of $^{32}$S nucleus

Similarly, the free energy surfaces for $^{32}$S nucleus are calculated for different spins at T = 2.8 MeV. The corresponding equilibrium deformation obtained from the minimization of the free energy surfaces are shown in the polar $\beta$ vs $\gamma$ plot for discrete spins (Fig.3.5). As can be seen, the equilibrium shape of the nucleus (in this liquid drop approximation) is spherical at J = 0. At low spins the nucleus is oblate and its deformation increases with spin. However above a certain critical spin (J = 17$\hbar$) the $^{32}$S nucleus becomes triaxial. The triaxial shape rapidly becomes nearly collective prolate and is characterized by large deformations. The moment of inertia as a function of angular momentum for $^{32}$S nucleus is shown in Fig.3.6. The shape evolution is also evident from Fig.3.6 where the different shapes of the nucleus are marked in the figure.

## 3.4 Giant dipole resonance cross sections

In general, for a non-rotating nucleus, the GDR strength functions along the 3 axes in general for an ellipsoidal shape can be obtained using the Hill-Wheeler parameterization $E_k = E_0 exp\left[-\sqrt{\frac{5}{4\pi}}\beta cos\left(\gamma - \frac{2\pi k}{3}\right)\right]$, with k = 1, 2, 3 denoting the three principal axes. $E_0$ refers to the centroid energy for a spherical nucleus with mass A. However these frequencies are modified in the case of a rotating nucleus. A rotating anisotropic harmonic oscillator potential and the isovector dipole-dipole interaction term describe the empirical energy of the giant dipole resonance [Nee82]. In the case of rotation about '1' axis, the cranking-model harmonic oscillator Hamiltonian is given as

$$\begin{aligned} H = \frac{1}{2}\sum_{\alpha=1}^{3}\left[\sum_{i=1}^{A}\left(\frac{p_\alpha^2}{m} + m\omega_\alpha^2 x_\alpha^2\right)_i + \frac{3m\omega_\alpha^2}{A}\left(\sum_{i=1}^{A}(\tau_3 x_\alpha)_i\right)^2\right] \\ - \Omega\sum_{i=1}^{A}(x_2 p_3 - x_3 p_2) \end{aligned} \tag{3.33}$$

where the oscillator frequencies $\omega_\alpha$ are inversely proportional to the extension of the nucleus along the axes $\alpha$ = 1, 2, 3 and $\Omega$ is the cranking frequency. In this approach, the two GDR components split (which are perpendicular to the rotation axis) due to Coriolis effect as the GDR vibrations in a nucleus couple with its rotation. The third component (along the rotation axis) remains intact. This gives altogether five components in general for the GDR strength function

[Nee82, Maj04, Dee10a]. These frequencies of the GDR in a rotating nucleus can be obtained by diagonalizing analytically the Hamiltonian in eq.(3.33). For rotation around z-axis, the final set of the GDR frequencies in the laboratory frame due to rotation is given by

$$
\begin{aligned}
\omega_1 &= \omega_z \\
\omega_2 &= \sqrt{\frac{\omega_y^2+\omega_x^2}{2} + \Omega^2 + \frac{1}{2}\sqrt{(\omega_y^2-\omega_x^2)^2 + 8\cdot\Omega^2\cdot(\omega_y^2+\omega_x^2)}} - \Omega \\
\omega_3 &= \sqrt{\frac{\omega_y^2+\omega_x^2}{2} + \Omega^2 + \frac{1}{2}\sqrt{(\omega_y^2-\omega_x^2)^2 + 8\cdot\Omega^2\cdot(\omega_y^2+\omega_x^2)}} + \Omega \\
\omega_4 &= \sqrt{\frac{\omega_y^2+\omega_x^2}{2} + \Omega^2 - \frac{1}{2}\sqrt{(\omega_y^2-\omega_x^2)^2 + 8\cdot\Omega^2\cdot(\omega_y^2+\omega_x^2)}} - \Omega \\
\omega_5 &= \sqrt{\frac{\omega_y^2+\omega_x^2}{2} + \Omega^2 - \frac{1}{2}\sqrt{(\omega_y^2-\omega_x^2)^2 + 8\cdot\Omega^2\cdot(\omega_y^2+\omega_x^2)}} + \Omega
\end{aligned}
\tag{3.34}
$$

It interesting to note that all five of these frequencies do not exist for all the shapes of the nuclei. They exist only for a collectively rotating triaxial nucleus as well as for a prolate nucleus ($\omega_x = \omega_y > \omega_z$) rotating about an axis perpendicular to its symmetry axis. However, for oblate nuclei ($\omega_x = \omega_y < \omega_z$) rotating about its symmetry axis, only two components, namely $\omega_1$ and $\omega_2 = \omega_5$, will exist. For spherical nucleus ($\omega_x = \omega_y = \omega_z$) one gets only one frequency, namely, $\omega_1 = \omega_2 = \omega_5$.

Therefore, the total GDR cross section can be written, in general, as

$$
\sigma = \sum_{i=1}^{n} \frac{\Gamma_i E_\gamma^2}{(E_\gamma^2 - E_i^2)^2 + \Gamma_i^2 E_\gamma^2} \tag{3.35}
$$

where $E_i$ and $\Gamma_i$ are the centroid energies and GDR widths, respectively, of the resonance. Here i represents the number of components of the GDR and is determined from the shape of the nucleus. The energy dependence of the GDR width is approximated by

$$
\Gamma_i = \Gamma_0 \left(\frac{E_i}{E_0}\right)^\delta \tag{3.36}
$$

where $\delta$ is taken as 1.9 [Aru04]. $\Gamma_0$ and $E_0$ are the ground state GDR width and centroid energy, respectively, for spherical nucleus of mass A.

## 3.5 Thermal shape fluctuation

The free energy minimization technique gives the most likely deformations for the nucleus under consideration at particular temperature and angular momentum. It is assumed that the nuclear deformation is frozen for each spin and temperature and no fluctuations are involved. However, at high temperatures the nuclear shape is not frozen. It can fluctuate around the equilibrium deformation which will influence the response of nuclei for dipole radiation. These shape fluctuations can be treated in a semi-classical way using methods of statistical mechanics. In a first approximation, it can be assumed that the changes in the shape parameters are slow compared to the GDR vibrations [Gal87, Pac88, Alh88]. Since the nucleus can have different shapes at temperature T and spin J, the macroscopic observables, like the absorption cross-section $\sigma_{abs}$, must be averaged over all possible shapes. A natural measure for the weight in the averaging procedure is given by the probability that the nucleus assumes a certain shape $(\beta, \gamma)$. The probability is related to the equi-potential surfaces of the free energy F by the Boltzman-distribution. The effective GDR strength distribution, measured in an experiment, is a sum of the strength distributions corresponding to vibrations built on each of the shapes that the nucleus undergoes, weighted with the probability that the nucleus has that shape,

$$\langle \sigma(E_\gamma; T, J) \rangle = \frac{\int D_\alpha \cdot exp(-F/T) \cdot \sigma(E_\gamma; T, J, \beta, \gamma)}{\int D_\alpha \cdot exp(-F/T)} \tag{3.37}$$

where $\sigma(E_\gamma; T, J)$ denotes the GDR strength function. The term $\mathrm{D}_\alpha$ is the volume element associated with the parameters $\beta, \gamma$.

$$D_\alpha = \beta^4 \cdot |\sin(3\gamma)| \; d\beta d\gamma \sin\theta d\theta d\phi \tag{3.38}$$

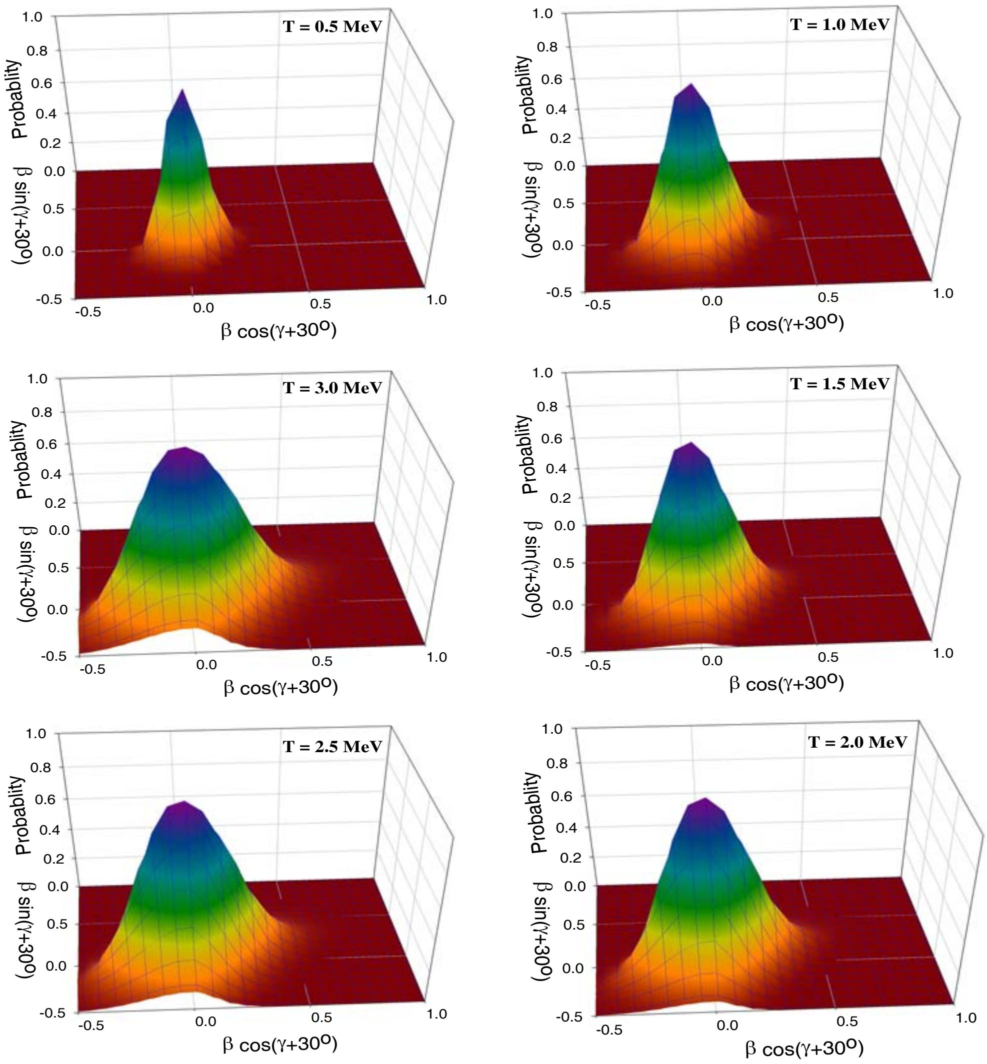


Figure 3.7: *The deformation probability distributions in the* $(\beta, \gamma)$ *plane for the* $^{47}$V *nucleus at different temperature (clockwise from the top left side). The distribution is normalized in such a way that the peak probability in each case is 1.*

The volume element is the Jacobian associated with the transformation of the five-quadrupole coordinates, including the orientation degrees of freedom [Boh75]. The Boltzmann probability (exp(-F/T)) as function of temperature for $^{47}$V nucleus is shown in Fig.3.7. Thus using the above formalism the GDR lineshape for any value of J & T can be calculated once the experimental angular momentum and temperature are known.

## 3.6 Statistical model

In order to interpret the high-energy $\gamma$-ray spectra, it is necessary to perform a statistical model calculation. The basic assumption of the statistical model for the decay of an excited nucleus is that all the relevant nuclear degrees of freedom are equilibrated before the decay can take place. When a compound nucleus (CN) is formed by fusion of two nuclei, it does not remember its initial formation conditions except for the conserved quantities like excitation energy ($E^*$), angular momentum (J), parity ($\pi$), isospin (T), etc. The compound nucleus can decay via the emission of particles (like neutron, proton, alpha) or gamma emission. In the statistical model of CN decay, the decay of such an equilibrated system into a particular channel will be governed by the available phase space in that exit channel. The decay rate through any channel is determined by the reciprocity theorem, i.e. the transition matrix elements associated with the formation of the compound nucleus a + A $\rightarrow$ C, are the same with those associated in the inverse decay process C $\rightarrow$ a + A. Consequently, the decay rates may be determined from the cross section of the inverse excitation process. The total decay rate, which determines the lifetime of the CN, is just the sum of all the partial decay rates for each of the exit channels. The cross section for the decay of the CN into a particular channel is provided by the branching probability multiplied by the fusion cross section for the formation of the compound nucleus [Pul77, Sri09].

The partial cross-sections for the formation of a compound nucleus of spin J and parity $\pi$ from a projectile and a target nucleus (spins $J_p$, $J_T$) at a centre of mass (cm) energy $E_{cm}$ is given by

$$\sigma(J,\pi) = \frac{\lambda^2}{4\pi} \frac{(2J+1)}{(2J_p+1)(2J_T+1)} \sum_{S=J_p-J_T}^{S=J_p+J_T} \sum_{L=J-S}^{L=J+S} T_L(E_{cm}) \qquad (3.39)$$

The transmission coefficient $T_L$ depends only on the energy ($E_{cm}$) and angular momentum ($L$). Here, $S = J_p + J_T$ is the channel spin and $\lambda$ is the wavelength. The summation over $L$ is restricted by the parity selection rule, $\pi_p \pi_t (-1)^L$. For strongly absorbed heavy ions, $T_L$ resembles the very simple form of Fermi distribution given as:

$$T_L = \frac{1}{1 + exp[(L - L_0)/d]} \tag{3.40}$$

Here $L_0$ is chosen in such a way that the total CN cross-section, $\sigma_{CN} = \sum_{J,\pi} \sigma(J, \pi)$ is reproduced. $d$ is termed as the diffusion parameter.

The computer code for statistical model calculations which had been used in the past, is CASCADE. This was originally written by Puhlhofer [Pul77] in 1977. After that, with time, different laboratories around the world have modified, revised and improved the original code according to their needs.

### 3.6.1 CASCADE

CASCADE is a computer routine to calculate the compound nuclear decay, where the excited compound nucleus is characterized by an initial excitation energy ($E^*$) and angular momentum distribution, realized in an ($E^*, J$) matrix. For each matrix element, the neutron, proton, $\alpha, \gamma$ and fission decay probabilities have been calculated, and the corresponding population is transferred to new ($E^*, J$) matrices, representing the daughter nuclei [Sri09]. This procedure is continued until the nuclei cools below the particle emission threshold energy, then finally subsequent calculation of the low energy yrast $\gamma$-ray emissions are performed. The rate $R_x d\epsilon_x$ for emitting a particle $x$ from an excited nucleus 1 (excitation energy $E_1$, spin $J_1$, parity $\pi_1$) to form a product nucleus 2 (at $E_2, J_2, \pi_2$) is

$$R_x d\epsilon_x = \frac{\rho_2(E_2, J_2, \pi_2)}{2\pi\hbar\rho_1(E_1, J_1, \pi_1)} \sum_{S=J_2-s_x}^{S=J_2+s_x} \sum_{L=J_1-S}^{L=J_1+S} T_L^x(\epsilon_x) d\epsilon_x \tag{3.41}$$

where $\epsilon_x$ is the kinetic energy of particle $x$ given as $\epsilon_x = E_1 - E_2 - B_x$. $B_x$ is the binding energy, $s_x$ is the spin of the particle $x, L$ is its orbital angular momentum and $S = J_2 + s_x$ is the channel spin. $\rho_1$ and $\rho_2$ are the level densities of the initial and final states of the nuclei. The transmission coefficients $T_x^L$ are calculated from the optical model potentials. In the calculation, the optical model potential parameters of Perey [Per63] and Huizenga & Igo [Hui62] have been used for the protons and the alpha particles. While for neutrons, the parameters of Wilmore and Hodgeson [Wil64] have been used.

The rate of $\gamma$-decay is also given by a similar formula

$$R_\gamma d\epsilon_\gamma = \frac{\rho_f(E_f, J_f)}{2\pi\hbar\rho_1(E_i, J_i)} \sum_L f_L(E_\gamma) E_\gamma^{(2L+1)} d\epsilon_\gamma \tag{3.42}$$

where $L$ denotes the multipolarity of the $\gamma$ ray. Modified CASCADE includes the emission of giant dipole resonance $\gamma$ rays built on excited states of nuclei. The absorption cross-section for GDR for spherical nuclei is well-reproduced by a lorentzian distribution. The GDR strength function is given by

$$\begin{aligned} f(E_\gamma) &= 2.09 \times 10^{-5} \cdot \frac{NZ}{A} \cdot S \cdot \frac{\Gamma_{GDR} E_\gamma}{(E_\gamma^2 - E_{GDR}^2) + \Gamma_{GDR}^2 E_\gamma^2} \\ &= 2.09 \times 10^{-5} \cdot \frac{NZ}{A} \cdot S \cdot f_{GDR}(E_\gamma) \end{aligned} \tag{3.43}$$

where $S$ is the fraction of the energy weighted dipole sum rule (EWSR), $E_{GDR}$ and $\Gamma_{GDR}$ are the centroid energy and width of the lorentzian distribution. For an axially deformed nucleus, the strength function is expressed as the superposition of two lorentzians since the GDR resonance will vibrate along the principal axes with frequencies inversely proportional to the lengths of these axes. In that case, $S_1$ and $S_2$ are the sum rule strengths of the two components and are expressed as $S_1 + S_2 = 1$ corresponding to the 100% sum rule strength. $S_2/S_1 = 2$ and $1/2$, respectively denote the GDR in a prolate and oblate deformed nuclei. The combined strength function can be expressed as

$$f_{GDR}(E_\gamma) = \frac{S_1 f_1(E_\gamma) + S_2 f_2(E_\gamma)}{S_1 + S_2} \tag{3.44}$$

$f_1$ and $f_2$ are the lorentzians due to vibration of nucleons along the two principal axes. $S_1$ and $S_2$ are corresponding strengths.

The level density $\rho$ at excitation energy $E^*$ and spin $J$ is given by

$$\rho(E^*, J) = \frac{2J+1}{12}\left(\frac{\hbar^2}{2I_0}\right)^{3/2}\sqrt{a}\ \frac{exp(2\sqrt{aU})}{U^2} \tag{3.45}$$

where

$$U = E^* - E_{rot} - \Delta_p \tag{3.46}$$

$$E_{rot} = \frac{\hbar^2}{2I}J(2J+1) \tag{3.47}$$

$$a = \tilde{a}\left[1 + \frac{\Delta_S}{U}\{1 - exp(-\gamma U)\}\right] \tag{3.48}$$

$\gamma$ being the shell correction damping factor and $U$ the internal thermal energy of the system. This form of energy dependence of nuclear level density (NLD) parameter $a$ incorporates the excitation energy dependence of the shell effect [Ign75]. Here, $\Delta_P$ is the pairing energy and the ground state shell correction $\Delta_S$ is determined by the magnitude of shell effects. The moment of inertia $I$ at a given $J$ is related to $I_0$ (rigid body moment of inertia) according to the rotating liquid drop model (RLDM) as $I = I_0(1 + \delta_1 J^2 + \delta_2 J^4)$. The parameter $\tilde{a}$ represents the asymptotic, liquid drop value of the level density parameter. The damping factor is estimated from the calculation of Schmidt [Sch82], viz, $\gamma^{-1} = 0.4A^{4/3}/\tilde{a}$.

# Chapter 4

# Giant dipole resonance $\gamma$-rays from hot $^{47}$V nucleus

## 4.1 Introduction

The giant dipole resonance (GDR), built on highly excited nuclear states, is the main experimental probe to study the shapes of hot rotating nuclei. Hot nuclei are formed in heavy ion fusion reactions where the relative kinetic energy of the colliding nuclei is converted into internal excitation energy and high angular momentum of the compound nuclei. These nuclei at high spin may undergo a Jacobi shape transition, an abrupt change of shape from an oblate ellipsoid rotating around the symmetry axis to an elongated prolate or triaxial shape rotating perpendicularly around the symmetry axis, similar to one, which occurs in rotating gravitating stars [Cha69]. In the search for exotic nuclear shapes, the light and medium mass nuclei are of special interest. This is because these nuclei are expected to undergo Jacobi shape transition at values of the angular momentum which are relatively low and below the fission limit. Signatures of such shape transitions in $^{45}$Sc [Kin93] and $^{46}$Ti [Maj04, Kmi07] have been seen from the study of GDR lineshapes built on excited states.

Recently, the deformation of the excited $^{47}$V nucleus has been grossly estimated from an inclusive $\alpha$-particle measurement [Apa06]. These studies, however, only indicate the overall deformation in an indirect way. Hence, it is worthwhile to complement the above study by measuring the deformation, in more direct manner, via the GDR $\gamma$-decay since it is also expected to undergo Jacobi shape transition similar to $^{46}$Ti [Maj04] at these conditions.

## 4.2 The multiplicity filter

In heavy-ion fusion reaction, the compound nucleus is formed at a well-defined excitation energy, but with a wide range of angular momenta. The hot compound nucleus loses most of the excitation energy via particle and gamma emissions above the yrast line. The remainder of the excitation energy and angular momentum are generally removed by the low energy discrete gamma emission [Har01]. A precise measurement of this $\gamma$-multiplicity is very important since the number of $\gamma$-rays emitted are directly related to the angular momenta populated in the system. The multiplicity of gamma rays is measured with an array of detectors placed close to the target having high gamma detection efficiency and granularity. The fold (number of multiplicity detectors fired) distribution is recorded on an event-by-event basis in coincidence with the high-energy gamma rays. Finally, the angular momentum distribution is extracted from this fold distribution in offline analysis.

At the Variable Energy Cyclotron Centre, Kolkata, India, a 50 - element gamma-multiplicity filter made of $BaF_2$ has been designed and developed for the measurement of angular momentum of the compound nucleus in an event by event mode [Dee10c].

### 4.2.1 Multiplicity detector fabrication

The preparation of $BaF_2$ detector from the bare crystal is a very involving as well as an interesting job. Standard procedures were followed for detector fabrication from bare barium fluoride crystals. First, the bare crystals were cleaned thoroughly using pure dehydrated ethyl alcohol. Each crystal was wrapped with 6 layers of 15 $\mu$m white teflon tape since the scintillation light components are in the ultra violet (UV) region and teflon ($C_2F_2$) is a very good reflector of UV light. Next, aluminium foil of 10 $\mu$m (3-4 layers) was used to enhance the light collection and to block the surrounding light from entering into the crystal. Fast, UV sensitive photomultiplier tubes (29mm dia, Phillips XP2978) were coupled with the crystals using highly viscous UV transmitting optical grease (Basylone, 300000 cstokes). This coupling need to be done very carefully so that no air bubble remains in the grease over the crystal surface, because air bubbles provide unwanted reflecting surfaces amounting to a loss of scintillation light and degrades the timing property. Specially designed aluminium collars were also used around the coupling area to provide additional support. A squared shape teflon reflector (3.5cm $\times$ 3.5cm) with a 3.0 cm hole at the centre was placed at the PMT end of the crystal to reflect back UV light which would otherwise escape from the PMT. A PMT voltage divider base was then attached to the PMT for applying the high voltage. After that, the whole assembly was covered with black electrical tape for light-tightness, and finally with heat-shrinkable PVC tube for providing mechanical stability to the detector. The total fabrication process is shown in Fig.4.1 and Fig.4.2. The multiplicity filter assembly arranged in two blocks of 5$\times$5 arrays is shown in Fig.4.3.

### 4.2.2 Energy and time resolution

The individual detector elements were tested with lab standard gamma ray sources. The energy spectra measured in individual detector is shown in Fig.4.4. The observed energy resolution is 7.2% at 1.17 MeV of $^{60}$Co source. The time resolution between two $BaF_2$ detectors was measured with the $^{60}$Co $\gamma$-ray source. The source was placed in between two identical detectors, which were kept 180°

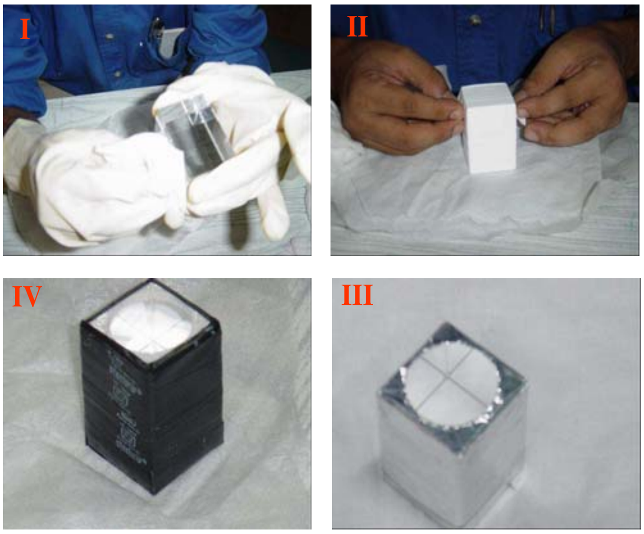


Figure 4.1: *The step by step process for detector fabrication from a bare crystal. Clockwise from the top left side. I. Cleaning of the bare $BaF_2$ crystal with pure dehydrated ethyl alcohol. II. The wrapping of the crystal with white teflon tape. III. The wrapped aluminium foil over the teflon wrapped crystal. IV. The black electric tape wrapped over the aluminium tape for light tightness.*


Figure 4.2: *The step by step process for detector fabrication from a bare crystal. Clockwise from the top left side. I. Highly viscous optical grease over the crystal surface before connecting to PMT. II. Coupling of the PMT with the crystal. III. The specially designed aluminium collar being put around the coupling area to provide additional support. IV. The total assembly covered with black electric tape and finally with heat shrinkable tube to provide mechanical stability to the detector.*

Figure 4.3: *The full multiplicity filter arranged in two blocks of 5×5 arrays.*

apart. The energies and their relative times were measured simultaneously in an event by event mode. The energy gated (1.0-1.4 MeV) time spectrum is shown in Fig.4.5. The value obtained for the time resolution is 450 ps [Dee10c].

### 4.2.3 Crosstalk probability

The crosstalk probability was measured with $^{22}$Na, $^{137}$Cs and $^{60}$Co sources at different thresholds. Twenty-five detectors were arranged in a $5 \times 5$ matrix. A start signal was generated from an external large $BaF_2$ detector (3.5×3.5×35 cm$^3$). The detectors of the multiplicity filter were gain matched and equal thresholds were applied to all. The events were collected only if 1.33 MeV gamma ray from $^{60}$Co source (or 1.274 MeV in case of $^{22}$Na) gave a photo-peak in the large $BaF_2$ detector, ensuring that exactly one gamma ray (1.17 MeV or 511 keV for $^{60}$Co or $^{22}$Na sources, respectively) was incident on the multiplicity filter. In the case of $^{137}$Cs, since only one gamma (662 keV) is emitted from the source no coincidence could be made. The background events were collected in an identical condition without the source and subtracted from the data. The

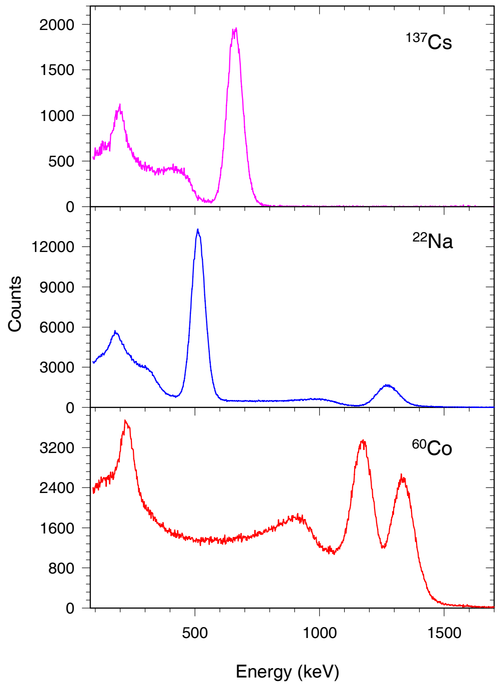


Figure 4.4: *Energy spectra from a single multiplicity detector for different laboratory standard gamma ray sources.*

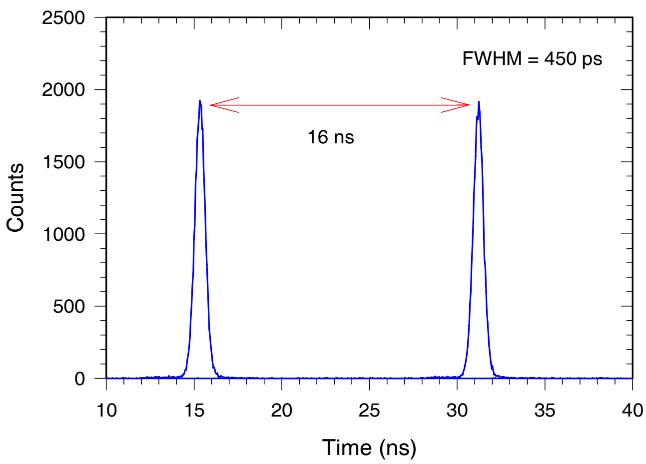


Figure 4.5: *Time resolution of an individual detector using $^{60}Co$ $\gamma$-source.*

data for different hit patterns were collected by counting in a scalar module. The crosstalk probabilities for the three energies at different thresholds of the multiplicity filter are shown in Fig.4.6 (solid points). The crosstalk probabili-

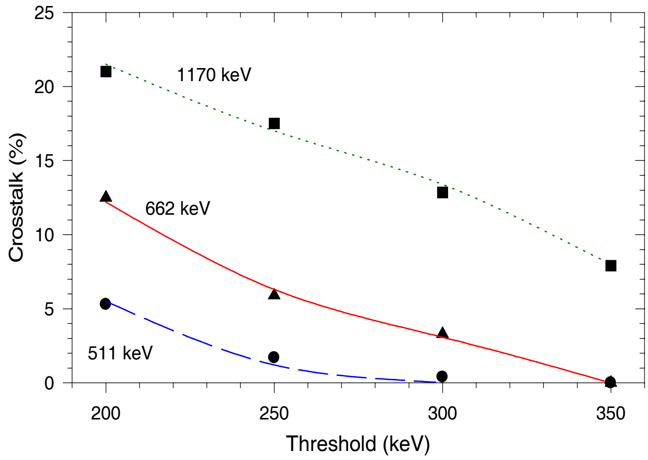


Figure 4.6: *The crosstalk probabilities for three energies ($^{22}$Na, $^{137}$Cs and $^{60}$Co) at different thresholds of the multiplicity filter. The symbols represent the experimental points while the lines correspond to GEANT simulation.*

ties were also calculated using Monte Carlo GEANT3 simulations and are also shown in Fig.4.6 (lines). The crosstalk probability is more for higher energy and decreases with increasing the threshold of the multiplicity detectors [Dee10c].

## 4.3 Experimental details

The LAMBDA spectrometer [Muk07] and the 50-element multiplicity filter [Dee10c] were employed for measuring the high-energy gamma rays from the decay of GDR and low energy multiplicity gamma rays, respectively, for $^{47}$V nucleus in an in-beam experiment.

The experiment was performed at the Variable Energy Cyclotron Centre, Kolkata using the 224 cm K-130 AVF room temperature cyclotron. A stable beam of $^{20}$Ne accelerated by the cyclotron was bombarded on a 1 mg/cm$^2$ thick target of $^{27}$Al. The initial excitation energy of $^{47}$V compound system was $E_x$ = 108 MeV corresponding to a projectile energy $E_{proj}$ = 160 MeV. The corresponding critical angular momenta was $L_{cr} = 38\hbar$. This value extends well beyond the critical angular momentum values of $28\hbar$ at which the Jacobi transitions are predicted to occur for this nucleus. The $^{47}$V compound nucleus was formed in an identical condition as in the previous charged particle measurement reported earlier [Cha05, Apa06].

The high-energy photons were detected using a part of the LAMBDA spectrometer [Muk07] arranged in a 7×7 matrix. It was centered at 55° to the beam direction and at a distance of 50 cm from the target, subtending a solid angle of 0.227 sr (1.8 % of $4\pi$). Lead sheets of 5 mm thickness were placed in front and sides of the array, to cut down the intensity of the low energy gamma rays. The beam was stopped in a downstream dump placed at 3m from the target. The neutrons and the gamma rays from the dump were shielded using borated paraffin and lead, respectively. The low energy $\gamma$-ray multiplicity was measured, in coincidence with the high-energy $\gamma$-rays, using the in-house developed 50-element multiplicity filter. It was split into two blocks of 25 detectors each, which were placed on the top and the bottom of the scattering chamber in castle type geometry. The distances of the detectors from the target were adjusted to equalize their efficiencies (solid angle). The overall efficiency of the multiplicity setup was ~30% as calculated using GEANT3 simulation. The detectors of the multiplicity filter were gain matched and equal thresholds were applied to all. The experimental setup is shown in Fig.4.7.

### 4.3.1 Trigger generation

The scheme of the complete electronic set-up is shown in Fig.4.8. The signals from the photo-multiplier tube (PMT) outputs of the spectrometer were first pre-amplified using a fixed (×10) gain fast amplifiers (CAEN N412). The amplified signals were split into two parts for the subsequent linear and logic paths. Each of the signals in the linear path was given a 100 ns delay and was split into two parts, with an amplitude ratio of 1:10 before sending them to

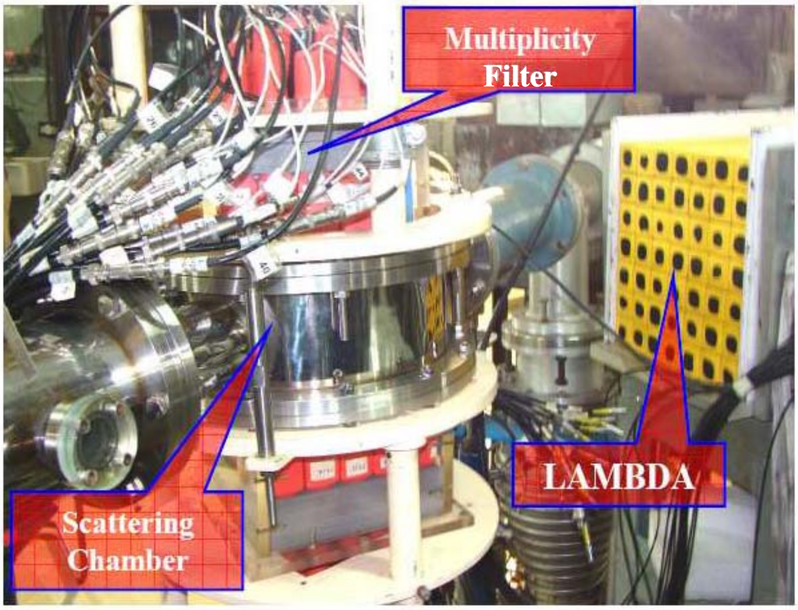


Figure 4.7: *The experimental setup of the LAMBDA spectrometer along with the multiplicity filter.*

a pair of QDCs for long and short integration. The signals in the logic path were sent to CAMAC leading-edge-discriminators (LED) (CAEN C894) and constant-fraction-discriminators (CFD) (CAEN C671). A level-1 trigger (A) was generated when the signal in any of the detector elements of the LAMBDA spectrometer crossed a high threshold ($>$ 4 MeV). Another trigger (B) was generated from the multiplicity filter array when any detector of the top block and any detector from the bottom block fired in coincidence. The coincidence between top and bottom multiplicity biased the selection of the angular momentum measurement towards the high spin region. A coincidence of these two triggers 'A' & 'B' generated the master trigger ensuring the selection of the high-energy photon events from the compound nucleus and the rejection of background. The signals from the multiplicity filters were fed to constant-fraction-discriminators (CFD) (CAEN C808) which gives a current sum output (50mV per hit) corresponding to the number of detectors fired. The current

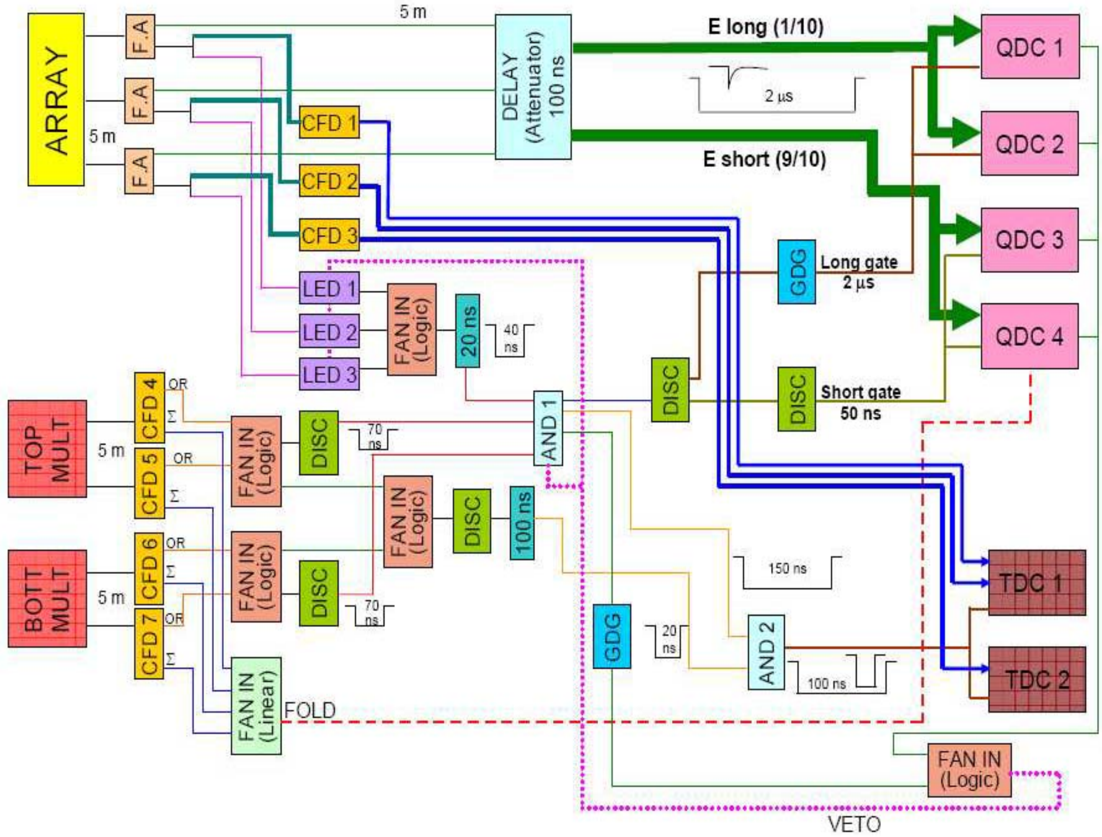


Figure 4.8: *The electronic scheme of the experimental setup.*

sum outputs from the four CFDs were summed in a Linear-Fan-in module. The summed output was fed into a QDC (V792) gated by the master trigger to generate, on event-by-event basis, the experimental fold (F) distribution with condition (F$\geq$2). The master trigger was also used for generating the integration gates (2$\mu$s, 50ns) and the common-start trigger of the TDCs. Each TDC was stopped by the individual delayed outputs from the CFDs (with a uniformly low threshold of 300 keV) for the generation of the individual time spectrum for each element of LAMBDA. For each of the 49 elements of LAMBDA, the long and short gate integrated energies and time were recorded for each triggered event.

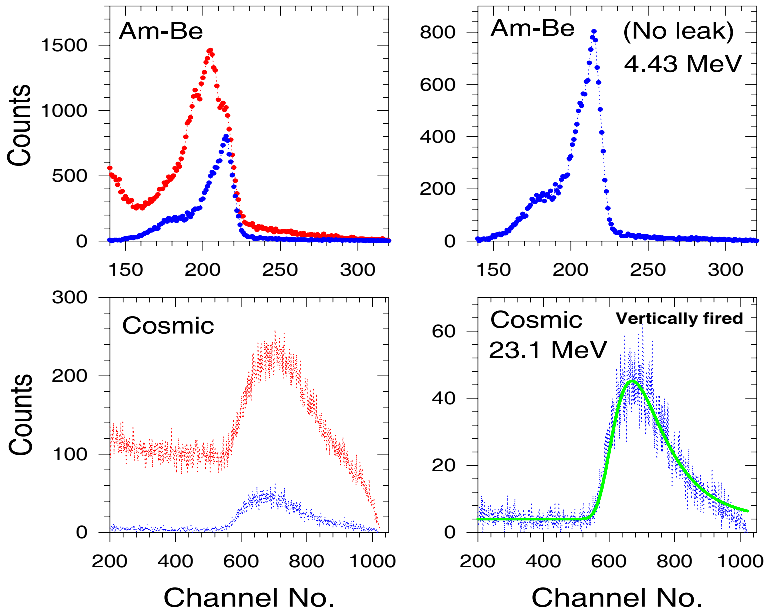


Figure 4.9: *Top panel: The Am-Be spectrum in one of the large $BaF_2$ detectors during calibration. The left panel shows the comparison between raw spectrum (red circles) and no-leak spectrum (blue circles) while the no-leak spectrum is shown independently in the right panel. Bottom panel: Cosmic muon spectrum in the same detector during calibration. In the left panel, the raw spectrum (red line) is shown along with the vertically fired condition (blue line). The spectrum for vertically fired condition is shown in the right panel. The spectrum is fitted with Landau function to extract the most probable energy (continuous line).*

### 4.3.2 Calibration of the detectors

All the 49 detectors of the LAMBDA spectrometer were calibrated using lab standard $\gamma$-ray sources and with minimum ionizing cosmic muons. The low energy calibration points were obtained using $^{22}$Na (0.511 and 1.274 MeV) and $^{241}$Am-$^{9}$Be (4.43 MeV). Due to the small cross-sectional area of individual detector element, 4.43 MeV $\gamma$-ray from Am-Be source does not deposit its full energy always and is dominated by the escape peaks (Fig.4.9). During offline analysis, the photo-peak (full energy peak) is observed cleanly by generating the spectrum under the condition that only a single detector has been fired without any leakage to the neighboring detectors in the event (no leak condition). The spectrum of 4.43 MeV $\gamma$-ray is shown in Fig.4.9 (left top panel) along with the

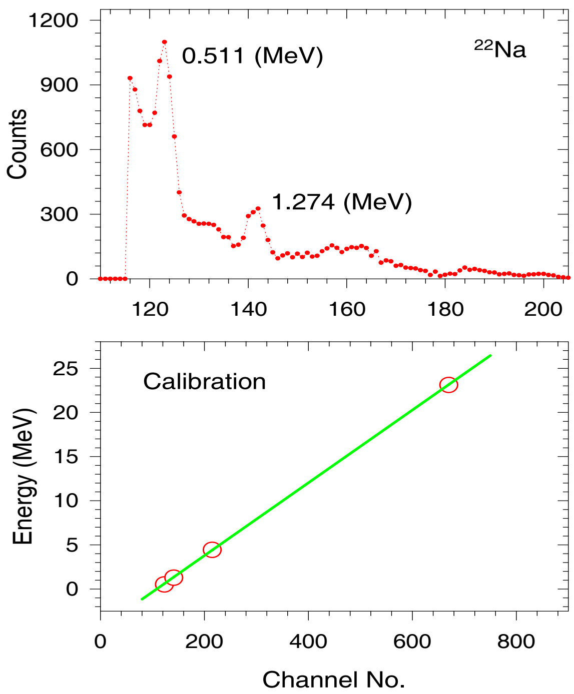


Figure 4.10: *The $^{22}$Na spectrum during calibration is shown in the top panel while the calibration curve is shown in the bottom panel.*

no-leak spectrum. The no-leak spectrum is shown individually in Fig.4.9 (right top panel). The $^{22}$Na spectrum obtained during calibration is shown in Fig.4.10 (top panel).

Minimum ionizing cosmic muons deposit 6.6 MeV/cm in $BaF_2$ material. Hence, while travelling the width of our detector (3.5 cm) vertically, they deposit 23.1 MeV of energy in the detector volume. The typical cosmic muon spectrum in the individual detector element, without any condition, during the calibration is shown in Fig.4.9. In offline analysis, the spectrum of cosmic muon is generated when all the seven detectors in a vertical column fire in a single event. This ensures that the muons travel the width of the crystal in a minimum path. The offline generated spectrum is compared with the no condition cosmic spectrum in Fig.4.9 (bottom left panel). The vertically fired spectrum is shown independently in right panel. The most probable energy was obtained by fitting the spectral shape with a Landau function (continuous line in Fig.4.9) and used for calibration.

The energy response of the detectors were found to be linear upto 4.43 MeV. The calibration curve is shown in Fig.4.10 (bottom panel). This calibration was extrapolated to 23.1 MeV (energy lost by cosmic muons) and found to match nicely ensuring a linear energy response of the detectors up to at least 23 MeV.

## 4.4 Extraction of angular momentum

During the experiment, the multiplicity fold distributions from the low energy yrast $\gamma$-rays were measured in an event-by-event mode using the multiplicity filter array. To remove the contributions of any non-fusion events, the final experimental fold spectrum was generated, offline, by gating with high energy gamma rays (>10 MeV) (filled circle in Fig.4.11) [Sri08] . The approach based on Monte Carlo GEANT3 simulation [Dee10c] was adopted to convert the experimental fold distribution to the angular momentum space. In this simulation, the realistic experimental conditions (including the detector thresholds and trigger conditions) were taken into account. Two blocks of 25 detectors arranged in 5×5 arrays were kept on the top and bottom of the scattering chamber, similar to the experiment. The incident multiplicity distribution was considered triangular and is given as, for a multiplicity M,

$$P(M) = \frac{2M+1}{1+exp((M-M_{max})/\delta M)} \tag{4.1}$$

where, $M_{max}$ is the maximum of this distribution and $\delta m$ is the diffuseness. The different input multiplicities of the low energy $\gamma$-rays were obtained by creating a random number according to the multiplicity distribution $P(M)$. Low energy gamma rays, for each randomly generated multiplicity, were thrown

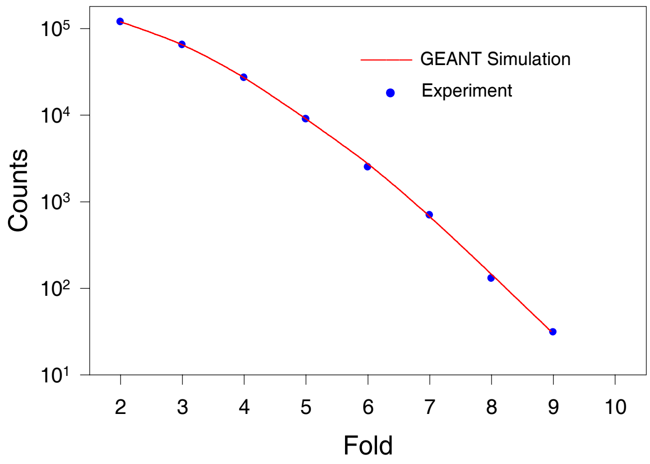


Figure 4.11: *The experimental fold spectrum (symbols) fitted with GEANT simulation (solid line).*

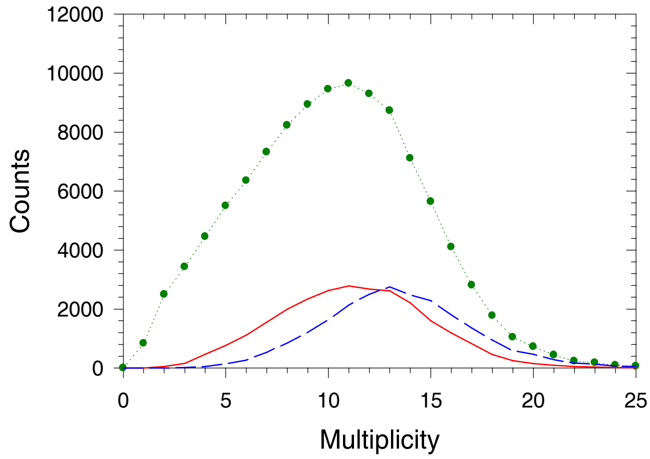


Figure 4.12: *The incident multiplicity distribution used in GEANT simulation (symbols along with dotted line). The multiplicity distributions obtained for different folds are also shown in the figure. The solid line represents fold 2 while the dashed line represents fold ≥3.*

isotropically from the target centre and the corresponding fold was recorded for that event. Two hundred thousand events were thrown to generate the simulated fold distribution. The energy distribution of the incident multiplicity was considered a gaussian with peak at 0.5 MeV and width 0.65 MeV.

The angular momentum distribution of the reaction $^{20}$Ne + $^{27}$Al was obtained from statistical model code CASCADE. The conversion of the angular momentum distribution to multiplicity distribution is achieved using the relation $J = 2 \cdot M + C$, where $C$ is the free parameter which takes into account the angular momentum loss due to particle evaporation and emission of statistical $\gamma$-rays. The parameters $M_{max}$ and $\delta m$ of the multiplicity distribution was obtained from the J-distribution by varying the free parameter $C$ until the best fit between measured F-distribution and simulated F-distribution was achieved. The value of $C$ was obtained as 6 and the parameters of the M-distribution were extracted as $M_{max} = 14.0$ and $\delta m = 2$ for best fit. The simulated fold distribution generated using the triangular distribution is shown by solid line in Fig.4.11. Next, the constrained multiplicity distributions for different folds were generated. The incident multiplicity distribution (dotted line along with symbol) and the multiplicity distributions for different fold windows are shown in Fig.4.12. The continuous line and the dashed line indicate the multiplicity distributions gating on the events with folds 2 and folds ≥3 respectively. The average angular momentum values for different folds are summarized in Table 4.1.

Table 4.1: Average angular momentum values corresponding to different folds.

| Reaction | Fold | <J> $\hbar$ |
|---|---|---|
| $^{20}$Ne + $^{27}$Al @ 160 MeV | 2 | 28.0 ± 7.0 |
| | ≥3 | 31.3 ± 8.0 |

## 4.5 Experimental data analysis

The high-energy gamma spectra were generated from the offline analysis of the data recorded in the event-by-event mode after putting proper cuts on the time of fight (TOF) and pulse shape discrimination (PSD)(discussed in Chapter 2).

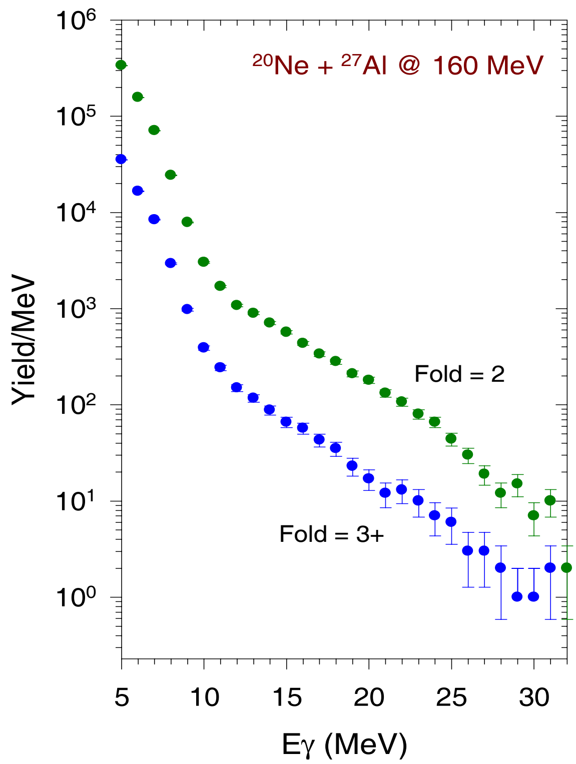


Figure 4.13: *The experimental high-energy $\gamma$-ray spectra.*

After application of different conditions, in a valid event, the energies deposited in the detectors were summed using the nearest neighbor event reconstruction technique [Muk07]( also discussed in Chapter 2). Finally the energies were Doppler corrected assuming the source velocity same as the compound nucleus velocity. The high-energy $\gamma$-ray spectra were generated for fold 2 and fold $\geq 3$ in the multiplicity filter which correspond to average angular momentum values of $28\hbar$ and $31\hbar$, respectively. The high-energy $\gamma$-ray spectra is shown in Fig.4.13.

The measured individual high-energy $\gamma$-ray spectrum corresponding to fold 2 and fold $\geq$ 3 were fitted using the statistical model decay code CASCADE along with a bremsstrahlung component to extract the GDR strength function. The estimated spin distributions, using GEANT3 simulation for different folds, were used as inputs in the statistical model calculation. The non statistical contribution arising due to bremsstrahlung was parameterized using the relation $\sigma_{brem} = A \cdot exp(-E_\gamma/E_0)$. The slope parameter was taken according to the prediction $E_0 = 1.1 \cdot [(E_{lab} - V_c)/A_p]^{0.72}$, where $E_{lab}, V_c$ and $A_p$ are the beam energy, Coulomb barrier and projectile mass, respectively [Nif90]. The CASCADE calculations have been performed with the same parameters as used in the charged particle analysis to explain the inclusive $\alpha$-spectrum in $^{20}$Ne + $^{27}$Al reaction at 160 MeV [Apa06]. The $r_0, \delta_1$ and $\delta_2$ parameters were taken as 1.30 fm, $4.5 \times 10^{-4}$ and $2.0 \times 10^{-8}$, respectively. The level density prescription of Ignatyuk et al. [Ign75] was used with the asymptotic level density parameter $\tilde{a}$=A/8.0 MeV$^{-1}$. Finally, the theoretical spectrum was folded with the detector response function, generated using the Monte Carlo GEANT3 simulation [Muk07], to compare with the experimental spectrum. It needs to mention that a conventional two-component Lorentzian strength function, which can be related to a prolate or an oblate shape of the excited and rotating nuclei, could not fit the data. The reason for this could be the fact that the $^{47}$V nucleus is experimentally populated at high spin of 28$\hbar$ and 31$\hbar$. According to the rotating liquid drop model, the $^{47}$V nucleus is predicted to undergo Jacobi shape transition at these angular momentum values consisting of five GDR components altogether (discussed in Chapter 3). Hence, calculations were performed using the theoretical formalism developed in Chapter 3 to extract all the five GDR components at the experimental $J$. It is interesting to note that the statistical model calculation, considering these parameters, represent the experimental data remarkably well for both the angular momentum windows. The CASCADE calculation along with the bremsstrahlung component folded with the detector response function is shown in Fig.4.14 (continuous line) together with the experimental data (filled circles). The linearized GDR spectrum was generated by the quantity $F_L(E_\gamma) \cdot Y_{exp}(E_\gamma)/Y_{cal}(E_\gamma)$. In this expression $Y_{exp}(E_\gamma)$ and $Y_{cal}(E_\gamma)$ are the

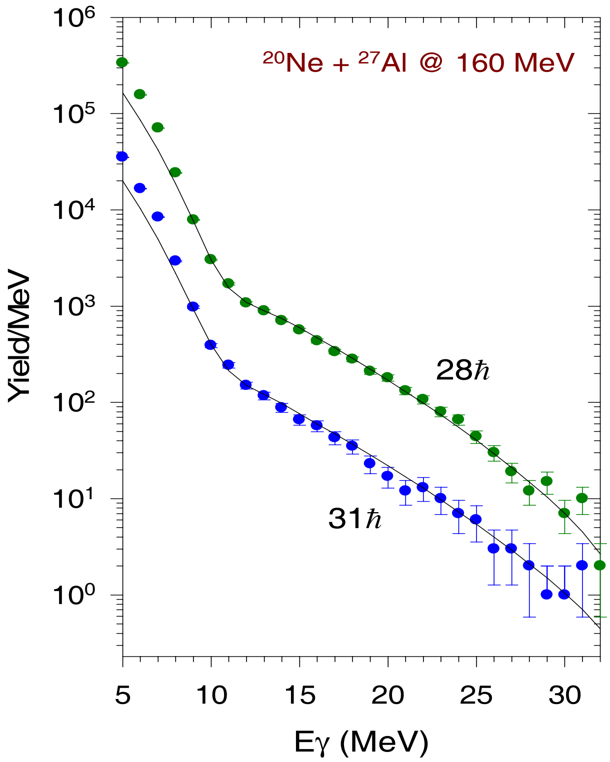


Figure 4.14: *The high-energy $\gamma$-ray spectra (filled circles) along with CASCADE prediction (continuous line) consisting of five GDR component for $^{47}$V nucleus.*

Table 4.2: The extracted GDR components for two angular momentum windows for $^{47}$V.

| <J> = 28 $\hbar$ | | | <J> = 31 $\hbar$ | | |
|---|---|---|---|---|---|
| $E_i$ (MeV) | $\Gamma_i$ (MeV) | $S_i$ | $E_i$ (MeV) | $\Gamma_i$ (MeV) | $S_i$ |
| 9.9±0.5 | 3.0±0.5 | 0.18±0.02 | 9.9±0.4 | 3.0±0.5 | 0.18±0.03 |
| 14.5±0.4 | 5.3±1.1 | 0.16±0.04 | 14.1±0.6 | 5.1±0.9 | 0.16±0.06 |
| 18.3±1.0 | 8.1±0.9 | 0.19±0.06 | 18.4±0.8 | 8.4 ±1.1 | 0.19±0.08 |
| 23.1±0.8 | 11.3±1.4 | 0.20±0.08 | 23.0±1.2 | 11.5±1.7 | 0.20±0.08 |
| 27.3±1.5 | 15.5±1.7 | 0.27±0.10 | 27.8±1.8 | 15.8±2.0 | 0.27±0.11 |

experimental and calculated spectra, respectively. The best fit GDR strength function $F_L(E_\gamma)$ in this case consists of 5-component Lorentzian function (table 4.2). The linearized GDR plots for the two angular momentum windows are

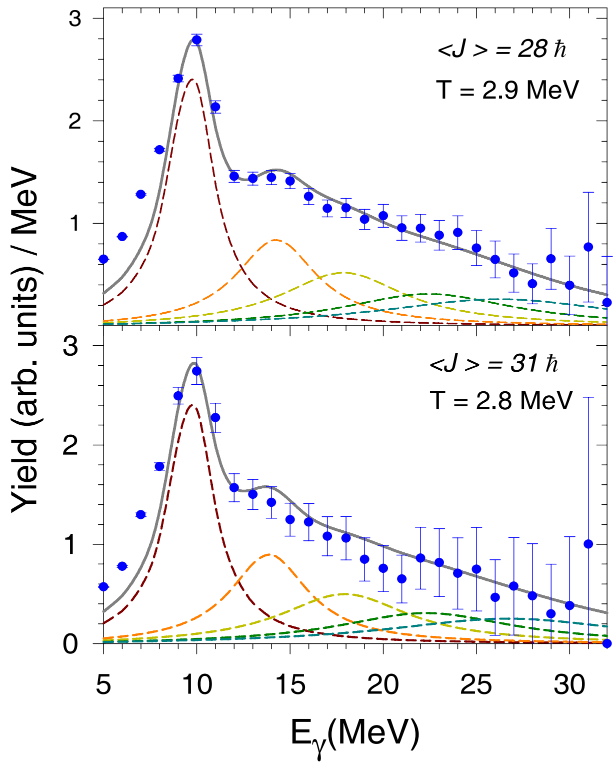


Figure 4.15: *The linearized experimental GDR strength function (filled circles) together with best fitting 5-Lorentzian function (continuous line) and its individual components.*

shown in Fig.4.15 along with the five GDR components used in the CASCADE calculation. Since, the width of the experimental angular momentum windows are large and the spin distributions corresponding to two different fold cuts (2 & $\geq$ 3) largely overlap, the GDR parameters and the overall GDR lineshapes are similar.

## 4.6 Result

The most striking feature of $^{47}$V populated at $28\hbar$ and $31\hbar$ is the strong enhancement in the $\gamma$ yield at $\sim$10 MeV similar to one observed in $^{46}$Ti [Maj04]. It is characteristics of a large deformation and the effect of Coriolis splitting due to very high angular velocity in the system [Dee10a]. Such very high an-

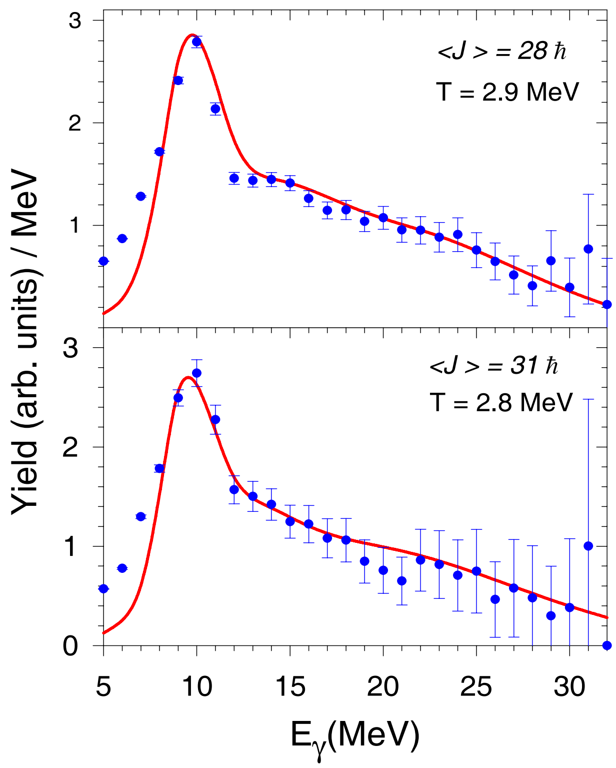


Figure 4.16: *The predicted line shapes from the free energy minimization technique (continuous lines) are compared with the linearized GDR strength functions for $^{47}V$ for the two angular momentum windows. The filled circles are the experimental data.*

gular velocities are usually achieved by the system normally beyond the Jacobi transition point. The average temperature of $^{47}$V nuclues was calculated using the relation $E_x = \tilde{a}T^2$ where $E_x = E^* - E_{rot} - E_{GDR}$ and $\tilde{a} = A/8$. $E^*$ is the excitation energy of the compound nucleus and $E_{rot}$ the energy bound in rotation. The GDR energy was extracted considering a single lorentzian from the relation $E_{GDR} = 18 \cdot A^{-1/3} + 25 \cdot A^{-1/6}$ [Gaa92]. The average temperatures corresponding to fold 2 and fold $\geq$ 3 were 2.9 and 2.8 MeV, respectively.

In order to interpret the extracted GDR strength functions in the entire $\gamma$-ray energy range (5 - 32), we performed the thermal shape fluctuation calculation to generate the theoretical GDR strength function. The resulting GDR strength function, obtained as a weighted average (with the weight given by the Boltzmann factor) of strength functions calculated at each $\beta, \gamma$ point (also including the Coriolis effects), is displayed with the full line in Fig.4.16 and compared with the experimental data. It describes the data for $^{47}$V remarkably well for both the experimentally measured spin windows of $28\hbar$ and $31\hbar$ at corresponding temperatures of 2.9 and 2.8 MeV, respectively. This remarkable good agreement between the theoretical predictions and the present experimental results is very much in favour of the onset of the Jacobi transition. Moreover, the appearance of a GDR component at $\sim$10 MeV is only possible due to the Coriolis splitting at very high angular frequency of the lowest vibrational frequency (which corresponds to the dipole vibration along the longest axis of the well deformed prolate or triaxial shape) [Dee10a]. In fact, for oblate shapes, typical for the equilibrium deformation at rotational frequencies lower than the critical value for the Jacobi transition, the Coriolis splitting is always absent [Nee82]. A further signature for the Jacobi transition is the presence of a broad tail in the 20-30 MeV region, in addition to the main peak at $E_\gamma \sim 18$ MeV. This result shows the importance of the selection of high rotational frequencies in the investigation of nuclear shapes through the GDR $\gamma$-decay.

The Jacobi shape transition has also been confirmed in our other experiment [Drc12] populating $^{46}$Ti via the reaction $^{19}$F (75, 125 MeV) + $^{27}$Al performed at the Pelletron accelerator of the Tata Institute of Fundamental Research, Mumbai, India. A sharp low-energy (at $\sim$10 MeV) component has been observed in the gamma-ray strength function superimposed on a broad distribution. At the higher beam energy, the component becomes more prominent at higher angular momentum, whereas for the lower beam energy the component disappears for higher fold. The comparison of the data at the two beam energies indicates that the critical angular momentum for the Jacobi transition is consistent with the theoretical prediction of $\sim 28\hbar$.

# Chapter 5

# Giant dipole resonance $\gamma$-rays from hot $^{32}$S nucleus

## 5.1 Introduction

In recent years, there have been intense theoretical and experimental efforts [Bec09] to search for highly (super/hyper) deformed (SD/HD) nuclear systems. There are indications that such highly deformed shapes are likely to be observed in light $\alpha$-like systems ($A_{CN} \sim$ 20-60) at higher angular momenta (typically $\geq$ 15 $\hbar$) and excitation energies (typically $\geq$ 40 MeV). Experimentally, large deformations were observed in $^{36}$Ar [Sve00] and $^{40}$Ca [Ide01], where the deformations were studied using $\gamma$-spectroscopic techniques. Such large deformations observed in light $\alpha$-like systems are believed to be due to the occurrence of either quasimolecular resonances or nuclear orbiting [San99], which has the origin in $\alpha$-cluster structure of these nuclei. The $^{20}$Ne + $^{12}$C reaction populating $^{32}$S is a well-established orbiting system [Sha79]. Our previous studies on enhancement of fragment yield near the entrance channel [Cha05] as well as $\alpha$-spectroscopic studies [Apa06] have strongly indicated a highly deformed orbiting dinuclear shape for $^{32}$S. However, no attempt has been made yet to see this large deformation directly via the splitting of the GDR strength function.

The statistical decay of the GDR from self-conjugate nuclei (e.g $^{32}$S in this case ) built on highly excited states, when populated by T=0 reaction channel ($^{20}$Ne + $^{12}$C), depends strongly on the isospin mixing due to the isovector character of the GDR [Har86, Beh93]. The E1 emission associated with the decay of the GDR ($\Delta$T=1) is hindered since decays from T=0 to T=0 states are isospin forbidden. The transitions from T=0 to T=1 states are allowed, but there are not many T=1 final states available to be populated by the GDR decays. However, the yield of high-energy $\gamma$-rays from N=Z compound nuclei increases in the presence of isospin mixing. The experimental method of extracting the isospin mixing probability was pioneered by Harakeh [Har86] and improved by Behr [Beh93]. It is based on the measurements of the high-energy $\gamma$-ray yields from the statistical decay of the GDR built in neighbouring N=Z and N$\neq$Z compound nuclei at similar excitation energy. Similar method was used to determine the degree of isospin mixing in $^{32}$S [Kin04], $^{36}$Ar, $^{44}$Ti, $^{60}$Zn [Woj06] and recently in $^{80}$Zr [Cor11]. Conversely, if the initial state is not pure in isospin but contains an admixture of T=1 states, it can decay to the more numerous T=0 final states. Thus, the first-step $\gamma$ yield depends on the degree of isospin mixing of the compound nucleus [Har86, Beh93].

In heavy ion collisions with bombarding energies well above the Coulomb barrier, a significant fraction of the light charged particle (particularly protons) is known to be emitted at forward angles in the early stage of the reaction [Awe81]. This extra contribution in the forward direction is generally a signature of pre-equilibrium nucleon emission. Hence, the statistical emission of $\gamma$-rays may also arise following incomplete fusion or pre-equilibrium nucleon emission [Kin04]. Thus, a decaying compound nucleus may not be a N=Z nucleus. The mass and charge of the compound nucleus as well as the excitation energy are expected to be lower than in case of complete fusion. Apart from that bremsstrahlung $\gamma$-ray emission should also be included in the analysis [Kin04].

Thus, it would be interesting to explore the shapes of the light $\alpha$-like systems directly through the GDR $\gamma$ decays in reactions above 7 MeV/nucleon, which would help in understanding the reaction dynamics of light $\alpha$-like systems and compare them with the corresponding Jacobi shapes in hot rotating compound nuclei.

## 5.2 Experimental details

The $^{32}$S compound nucleus was formed at initial excitation energies of 73 and 78 MeV, using the reaction $^{20}$Ne + $^{12}$C with a pulsed $^{20}$Ne beam at $E_{proj}$ = 145 and 160 MeV, respectively, from the K-130 room temperature cyclotron at the Variable Energy Cyclotron Centre. A self-supporting carbon target of 1 mg/cm$^2$ thickness was used. Since it is difficult to extract the angular momentum for very low mass accurately, the experiment was performed with two incident energies, 145 and 160 MeV, in order to populate $^{32}$S nucleus at different spins. The corresponding grazing angular momentum values are 24$\hbar$ and 25$\hbar$, respectively, which extend well beyond the critical angular momentum value of 17.5$\hbar$ at which the Jacobi transition is predicted to occur for this nucleus [Dee10a].

The experimental technique was similar to that described previously for $^{47}$V in Chapter 4. A part of the LAMBDA spectrometer [Muk07] was employed to measure the high-energy gamma rays from the decay of hot $^{32}$S. An array of 49 $BaF_2$ detectors, each 35 cm long with a square cross-section of 3.5×3.5 cm$^2$, arranged in 7×7 matrix was kept at a distance of 50 cm from the target and at a lab angle of 55° with respect to the beam axis. Lead sheets of 5 mm thickness were placed in front and sides of the array, to cut down the intensity of the low energy gamma rays. The beam dump, located 3.0 meters downstream, was heavily shielded with borated paraffin blocks and lead bricks to cut down the gamma and neutron background. The in-house developed 50-

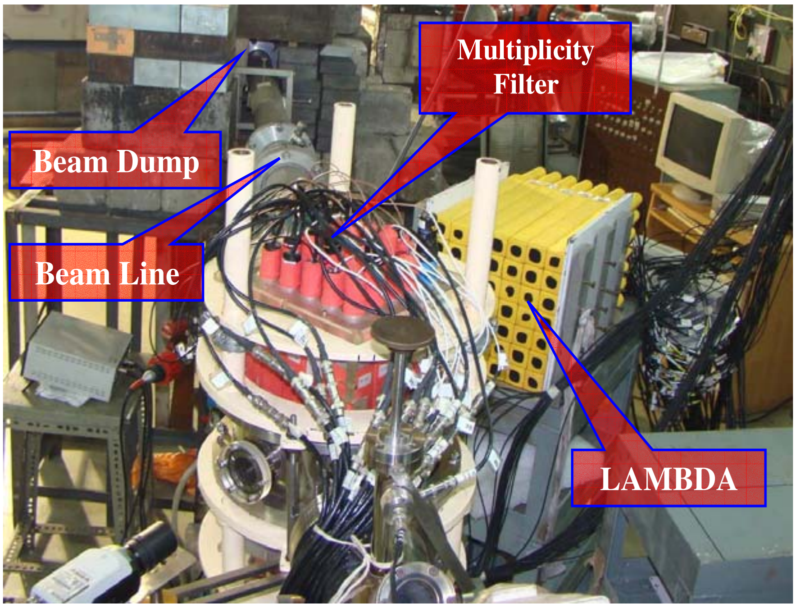


Figure 5.1: *The experimental setup of the LAMBDA spectrometer arranged in 7×7 matrix along with the multiplicity filter placed on top and bottom of the scattering chamber.*

element $BaF_2$ multiplicity filter [Dee10c] was also used to measure the discrete low energy multiplicity gamma rays, in coincidence with the high-energy gamma rays, to gate on the high angular momentum events of the compound nucleus as well as to get the start time trigger for time of flight (TOF) measurement. The multiplicity filter was configured in two closely packed groups of 25 detectors each, in a staggered castle type geometry, and placed above and below the scattering chamber. The efficiency of the multiplicity setup was ∼30% as calculated using the GEANT simulation. The experimental setup is shown in Fig.5.1. The neutron-gamma discrimination of the events in the large $BaF_2$ detectors (LAMBDA) was achieved through TOF measurement and the pile-up rejection was done using the pulse shape discrimination (PSD) technique by measuring the charge deposition over two integrating time intervals (50 ns and 2 $\mu$s). The electronic circuit and the trigger generation was same as in the case of $^{20}$Ne+$^{27}$Al experiment populating $^{47}$V and is discussed in Chapter 4.

## 5.3 Experimental data analysis

The high-energy gamma spectra were generated in off-line analysis of the data recorded in an event-by-event mode after putting proper cuts on the TOF and PSD (discussed in chapter 2). After application of different conditions, in a valid event, the energy deposited in the detectors was summed using the nearest neighbor event reconstruction technique [Muk07]. Finally, the energies were Doppler corrected. The high-energy spectra were generated for folds $\geq$3 for both the energies 145 & 160 MeV and is shown in Fig.5.2. The spectra were analyzed using the statistical code CASCADE [Pul77], described in Chapter 3, along with a bremsstrahlung component folded with the detector response function. The non-statistical bremsstrahlung component was parameterized using the relation $\sigma_{brem} = A \cdot exp(-E_\gamma/E_0)$. The inverse slope parameters were taken as 4.1 MeV$^{-1}$ and 4.3 for the incident energies 145 and 160 MeV, respectively, which are consistent with the bremsstrahlung systematics [Nif90]. The $r_0$, $\delta_1$ and $\delta_2$ parameters in CASCADE calculation were taken as 1.35 fm, 1.0 $\times$ $10^{-3}$ and 2.0 $\times$ $10^{-8}$, respectively. The level density prescription of Ignatyuk et al. [Ign75] was used with the asymptotic level density parameter $(\tilde{a})$=A/8.0 MeV$^{-1}$. The values of the different input parameters in CASCADE calculation were kept same as used for the charge particle analysis [Apa06] except for the $\delta_1$ parameter. It was changed from 3.5 $\times$ $10^{-3}$ to 1.0 $\times$ $10^{-3}$ in order to describe properly the low energy part of the high-energy $\gamma$ spectra.

At first, it needs to be mentioned that the statistical model code CASCADE used in the present thesis does not include the isospin effect. Hence, in order to visualize the GDR lineshapes, a linearization procedure, which is usually applied in the study of the GDR in hot nuclei, was adopted. The measured spectra have been divided by equivalent spectra calculated using constant B(E1) along with a bremsstrahlung component. The $\gamma$-ray cross-section below 10

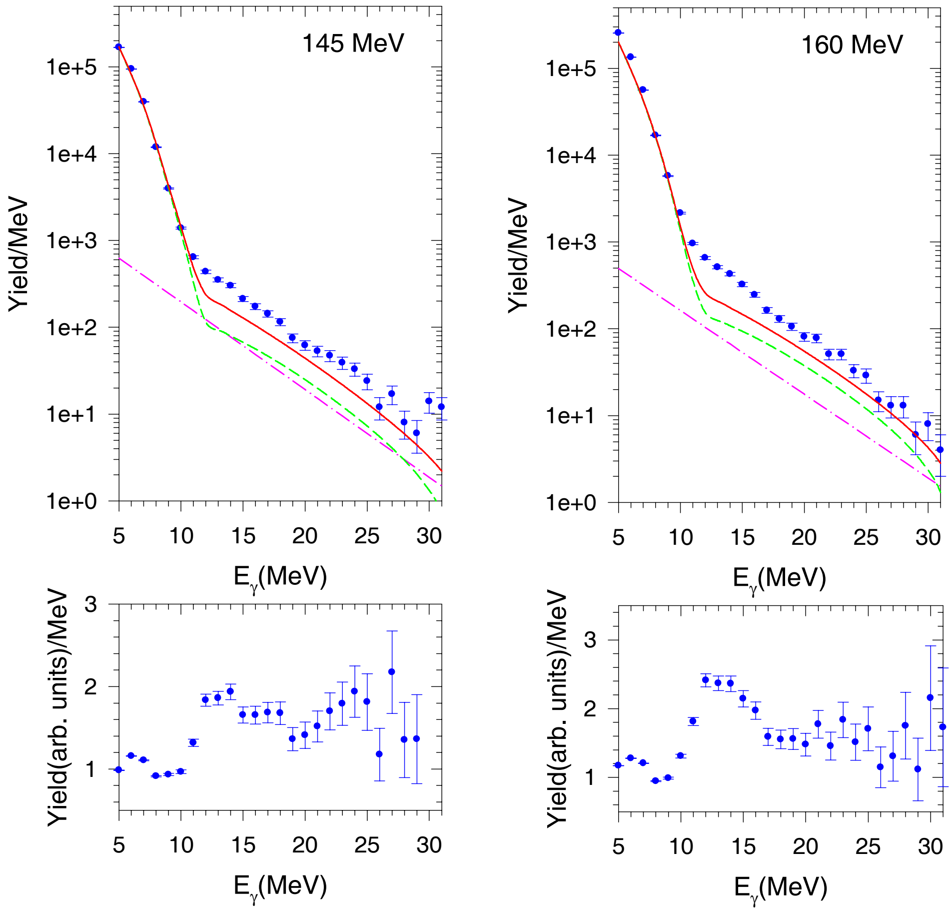


Figure 5.2: *The experimental high-energy $\gamma$-ray spectra (filled circles) for two incident beam energies for $^{32}$S nucleus. The dashed line corresponds to CASCADE calculation (without GDR strength function) while the dot-dashed line represents the bremsstrahlung component. The sum of the two (continuous line) is compared with the experimental data. The bottom panel shows the divided plot.*

MeV is mainly due to the $\gamma$-cascades in the residual nuclei populated below the particle emission threshold. Hence, the spectral shape below 10 MeV is almost independent of the isospin effect [Har86]. Thus, the divided plot would provide an idea about the shape of the GDR strength function. The linearized GDR lineshapes for 145 and 160 MeV incident energies are shown in Fig.5.2. It is interesting to note that the GDR lineshapes are completely different from $^{47}$V as observed in chapter 4. It appears that the GDR strength function, for both the incident energies, consists of two components, one at $\sim$ 14 MeV and another at

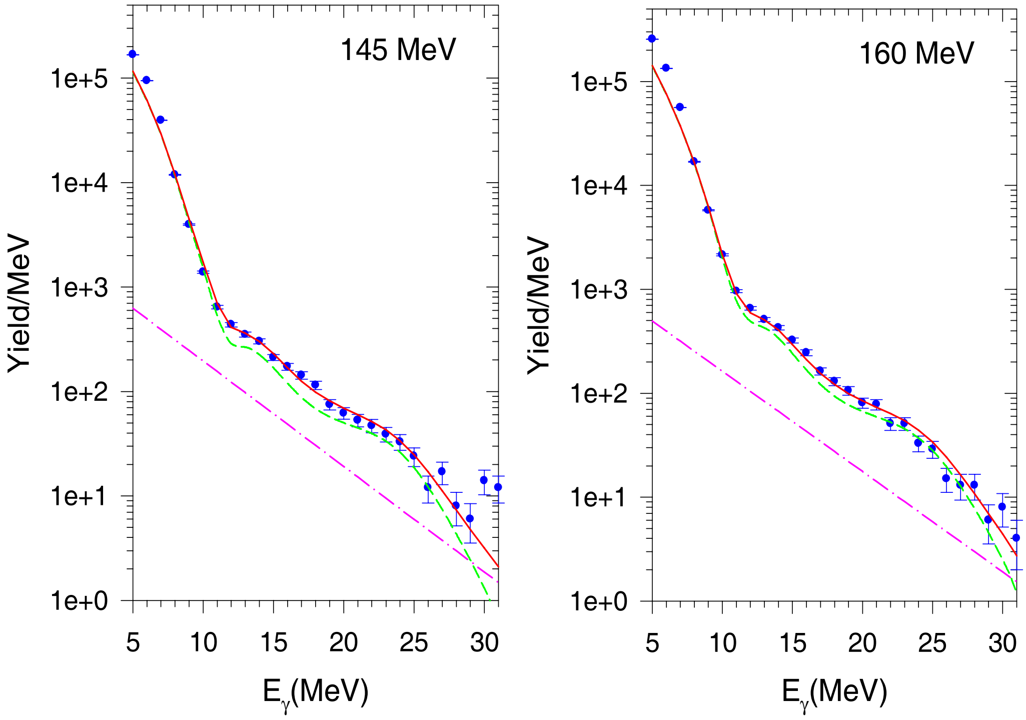


Figure 5.3: *The high-energy $\gamma$-ray spectra (filled circles) along with CASCADE prediction including GDR strength function (dashed line) for two incident beam energies for $^{32}$S nucleus. The dot-dashed line represents the bremsstrahlung component while the continuous line corresponds to CASCADE + bremsstrahlung.*

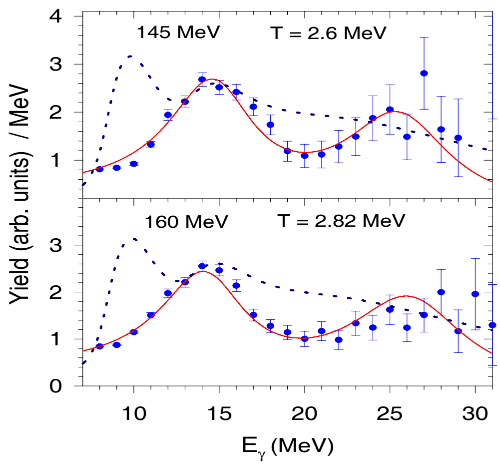


Figure 5.4: *The GDR lineshape for the two-incident energy. The symbols represent the experimental data; continuous lines correspond to the GDR strength functions used in CASCADE while the dashed lines represent the TSFM calculation for $^{32}$S nucleus at J=22$\hbar$ and $T$ = 2.8 MeV.*

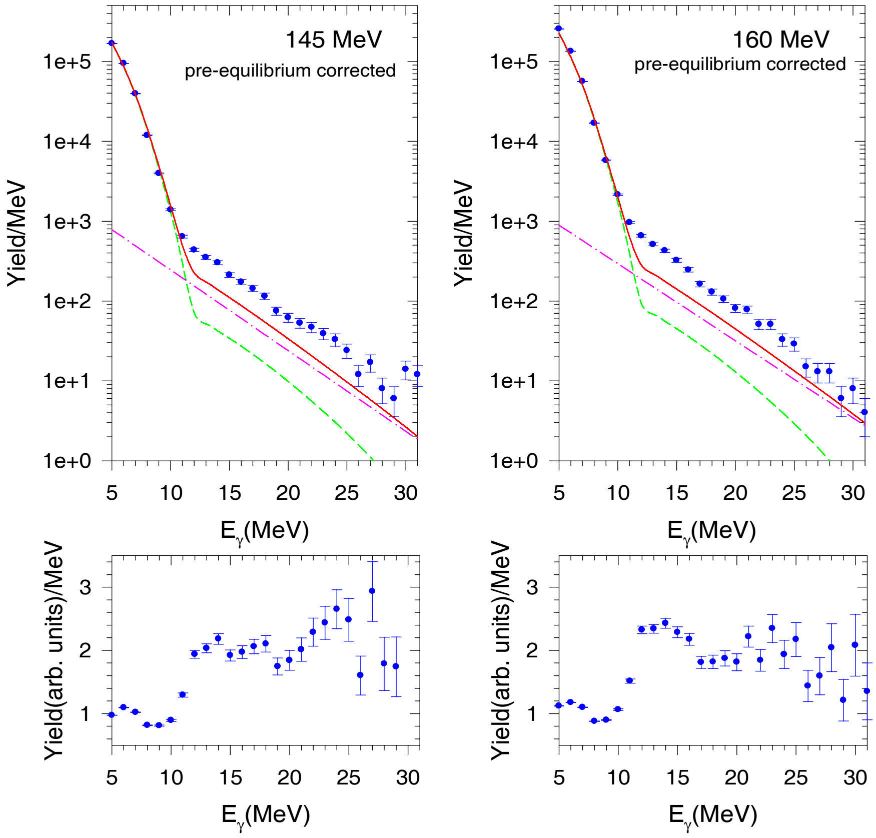


Figure 5.5: *Same as Fig.5.2 but with pre-equilibrium correction.*

$\sim$ 25 MeV. In order to compare the data with thermal shape fluctuation model (TSFM), statistical model analysis was performed including the GDR strength function along with the bremsstrahlung component (Fig.5.3). The extracted GDR parameters using $\chi^2$ minimization for the two incident beam energies 145 and 160 MeV are listed in table 5.1. However, the extracted parameters may not be correct as the statistical calculation was carried out without the isospin effect. In order to emphasize the GDR region, the linearized GDR plots are shown in Fig.5.4 using the quantity $F(E_\gamma)Y^{exp}(E_\gamma)/Y^{cal}(E_\gamma)$, where, $Y^{exp}(E_\gamma)$ and $Y^{cal}(E_\gamma)$ are the experimental and the best fit CASCADE spectra. The best fit GDR strength function $F(E_\gamma)$ in this case consists of a 2-component Lorentzian function.

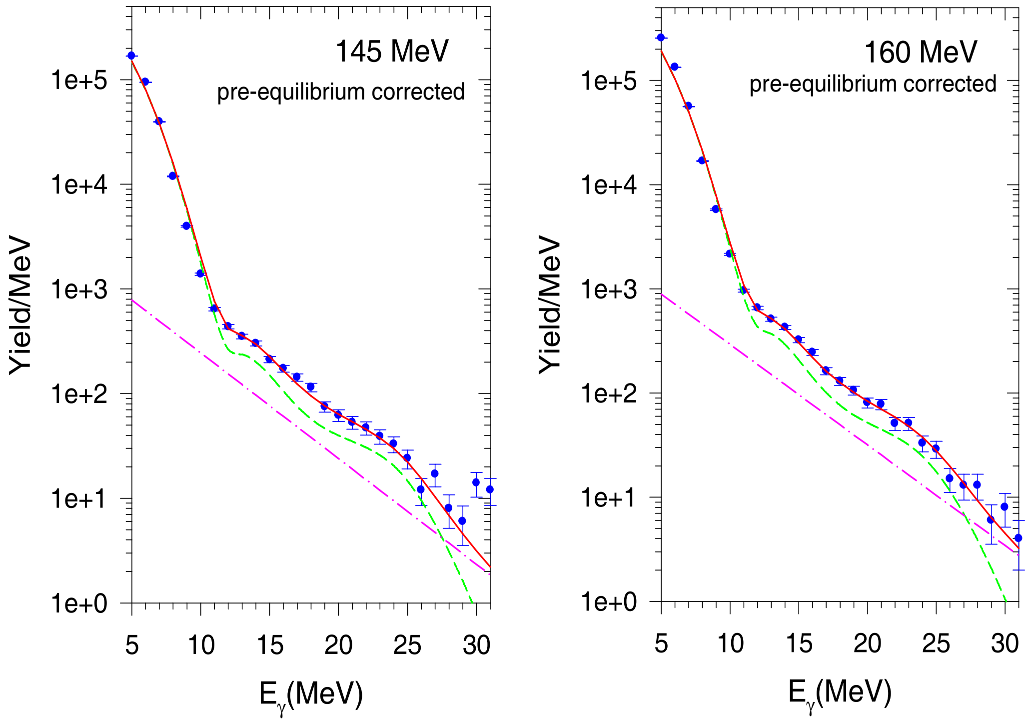


Figure 5.6: *Same as Fig.5.3 but with pre-equilibrium correction.*

The $^{20}$Ne+$^{12}$C system was studied earlier at 5 MeV/nucleon and 9.5 MeV/ nucleon to extract the degree of isospin mixing in $^{32}$S [Kin04]. It was observed that the isospin mixing is small at excitation energy of 58 MeV. However, at projectile energy of 9.5 MeV/ nucleon a large amount of bremsstrahlung $\gamma$-ray emission and strong influence of incomplete fusion was reported. It was concluded that only a fraction of $\gamma$-rays probably decay from the N=Z compound nuclei and more exclusive experiment would be needed to determine the degree of isospin mixing in this case. In our charge particle experiments for $^{20}$Ne ($\sim$ 7-10 MeV/nucleon) + $^{12}$C reactions, a significant contribution from pre-equilibrium process at forward angles was observed in the proton emission [Apa09]. Hence, the high energy $\gamma$-ray spectra have been re-analyzed including the pre-equilibrium effect in analogy with Ref [Kin04]. The initial excitation energies of the compound nucleus were 73 and 78 MeV for 145 and 160 MeV incident energies, respectively. The excitation energy losses due to incomplete fusion was estimated using the empirical formula proposed by M. Kelly [Kel99] and obtained $\Delta E_x = 21$ MeV for 145 MeV incident energy and $\Delta E_x = 26$ MeV for 160 MeV incident energy. Next, the high energy $\gamma$-ray spectra, for both the incident energies, were calculated assuming the decay of $^{31}$P at appropriate effective excitation of $E_x = 52$ MeV. The statistical model analysis including pre-equilibrium correction is shown in Fig.5.5. Again the measured experimental data have been divided by the equivalent spectra calculated using constant B(E1) in CASCADE along with a bremsstrahlung component. Interestingly, the linearized GDR strength functions look very similar to the ones obtained without pre-equilibrium correction. In this case also it appears that the GDR lineshape consists of two components, one at $\sim 14$ MeV and another at $\sim 25$ MeV. The GDR parameters were estimated performing statistical model analysis including the GDR strength function along with the bremsstrahlung component (Fig.5.6). In order to compare the data with thermal shape fluctuation model (TSFM), the linearized GDR plots are shown in Fig.5.7 using the quantity $\mathrm{F(E_\gamma)Y^{exp}(E_\gamma)/Y^{cal}(E_\gamma)}$, where, $\mathrm{Y^{exp}(E_\gamma)}$ and $\mathrm{Y^{cal}(E_\gamma)}$ are the experimental and the best fit CASCADE spectra. The extracted GDR parameters using $\chi^2$ minimization for the two incident beam energies of 145 and 160 MeV are listed in table 5.2.

As can be seen from table 5.1 and table 5.2 that the extracted GDR parameters are very similar for both the analysis i.e. without pre-equilibrium and with pre-equilibrium effect. The only change observed was the overall magnitude of the strength function of the GDR decay. For pre-equilibrium analysis, 1.3 times the energy weighted sum rule (EWSR) strength was required. Thus, it appears that the GDR parameters (specially the centroid energies that provide information of the deformation) will not be significantly modified if isospin effect

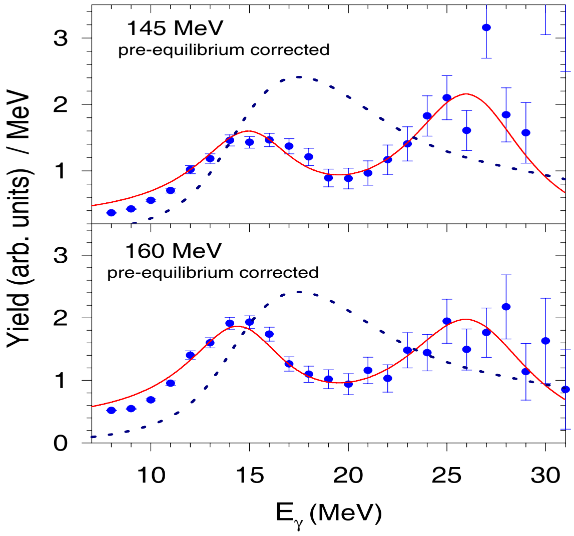


Figure 5.7: *The GDR lineshape for the two-incident energy (with pre-equilibrium correction). The symbols represent the experimental data; continuous lines correspond to the GDR strength functions used in CASCADE while the dashed lines represent the TSFM calculation for $^{31}$P nucleus at $J = 16\hbar$ and $T = 1.9$ MeV.*

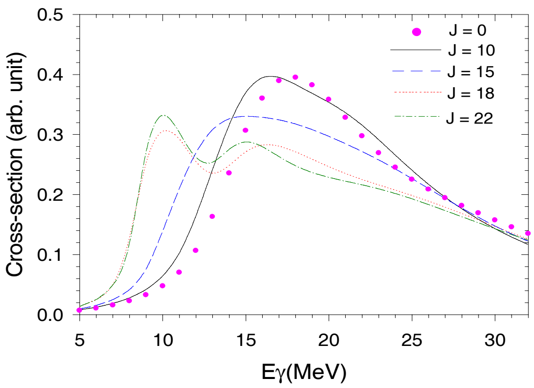


Figure 5.8: *The evolution of GDR lineshape with angular momentum for $^{32}$S nucleus at $T = 2.8$ MeV.*

included statistical model calculations are performed. The isospin effect inhibits the overall strength function of the GDR decay. Therefore, it is expected that the spectral shape of the spectrum will not change rather the overall magnitude of the strength function will be modified. The main aim of the experiment was to view the deformation via splitting of the GDR lineshape, i.e. shape of the

Table 5.1: The extracted GDR components for two incident energies for $^{32}$S.

| $E_{Lab}$ = 145 MeV | | | $E_{Lab}$ = 160 MeV | | |
|---|---|---|---|---|---|
| $E_i$ (MeV) | $\Gamma_i$ (MeV) | $S_i$ | $E_i$ (MeV) | $\Gamma_i$ (MeV) | $S_i$ |
| 14.5 ± 0.3 | 6.2 ± 0.8 | 0.37 ± 0.05 | 14.0 ± 0.4 | 6.2 ± 0.9 | 0.32 ± 0.05 |
| 25.4 ± 0.8 | 7.5 ± 1.3 | 0.63 ± 0.09 | 26.0 ± 0.9 | 8.2 ± 1.8 | 0.68 ± 0.10 |

Table 5.2: The extracted GDR components including pre-equilibrium correction.

| $E_{Lab}$ = 145 MeV | | | $E_{Lab}$ = 160 MeV | | |
|---|---|---|---|---|---|
| $E_i$ (MeV) | $\Gamma_i$ (MeV) | $S_i$ | $E_i$ (MeV) | $\Gamma_i$ (MeV) | $S_i$ |
| 14.8 ± 0.5 | 6.3 ± 1.0 | 0.3 ± 0.06 | 14.3 ± 0.4 | 6.3 ± 0.9 | 0.35 ± 0.04 |
| 26.0 ± 0.9 | 7.3 ± 1.2 | 1.0 ± 0.11 | 26.0 ± 0.8 | 8.0 ± 1.9 | 1.0 ± 0.12 |

strength function and to determine its the absolute magnitude. However, it is beyond the scope of present thesis to carry out the calculations by including the effect of isospin to verify the GDR parameters. Moreover, it was also concluded in Ref [Kin04] that it would be an impossible task to deduce the isospin mixing at 9.5 MeV/nucleon by the same technique as used at 5 MeV/nucleon. Interestingly, the double hump nature of the experimental data is also seen (even in logarithmic scale) in the Ref [Kin04] for 9.5 MeV/nucleon reaction. However, the analysis was performed using single GDR component which did not represent well the high energy part of the experimental data.

## 5.4 Result

Interestingly, in the case of $^{20}$Ne + $^{12}$C reaction populating $^{32}$S, no enhancement at ∼10 MeV is observed, contrary to $^{47}$V, even though the nucleus is populated well beyond the Jacobi transition point. In fact, five GDR components were not required in this case to explain the experimental data. The GDR lineshapes for $^{20}$Ne + $^{12}$C reactions are completely different from the one observed for $^{47}$V nucleus in Chapter 4. In fact, the lineshapes are also remarkably different from those one usually gets in the case of a spherical or a near spherical system and indicate large deformations. The shape looks more like a highly extended prolate and is seen for the first time for this nucleus. Applying the relation in eqn.(1.12), we get the deformation of $^{32}$S, from the two GDR peaks, as $\beta = 0.76$ corresponding to an axis ratio of 1.94:1 at 160 MeV incident energy. The temperature of $^{32}$S nucleus was calculated from the initial excitation energy after subtracting the rotational energy and the GDR resonance energy. The rotational energy was calculated corresponding to the critical angular momentum $\sim 25\hbar$. The single GDR peak was considered and extracted from the relation $E_{GDR} = 18 \cdot A^{-1/3} + 25 \cdot A^{-1/6}$ [Gaa92] used for GDR built on excited states. The temperatures corresponding to 73.0 and 78.0 MeV excitation energies were 2.60 and 2.82 MeV, respectively. For pre-equilibrium analysis, the temperature is 1.9 MeV corresponding to the excitation energy of 52 MeV.

In order to understand the experimental GDR strength functions in the entire $\gamma$-ray energy range (5 - 32), the free energy calculations, similar to $^{47}$V, were performed. The GDR lineshapes for $^{32}$S nucleus were generated for both low and high angular momentum window but it failed miserably to explain the experimental result. The evolution of the GDR lineshape as function of $J$ for $^{32}$S is shown in Fig.5.8. The calculation performed at J=22$\hbar$ & T=2.8 MeV is shown in Fig.5.4 while the calculation performed at lower angular momentum for $^{31}$P at J=16$\hbar$ & T=1.9 MeV is shown in Fig.5.7.

The occurrence of such a large deformation without showing the characteristics of Jacobi transition is possible only if some other reaction mechanism is responsible. One of the possibilities could be due to the formation of a long lived, highly deformed orbiting dinuclear complex where the nucleus is not fully equilibrated (in terms of shape degrees of freedom) and maintains the entrance channel shape before finally splitting into two parts. In our charge particle experiment [Cha05] for $^{20}$Ne ($\sim$ 7-10 MeV/nucleon) + $^{12}$C reactions, yields of carbon and boron fragments were significantly enhanced, which indicated the survival of orbiting at these high excitation energy. The estimated deformation for $^{32}$S, as extracted from the inclusive $\alpha$-particle evaporation using CASCADE calculation, was also found to be much larger than the 'normal' deformation of hot, rotating composites at similar excitations which also indicated towards the formation of orbiting dinuclear complex [Apa06]. Thus, it appears that the strong deformation extracted from the resonance energy peaks observed for $^{32}$S ($\beta = 0.76$) is due to the formation of long-lived orbiting-like dinuclear system.

However, it can also be conjectured that the observed unusual deformation can be due to the formation of the molecular structure of the $^{16}$O+$^{16}$O cluster in $^{32}$S. In the theoretical work of Kimura and Horiuchi [Kim04], it was predicted that the SD states of $^{32}$S have considerable amount of $^{16}$O+$^{16}$O components and become more prominent as the excitation energy increases. The estimated deformation for two touching $^{16}$O was found to be $\beta = 0.73$ which is in agreement with the experimentally extracted deformation from the resonance energy peaks ($\beta = 0.76$). The occurrence of GDR in nuclei, where the entire nucleus takes part in a collective manner, is clearly an effect of the mean field structure of the nucleus. It is also known that other inherent structures (molecular resonance and/or orbiting dinuclear complex) in light $\alpha$-cluster nuclei may coexist with the mean field description of the nucleus. Whether the experimental signatures of the overall nuclear deformation via GDR $\gamma$ decay is due to the coexistence of these effects needs to be investigated further and are beyond the scope of this present study.

# Chapter 6

# Summary and conclusion

It is clear from the results presented in the thesis that the $\gamma$-decay from the giant dipole resonance can be used to study the different reaction mechanisms. The linearized GDR lineshapes for the systems $^{47}$V and $^{32}$S populated via $^{20}$Ne + $^{27}$Al and $^{20}$Ne + $^{12}$C, respectively, are remarkably different from each other. Interestingly, the two lineshapes are also dissimilar from what is expected for a spherical or a near spherical system pointing towards large deformations. The most striking feature for $^{47}$V is the strong enhancement in the $\gamma$-ray yield at $\sim 10$ MeV. It is the characteristics of Jacobi shape transition, an abrupt change from an oblate to an elongated triaxial shape, and Coriolis effect due to high angular momentum. The experimental results are also consistent with the predictions of a hot rotating liquid drop model.

It is well known that the $\gamma$-ray yield from the decay of the GDR in self-conjugate nuclei ($^{32}$S) populated by T=0 entrance channel are found to be strongly inhibited due to the isovector nature of the electric dipole radiation and increase in the presence of isospin mixing. However, in heavy ion collision at projectile energies above 6 MeV/nucleon, incomplete fusion and pre-equilibrium emission processes also occur. Hence, the high energy $\gamma$-rays may also arise following incomplete fusion and pre-equilibrium nucleon emission.

Since the statistical model code CASCASE used in the thesis does not include the effect of isospin, the data have been analyzed twice i.e. considering pre-equilibrium emission and without pre-equilibrium emission. For both the cases, the GDR parameters are very similar except for the overall GDR strength function. Thus, it is expected that the isospin included statistical model analysis will not change the spectral shape of the resonance but rather the overall magnitude of the strength function will be modified. Interestingly, no enhancement is seen at $\sim$ 10 MeV for $^{20}$Ne + $^{12}$C reactions populating $^{32}$S although it is populated well beyond the Jacobi transition point. The shape looks more like a highly extended prolate and is seen for the first time for this nucleus. In this case, the thermal shape fluctuation model fails to explain the experimental data. The occurrence of such a large deformation without showing the characteristics of Jacobi transition is possible only if some other reaction mechanism is responsible. This unusual deformation has been speculated due to the formation of either the orbiting dinuclear configuration or the molecular structure of $^{16}$O + $^{16}$O forming a super-deformed structure in $^{32}$S at high excitation.

It is interesting to note that the Jacobi shape transition is seen only upto A = 50. However, it is predicted to take place in heavier nuclei, atleast upto A$\sim$100, where the angular momentum corresponding to Jacobi transition is less than that of the fission limit. Thus, it would be an exciting study to look for the Jacobi transition in heavier mass systems in future. Similar to the $^{32}$S nucleus, a strong entrance channel effect is also seen for heavier nuclei in the reactions $^{16}$O + $^{89}$Y and $^{16}$O + $^{93}$Nb pointing towards the formation of orbiting dinuclear configuration. However, in the case of $^{12}$C + $^{93}$Nb no such large back-angle yield is observed [Ray91]. It would be interesting to measure the GDR $\gamma$-decay from these systems to look for the anomaly observed in the corresponding charged particle experiments.

Apart from the heavy-ion reaction, an extensive experiment was carried out to study the emission of high-energy photons from the spontaneous fission of $^{252}$Cf source. Interestingly, high-energy $\gamma$-rays upto 80 MeV have been observed in the experiment. The $\gamma$-rays in the range 8-20 MeV are attributed to the GDR $\gamma$-decay from the excited fission fragments while the spectrum above 20 MeV is attributed to the coherent bremsstrahlung $\gamma$-rays due to acceleration of the fission fragments in their mutual Coulomb field. The result has been substantiated with a theoretical calculation by estimating the emission of $\gamma$-rays considering classical Coulomb acceleration. This approximate calculation describes the experimental data remarkably well when the pre-scission kinetic energies of the emitted fission fragments and the conservation of energy are taken into account.

# Bibliography


[Alh86] Y. Alhassid, S. Levit and J. Zingman, "Universal Features of Shape Transitions in Hot Rotating Nuclei", Phys. Rev. Lett. 57 (1986) 539.

[Alh87] Y. Alhassid, J. Zingman and S. Levit, "Landau theory of shape transitions in hot rotating nuclei", Nucl. Phys. A469 (1987) 205.

[Alh88] Y. Alhassid, B. Bush and S. Levit, "Thermal Shape Fluctuations, Landau Theory, and Giant Dipole Resonances in Hot Rotating Nuclei", Phys. Rev. Lett. 61 (1988) 1926.

[Alh90] Y. Alhassid and B. Bush, "Effects of thermal fluctuations on giant dipole resonances in hot rotating nuclei", Nucl. Phys. A509 (1990) 461.

[Alh92] Y. Alhassid and B. Bush, "The systematics of the Landau theory of hot rotating nuclei", Nucl. Phys. A549 (1992) 12.

[Alh93] Y. Alhassid and N. Whelan, "The Jacobi transition and the giant-dipole resonance in rapidly rotating hot nuclei", Nucl. Phys. A565 (1993) 427.

[Alh99] Y. Alhassid, "Giant dipole resonances in hot rotating nuclei: Overview and recent advances", Nucl. Phys. A649 (1999) 107c.

[Apa06] Aparajita Dey, S. Bhattacharya, C. Bhattacharya, K. Banerjee, T. K. Rana, S. Kundu, S. Mukhopadhyay, D. Gupta, and R. Saha, "Evidence of large nuclear deformation of $^{32}S^{*}$ formed in the $^{20}Ne+^{12}C$ reaction", Phys. Rev. C74 (2006) 044605.

[Apa09] Aparajita Dey S. Bhattacharya, C. Bhattacharya, K. Banerjee, T. K. Rana, S. Kundu, s. R. Banerjee, S. Mukhopadhyay, D. Gupta, and R. Saha, "Light-charged-particle emission from hot $^{32}S^{*}$ formed in the $^{20}Ne+^{12}C$ reaction" European Phys. Journal A 41 (2009) 39.

[Aru04] P. Arumugam, G. Shanmugam and S. K. Patra, "Giant dipole resonance and Jacobi transition with exact treatment of fluctuations", Phys. Rev. C69 (2004) 054313.

[Awe81] T. C. Awes, G. Poggi, C. K. Gelbke, B.B.Back, B.G. Glagola H. Breuer and V. E. Viola, Jr, "Precompound emission of light particles in the reaction $^{16}$O + $^{238}$U 20 Mev/nucleon", Phys. Rev. C24 (81) 89.

[Bal47] G. C. Baldwin and G. S. Klaiber, "Photo-Fission in Heavy Elements", Phys. Rev. 71 (1947) 3.

[Bar97] V. Baran, A. Bonasera, M. Colonna, M. Di toro and A. Guarnera, "Giant resonances built on highly excited states: A test-ground for nuclear dynamics", Prog. Nucl. Part. Phys. 38 (1997) 263.

[Bec93] C. Beck, B. Djerroud, F. Haas, R. M. Freeman, A. Hachem, B. Heusch, A. Morsad, and M. Vuillet-A-Cilles, "Asymmetric fission of $^{47}$V induced by the $^{23}$Na+$^{24}$Mg reaction", Phys. Rev. C 47 (1993) 2093.

[Bec09] C. Beck, P. Papka, A. Snchez i Zafra, S. Thummerer, F. Azaiez, P. Bednarczyk, S. Courtin, D. Curien, O. Dorvaux, D. Lebhertz, A. Nourreddine, M. Rousseau, W. von Oertzen, B. Gebauer, C. Wheldon, Tz. Kokalova, G. de Angelis, A. Gadea, S. Lenzi, S. Szilner3, D. R Napoli, W. N. Catford, D. G. Jenkins and G. Royer, "Binary reaction decays from $^{24}$Mg+$^{12}$C", Phys. Rev. C 80 (2009) 034604 and references therein.

[Beh93] J. A. Behr, K. A. Snover, C. A. Gossett, M. Kicinska-Habior, J. H. Gundlach, Z. M. Drebi, M. S. Kaplan and D. P. Wells, "Restoration of Isospin Symmetry in Highly Excited Compound Nuclei", Phys. Rev. Lett. 70 (1993) 3201.

[Ber69] R. Bergre, H. Beil, P. Carlos, A. Veyssire, "Sections efficaces photoneutroniques de I, Ce, Sm, Er et Lu", Nucl. Phys. A133 (1969) 417.

[Ber75] B. L. Berman and S. C. Fultz, "Measurements of the giant dipole resonance with monoenergetic photons", Rev. Mod. Phys. 47 (1975) 713.

[Bor91] P. F. Bortignon, A. Bracco, D. Brink and R. A. Broglia, "Limiting temperature for the existence of collective motion in hot nuclei", Phys. Rev. Lett. 67 (1991) 3360.

[Bor98] P. F. Bortignon, A. Bracco and R. A. Broglia, "Giant Resonances: Nuclear Structure at Finite Temperature", Harwood Academic Publishers, (1998).

[Bor01] P. F. Bortignon, "Spreading of giant resonances  Current status and perspective", Nucl. Phys. A 687 (2001) 329.

[Boh75] A. Bohr and B. Mottelson, "Nuclear Structure", (Vol. 2) Benjamin, New York, (1975).

[Bot37] W. Bothe, W. Gentner, Z. Phys. 71 (1937) 236.

[Bri62] P. Axel, "Electric Dipole Ground-State Transition Width Strength Function and 7-Mev Photon Interactions", Phys. Rev. 126 (1962) 671.

[Cam03] F Camera, A Bracco, V Nanal, M.P Carpenter, F Della Vedova, S Leoni, B Million, S Mantovani, M Pignanelli, O Wieland, B.B Back, A.M Heinz, R.V.F Janssens, D Jenkins, T.L Khoo, F.G Kondev, T Lauritsen, C.J Lister, B McClintock, S Mitsuoka, et al. "Radiative fusion from very symmetric reactions: the giant dipole resonance in the $^{179}$Au nucleus", Phys. Lett. B 560 (2003) 155.

[Cha69] S. Chandrasekhar, "Ellipsoidal figures of equilibrium", Yale Univ. Press, New Haven, (1969).

[Cha05] C. Bhattacharya, A. Dey, S. Kundu, K. Banerjee, S. Bhattacharya, S. Mukhopadhyay, D. Gupta, T. Bhattacharjee, S. R. Banerjee, S. Bhattacharyya, T. Rana, S. K. Basu, R. Saha, S. Bhattacharjee, K. Krishan, A. Mukherjee and D. Bandopadhyay, "Survival of orbiting in $^{20}$Ne (7-10 MeV/nucleon) + $^{12}$C reactions", Phys. Rev. C 72 (2005) 021601(R).

[Coh74] S. Cohen, F. Plasil and W.J. Swiatecki, "Equilibrium configurations of rotating charged or gravitating liquid masses with surface tension", Ann. Of Phys.(N.Y) 82 (1974) 557.

[Cor11] A. Corsi, O. Wieland, S. Barlini, A. Bracco, F. Camera, V. L. Kravchuk, G. Baiocco, L. Bardelli, G. Benzoni, M. Bini, N. Blasi, S. Brambilla, M. Bruno, G. Casini, M. Ciemala, M. Cinausero, F. C. L. Crespi, M. DAgostino, M. Degerlier,A. Giaz, F. Gramegna, M. Kmiecik, S. Leoni, A. Maj, T. Marchi, K. Mazurek, W. Meczynski, B. Million, D. Montanari, L. Morelli, S. Myalski,A. Nannini, R.

Nicolini, G. Pasquali, G. Poggi, V. Vandone, and G. Vannini “Measurement of isospin mixing at a finite temperature in $^{80}$Zr via giant dipole resonance decay”, Phys. Rev. C 84 (2011) 041304(R).

[Dan58] M. Danos, “On the long-range correlation model of the photonuclear effect”, Nucl. Phys. 5 (1958) 23.

[Dan98] Nguyen Dinh Dang and Akito Arima, “Quantal and Thermal Dampings of Giant Dipole Resonances in $^{90}$Zr, $^{120}$Sn, and $^{208}$Pb”, Phys. Rev. Lett. 80 (1999) 4145.

[Dan99] D. N. Dang, K. Tanabe and A. Arima, “Shape evolution of the hot giant dipole resonance”, Nucl. Phys. A645 (1999) 536.

[Dan11] Nguyen Dinh Dang, “Shear-viscosity to entropy-density ratio from giant dipole resonances in hot nuclei”, Phys. Rev. C 84 (2011) 034309

[Dav76] K. T. R. Davies and J. R. Nix, “Calculation of moments, potentials, and energies for an arbitrarily shaped diffuse-surface nuclear density distribution”, Phys. Rev. C 14 (1976) 1977.

[Dee10a] Deepak Pandit, S. Mukhopadhyay, Srijit Bhattacharya, Surajit Pal, A. De, S. Bhattacharya, C. Bhattacharya, K. Banerjee, S. Kundu, T. K. Rana, A. Dey, G. Mukherjee, T. Ghosh, D. Gupta, and S. R. Banerjee, “Extreme nuclear shapes examined via giant dipole resonance lineshapes in hot light-mass systems”, Phys. Rev. C81 (2010) 061302(R).

[Dee10b] Deepak Pandit, S. Mukhopadhyay, Srijit Bhattacharya, Surajit Pal, A. De, S.R. Banerjee, “Coherent bremsstrahlung and GDR width from $^{252}$Cf cold fission”, Phys. Lett. B690 (2010) 473.

[Dee10c] Deepak Pandit, S. Mukhopadhyay, Srijit Bhattacharya, Surajit Pal, A. De, S.R. Banerjee, “A realistic technique for selection of angular momenta from hot nuclei: A case study with $^{4}$He + $^{115}$In $\rightarrow$ $^{119}$Sb$^{*}$ at $E_{Lab}$ = 35 MeV”, Nucl. Inst. Meth. A624 (2010) 148.

[Dee12] Deepak Pandit, S. Mukhopadhyay, Surajit Pal, A. De and S. R. Banerjee, “Critical behavior in the variation of GDR width at low temperature”, Phys. Lett. B713 (2012) 434.

[Del10] J. -P. Delaroche, M. Girod, J. Libert, H. Goutte, S. Hilaire, S. Pru, N. Pillet, and G. F. Bertsch, “Structure of even-even nuclei using a mapped collective Hamiltonian and the D1S Gogny interaction”, Phys. Rev. C 81 (2010) 014303.

[Die74] F. S. Dietrich, J. C. Browne, W. J. OConnell and M. J. Kay, "Spectrum of $\gamma$ rays in the 8- to 20-MeV range from $^{252}$Cf spontaneous fission", Phys. Rev. C 10 (1974) 795.

[Die88] S. S. Dietrich and B. L. Berman, "Atlas of photoneutron cross sections obtained with monoenergetic photons", Atomic Data Nuclear Data Tables 38 (1988) 199.

[Dre95] Z. M. Drebi, K. A. Snover, A. W. Charlop, M. S. Kaplan, D. P. Wells, D. Ye and Y. Alhassid, "Spin-induced shape changes in light-medium mass compound nuclei", Phys. Rev. C 52 (1995) 578.

[Drc12] D. R. Chakrabarty, V. M. Datar, Suresh Kumar, G. Mishra, E. T. Mirgule, A. Mitra, P. C. Rout, V. Nanal, Deepak Pandit, S. Mukhopadhyay, and Srijit Bhattacharya, "Exclusive giant dipole resonance measurement on the Jacobi transition in the $^{19}$F + $^{27}$Al system", Phys. Rev. C 85, (2012) 044619.

[Dub05] N. Dubray, J. Dudek and A. Maj, "Statistical description of the thermal shape fluctuations using realistic microscopic and macroscopic models", Acta Physica Polonica B 36 (2005) 1161.

[Ere11] N V Eremin, S S Markochev, A A Paskhalov, G Mandaglio, M Manganaro, G Fazio, G Giardina and M V Romaniuk, "Investigation of high energy $\gamma$-rays accompanying spontaneous fission of $^{252}$Cf in double and triple neutron-$\gamma$ coincidences ", Journal of Physics:Conference series 282 (2011) 012017.

[Erh10] M. Erhard, A. R. Junghans, C. Nair, R. Schwengner, R. Beyer, J. Klug, K. Kosev, A. Wagner, E. Grosse,"Experimental study of the electric dipole strength in the even Mo nuclei and its deformation dependence", Phys. Rev. C 81 (2010) 034319.

[Gaa92] J. J. Gaardhoje, "Nuclear Structure at High Excitation Energy Studied with Giant Resonances", Ann. Rev. Nucl. Part. Sci. 42 (1992) 483.

[Gal85] M. Gallardo, M. Diebel, T. Dossing and R.A. Broglia, "Damping of the giant dipole resonance in hot, strongly rotating nuclei", Nucl. Phys. A443 (1985) 415.

[Gal87] M. Gallardo, F. J. Luis and R.A. Broglia, "Role of thermal fluctuations in the damping of the giant dipole resonance of spherical and deformed nuclei: $^{90}$Zr and $^{164}$Er", Phys. Lett. B191 (1987) 222.

[Gol48] M. Goldhaber and E. Teller, “On Nuclear Dipole Vibrations”, Phys. Rev. 74 (1948) 1046.

[Gun90] J. H. Gundlach, K. A. Snover, J. A. Behr, C. A. Gossett, M. Kicinska-Habior and K. T. Lesko, “Oblate deformed shapes of hot rotating nuclei deduced from giant-dipole-resonance decay studies”, Phys. Rev. Lett. 65 (1990) 2523.

[Har01] M. N. Harakeh and A. van der Woude, “Giant Resonances: Fundamental High-Frequency Modes of Nuclear Excitation”, Harwood Academic Publishers, (2001).

[Har86] M. N. Harakeh , D. H. Dowell, G. Feldman, E. F. Garman, R. Loveman, J. L. Osborne and K. A. Snover, “ Role of isospin in the statistical decay of the giant dipole resonance built on excited states”, Phys. Lett. B 176 (1986) 297

[Hec03] P. Heckman, D. Bazin, J.R. Beene, Y. Blumenfeld, M.J. Chromik, M.L. Halbert, J.F. Liang, E. Mohrmann, T. Nakamura, A. Navin, B.M. Sherrill, K.A. Snover, M. Thoennessen, E. Tryggestad, R.L. Varner, “Low-temperature measurement of the giant dipole resonance width”, Phys. Lett. B 555 (2003) 43

[Hil53] D. L. Hill and J. A. Wheeler, “Nuclear Constitution and the Interpretation of Fission Phenomena”, Phys. Rev. 89 (1953) 1102.

[Hof93] D. J. Hofman, B. B. Back, C. P. Montoya, S. Schadmand, R. Varma and P. Paul, “High energy $\gamma$ rays from $^{252}$Cf spontaneous fission”, Phys. Rev. C 47 (1993) 1103.

[Hui62] J. R. Huizenga and G. Igo, “Theoretical reaction cross sections for alpha particles with an optical model”, Nucl. Phys. 29 (1962) 462.

[Hor04] H. Horiuchi, “Cluster structure in nuclei”, Nucl. Phys. A731 (2004) 329.

[Ide01] E. Ideguchi, D. G. Sarantites, W. Reviol, A. V. Afanasjev, M. Devlin, C. Baktash, R. V. F. Janssens, D. Rudolph, A. Axelsson, M. P. Carpenter, A. Galindo-Uribarri, D. R. LaFosse, T. Lauritsen, F. Lerma, C. J. Lister, P. Reiter, D. Seweryniak, M. Weiszflog, and J. N. Wilson, “Superdeformation in the Doubly Magic Nucleus $^{40}_{20}Ca_{20}$”, Phys. Rev. Lett. 87, (2001) 222501.

[Ign75] A. V. Ignatyuk, G. N. Smirenkin, and A. S. Tishin, Sov. J. Nucl. Phys. 21, (1975) 255 Yad. Fiz. 21, 485 (1975).

[Jac75] J. D. Jackson, "Classical Electrodynamics", Second Edition, J. Wiley and Sons, (1975).

[Jur08] A.R. Junghans, G. Rusev, R. Schwengner, A. Wagner, E. Grosse, "Photon data shed new light upon the GDR spreading width in heavy nuclei", Phys. Lett. B670 (2008) 200.

[Kas89] J. Kasagi, H. Hama, K. Yoshida, et al., J. Phys. Soc. Jpn. Suppl. 58 (1989) 620.

[Kel97] M. P. Kelly, J. F. Liang, A. A. Sonzogni, K. A. Snover, J. P. S. van Schagen and J. P. Lestone, "Preequilibrium particle emission and the giant-dipole resonance in Sn nuclei", Phys. Rev. C 56 (1997) 3201.

[Kel99] M. P. Kelly, K. A. Snover, J. P. S. van Schagen, M. Kicinska-Habior and Z. Trznadel, "Giant Dipole Resonance in Highly Excited Nuclei: Does the Width Saturate?", Phys. Rev. Lett. 82 (1999) 3404.

[Kim04] Masaaki Kimura and Hisashi Horiuchi, "$^{16}$O$+^{16}$O molecular nature of the superdeformed band of $^{32}$S and the evolution of the molecular structure", Phys. Rev. C 69 (2004) 051304(R).

[Kin93] M. Kicinska-Habior, K. A. Snover, J. A. Behr, C. A. Gossett, Y. Alhassid and N. Whelen, "Search for a phase transition in the nuclear shape at finite temperature and rapid rotation ", Phys. Lett. B308 (1993) 225.

[Kin04] M. Kicinska-Habior, E. Wojcik, O. Kijewska, M. Kisielinski, M. Kowalczyk and J. Choinski, "Giant dipole radiation and isospin purity in highly excited $^{32}$S nuclei", Nucl. Phys. A731 (2004) 138.

[Kmi07] M. Kmiecik, A. Maj, M. Brekiesz, K. Mazurek, P. Bednarczyk, J. Grebosz, W. Meczynski, J. Styczen, M. Zieblinski, K. Zuber, P. Papka, C. Beck, D. Curien, F. Haas, V. Rauch, M. Rousseau, J. Dudek, N. Schunck, A. Bracco, F. Camera, G. Benzoni, O. Wieland, B. Herskind, E. Farnea, G. De Angelis, "Strong Deformation Effects in Hot Rotating $^{46}$Ti ", Acta Phys. Pol. B 38 (2007) 1437.

[Kno99] G. F. Knoll, "Radiation Detection and Measurement", John Wiley & Sons, Inc., Third Edn. (1999).

[Kra79] H. J. Krappe, J. R. Nix and A. J. Sierk, "Unified nuclear potential for heavy-ion elastic scattering, fusion, fission, and ground-state masses and deformations", Phys. Rev. C 20 (1979) 992.

[Kus98] Dimitri Kusnezov, Y. Alhassid and K. A. Snover, “Scaling Properties of the Giant Dipole Resonance Width in Hot Rotating Nuclei”, Phys. Rev. Lett. 81 (1998) 542.

[Lan70] L. D. Landau and E. M. Lifshitz, “Statistical Physics”, Pergamon, Oxford, (1970) p. 115ff.

[Lew72] M. B. Lewis and F. E. Bertrand, “Evidence from inelastic proton scattering for a giant quadrupole vibration in spherical nuclei ”, Nucl. Phys. A196 (1972) 337.

[Luk91] S.J. Luke, C.A. Gosset and R. Vandenbosch, “Search for high energy $\gamma$ rays from the spontaneous fission of $^{252}$Cf”, Phys. Rev. C 44 (1991) 1548.

[Maj04] A. Maj, M. Kmiecik, A. Bracco, F. Camera, P. Bednarczyk, B. Herskind, S. Brambilla, G. Benzoni, M. Brekiesz, D. Curien, G. De Angelis, E. Farnea, J. Grbosz, M. Kicinska-Habior, S. Leoni, W. Mczynski, B. Million, D.R. Napoli, J. Nyberg, C.M. Petrache, et al., “Evidence for the Jacobi shape transition in hot $^{46}$Ti”, Nucl. Phys. A731 (2004) 319.

[Mat97] M. Mattiuzzi, A. Bracco, F. Camera, W.E. Ormand, J.J. Gaardhoje, A.Maj, B. Million, M. Pignanelli, T. Tveter “Angular momentum dependence of the GDR width in Sn nuclei at fixed excitation energy”, Nucl. Phys. A612 (1997) 262.

[Mol81] Peter Moller and J. R. Nix, “Nuclear mass formula with a Yukawa-plus-exponential macroscopic model and a folded-Yukawa single-particle potential”, Nucl. Phys. A361 (1981) 117.

[Muk07] S. Mukhopadhyay, Srijit Bhattacharya, Deepak Pandit, A. Ray, Surajit Pal, K. Banerjee, S. Kundu, T.K. Rana, S. Bhattacharya, C. Bhattacharya, A. Dec, S.R. Banerjee, “LAMBDA: Large Area Modular $BaF_2$ Detector Array for the measurement of high energy $\gamma$ rays”, Nucl. Inst. Meth. A582 (2007) 603.

[Muk12] S. Mukhopadhyay, Deepak Pandit, Surajit Pal, Srijit Bhattacharya, A. De, S. Bhattacharya, C. Bhattacharya, K. Banerjee, S. Kundu, T.K. Rana, G. Mukherjee, R. Pandey, M. Gohil, H. Pai, J.K. Meena , S.R. Banerjee, “Measurement of giant dipole resonance width at low temperature: A new experimental perspective”, Phys. Lett. B 709 (2012) 9

[Mye66] W. D. Myers and W. J. Swiatecki, "Nuclear masses and deformations" Nucl. Phys. 81 (1966) 1.

[Mye77] W. D. Myers, W. J. Swiatecki, T. Kodama, L. J. El-Jaick and E. R. Hilf, "Droplet model of the giant dipole resonance", Phys Rev. C 15 (1977) 2032.

[Nee82] K. Neergard, "The isovector dipole mode in heated rotating nuclei", Phys. Lett. 110B (1982) 7.

[New81] J. O. Newton, B. Herskind, R. M. Diamond, E. L. Dines, J. E. Draper, K. H. Lindenberger, C. Schuck, S. Shih and F. S. Stepehns, "Observation of Giant Dipole Resonances Built on States of High Energy and Spin", Phys. Rev. Lett. 46 (1981) 1383.

[Nif90] H. Nifennecker and J. A. Pinston, "High Energy Photon Production in Nuclear Reactions", Annu. Rev. Nucl. Part.Sci. 40 (1990) 113.

[Orm96] W. E. Ormand, P. F. Bortignon and R. A. Broglia, "Temperature Dependence of the Width of the Giant Dipole Resonance in $^{120}$Sn and $^{208}$Pb", Phys. Rev. Lett. 77 (1996) 607

[Orm99] W. E. Ormand, "Theoretical description of the giant-dipole resonance in hot nuclei", Nucl. Phys. A649 (1999) 145c.

[Pac88] J. M. Pocheco, C. Ynanouleas and R. A. Broglia, "Fluctuations in the Shape Transitions of Hot Nuclei", Phys. Rev. Lett. 61 (1988) 294.

[Ple92] H. van der Ploeg, R. Postma, J. C. Bacelar, T. van den Berg, V. Iacob, J. Jongman and A. van der Woude, "Large gamma anisotropy observed in the $^{252}$Cf spontaneous-fission process", Phys. Rev. Lett. 68 (1992) 3145.

[Ple95] H. van der Ploeg, J. C. S. Bacelar, A. Buda, C. R. Laurens, A. van der Woude, J. J. Gaardhoje, Zelazny, G. van't Hof and N. Kalantar-Nayestanaki, "Emission of photons in spontaneous fission of $^{252}$Cf", Phys. Rev. C 52 (1995) 1915.

[Ple95a] H. van der Ploeg,"$\gamma$-ray emission in the spontaneous fission of $^{252}$Cf and in the induced fission of $^{229}$Np$^{*}$ (fission time scales) " Ph.D Thesis, University of Groningen, (1995).

[Pit71] R. Pitthan and Th. Walcher, "Inelastic electron scattering in the giant resonance region of La, Ce and Pr", Phys. Lett. B36 (1971) 563.

[Per63] F. G. Perey, "Optical-Model Analysis of Proton Elastic Scattering in the Range of 9 to 22 MeV", Phys. Rev. 131 (1963) 745.

[Pom03] K. Pomorski and J. Dudek, "Nuclear liquid-drop model and surface-curvature effects", Phys. Rev. C 67 (2003) 044316.

[Pul77] F. Puhlhofer, "On the interpretation of evaporation residue mass distributions in heavy-ion induced fusion reactions", Nucl. Phys. A280 (1977) 267.

[Rat03] S. K. Rathi, "Study of high energy gamma rays in nuclear reactions", Ph.D Thesis, Bombay University, (2003).

[Ray91] A. Ray, D. Shapira, J. Gomez del Campo, H. J. Kim, C. Beck, B. Djerroud, B. Heusch, D. Blumenthal and B. Shivakumar, "Compound nucleus origin of back-angle yields in the $^{31}$P+$^{16}$O and $^{35}$Cl+$^{12}$C reactions", Phys. Rev. C 44 (1991) 514.

[Rin84] P. Ring, L.M. Robledo, J.L. Egido and J.L. Faber, "Microscopic theory of the isovector dipole resonance at high angular momenta ", Nucl. Phys. A419 (1984) 261.

[Sag84] H. Sagawa and G.F. Bertsch, "Self-consistent calculations of finite temperature nuclear response function", Phys. Lett. B 146 (1984) 138.

[Sal08] M.D. Salsac, F. Haas, S. Courtin, A. Algora, C. Beck, S. Beghini, B.R. Behera, R. Chapman, L. Corradi, Z. Dombradi, E. Farnea, E. Fioretto, A. Gadea, D.G. Jenkins, A. Latina, D. Lebhertz, S. Lenzi, X. Liang, N. Marginean, G. Montagnoli, et al., "Decay of a narrow and high spin $^{24}$Mg + $^{24}$Mg resonance", Nucl. Phys. A 801, (2008) 1.

[San99] S. J. Sanders, A. Szanto de Toledo and C. Beck, "Binary decay of light nuclear systems", Phys. Rep. 311, (1999) 487.

[Sat76] G. R. Satchler and W. G. Love, "A new interaction for heavy-ion scattering", Phys Lett. B65 (1976) 415.

[Sch66] H.W. Schmitt, J.H. Neiler, F.J. Walter, "Fragment Energy Correlation Measurements for $^{252}$Cf Spontaneous Fission and $^{235}$U Thermal-Neutron Fission", Phys. Rev. 141 (1966) 1146.

[Sch69] W. Scheid and W. Greiner, Z. Phys. 226 (1969) 364.

[Sch82] K. -H. Schmidt, H. Delagrange, J. P. Dufour, N. Carjan and A. Fleury, "Influence of shell structure and pairing correlations on the nuclear state density", Z. Phys. A308 (1982) 215.

[Sha79] D. Shapira, J. L. C. Ford, J. GomezdelCampo, R. G. Stokstad, and R. M. DeVries, "Orbiting in the $^{12}$C + $^{20}$Ne System", Phys. Rev. Lett. 43 (1979) 1781.

[Sno86] K. A. Snover, "Giant resonance in excited nuclei", Ann. Rev. Nucl. Part. Sci. 36 (1986) 545.

[Sre06] J. Srebrny, T. Czosnyka, Ch. Droste, S.G. Rohozinski, L. Prchniak, K. Zajac, K. Pomorski, D. Cline, C.Y. Wu, A. Backlin, L. Hasselgren, R.M. Diamond, D. Habs, H.J. Korner, F.S. Stephens, C. Baktash, R.P. Kostecki, "Experimental and theoretical investigations of quadrupole collective degrees of freedom in $^{104}$Ru", Nucl. Phys. A766 (2006) 25.

[Sri08] Srijit Bhattacharya, S. Mukhopadhyay, Deepak Pandit, Surajit Pal, A. De, S. Bhattacharya, C. Bhattacharya, K. Banerjee, S. Kundu, T. K. Rana, A. Dey, G. Mukherjee, T. Ghosh, D. Gupta, and S. R. Banerjee, "Giant dipole resonance width in nuclei near Sn at low temperature and high angular momentum", Phys. Rev. C 77 (2008) 024318.

[Sri09] S. Bhattacharya, "Studies of giant resonances built on very highly excited states in nuclei", Ph.D Thesis, Calcutta University, (2008).

[Ste50] H. Steinwedel and J. H. Jensen, Z. Naturforch, 52 (1950) 413.

[Sve00] C. E. Svensson et al., "Superdeformation in the $N = Z$ Nucleus $^{36}$Ar: Experimental, Deformed Mean Field, and Spherical Shell Model Descriptions" Phys. Rev. Lett. 85 (2000) 2693.

[Van02] E.V.D. Van Loef, "Scintillation properties of $LaBr_3$:$Ce^{3+}$ crystals: fast, efficient and high-energy-resolution scintillators", Nucl. Inst. Meth. A486 (2002) 254.

[Var05] V.A. Varlachev, G.N. Dudkin, V.N. Padalko, "Does the coherent bremsstrahlung of fission fragments exist?", JETP Lett. 0582 (2005) 390.

[Vre99] D. Vretenar, P. Ring, G. A. Lalazissis and N. Paar, "Relativistic mean-field description of the dynamics of giant resonances" Nucl. Phys. A649 (1999) 29c.

[Wah88] A.C. Wahl, “Nuclear-charge distribution and delayed-neutron yields for thermal-neutron-induced fission of $^{235}$U, $^{233}$U and $^{239}$Pu and for spontaneous fission of $^{252}$Cf”, At. Data Nucl. Data Tables 39 (1988) 1.

[Wil64] D. Wilmore and P. E. Hodgson, “The calculation of neutron cross-sections from optical potentials ”, Nucl. Phys. 55 (1964) 673.

[Woj06] E. Wojcik, M. Kicinska-Habior, O. Kijewska, M. Kowalczyk, M. Kisielinski, J. Choinski, “Giant Dipole Radiation and Isospin mixing in hot light nucclei.”, Acta Phys. Pol. B 37, (2006) 207.

# List of Publications

1. "*Critical behavior in the variation of GDR width at low temperature*", **Deepak Pandit**, S. Mukhopadhyay, Surajit Pal, A. De and S. R. Banerjee, **Phys. Lett. B713 (2012) 434**.

2. "*Measurement of giant dipole resonance width at low temperature: A new experimental perspective*", S. Mukhopadhyay, **Deepak Pandit**, Surajit Pal, Srijit Bhattacharya, A. De, S. Bhattacharya, C. Bhattacharya, K. Banerjee, S. Kundu, T.K. Rana, G. Mukherjee, R. Pandey, M. Gohil, H. Pai, J.K. Meena , S.R. Banerjee, **Phys. Lett. B 709 (2012) 9**.

*3. "*Coherent bremsstrahlung and GDR width from $^{252}Cf$ cold fission*", **Deepak Pandit**, S. Mukhopadhyay, Srijit Bhattacharya , Surajit Pal , A. De, S. R. Banerjee, **Phys. Lett. B 690 (2010) 473**.

*4. "*Extreme nuclear shapes examined via giant dipole resonance lineshapes in hot light-mass systems*", **Deepak Pandit**, S. Mukhopadhyay,Srijit Bhattacharya, Surajit Pal, A. De, S. Bhattacharya, C. Bhattacharya, K. Banerjee, S. Kundu, T. K. Rana, A. Dey, G. Mukherjee, T. Ghosh, D. Gupta, and S. R. Banerjee, **Phys. Rev. C 81 (2010) 061302(Rapid)**.

*5. "*A realistic technique for selection of angular momenta from hot nuclei: A case study with $^4He + {}^{115}In \rightarrow {}^{119}Sb*$ at $E_{Lab} = 35$ MeV*", **Deepak Pandit**, S. Mukhopadhyay, Srijit Bhattacharya , Surajit Pal , A. De, S. R. Banerjee, **NIM A 624 (2010) 148**.

6. "*Variation of neutron detection characteristics with dimension of BC501A neutron detector*", K. Banerjee, T. K. Ghosh, S. Kundu, T. K. Rana, C. Bhattacharya, J. K. Meena, G. Mukherjee, P.Mali, D. Gupta, S. Mukhopadhyay, **D Pandit**, S. R. Banerjee, S.Bhattacharya , T. Bandyopadhyay, S.Chatterjee, **NIM A 608 (2009) 440**.

7. "*Giant dipole resonance width in nuclei near Sn at low temperature and high angular momentum*", Srijit Bhattacharya, S. Mukhopadhyay, **Deepak Pandit**, Surajit Pal, A. De, S. Bhattacharya, C. Bhattacharya, K. Banerjee, S. Kundu, T. K. Rana, A. Dey, G. Mukherjee, T. Ghosh, D. Gupta, and S. R. Banerjee, **Phys. Rev. C 77 (2008) 024318**.

*Indicates publications related to this thesis.

8. "*Scaling of the giant dipole resonance widths in hot rotating nuclei from the ground state values*", Srijit Bhattacharya, **Deepak Pandit**, S. Mukhopadhyay, Surajit Pal, and S. R. Banerjee, **Phys. Rev. C 78 (2008) 064601**.

9. "*Consistency of nuclear thermometric measurements at moderate excitation*", T. K. Rana, C. Bhattacharya, S. Kundu, K. Banerjee, S. Bhattacharya, A. Dey, T. K. Ghosh, G. Mukherjee, J. K. Meena,D. Gupta, S. Mukhopadhyay, **D Pandit**, S. R. Banerjee, A. Roy, and P. Dhara, **Phys. Rev. C 78 (2008) 027602**.

10. "*LAMBDA: Large Area Modular $BaF_2$ Detector Array for the measurement of high energy gamma rays*", S. Mukhopadhyay, Srijit Bhattacharya, **Deepak Pandit**, A. Ray, Surajit Pal, K. Banerjee, S. Kundu, T. K. Rana, S. Bhattacharya, C. Bhattacharya, A. De, S. R. Banerjee, **NIM A 582 (2007) 603**.

11. "*Characteristics of Gd-loaded liquid scintillators BC521 and BC525*", K. Banerjee, S. Kundu, S. Mukhopadhyay, T.K. Rana, S. Bhattacharya, C. Bhattacharya, S. R. Banerjee, T.K. Ghosh, G. Mukherjee, T. Bandyopadhyay, A. Dey, J. K. Meena, P. Mukhopadhyay, D. Gupta, S. Pal, **D Pandit**, S. Bhattacharya, **NIM A 580 (2007) 1383**.